

Final state interaction and temperature effects in Compton scattering from lithium

DISSERTATION

zur Erlangung des Doktorgrades der Naturwissenschaften
des Fachbereiches Physik der Universität Dortmund

vorgelegt von

Christian Sternemann

2000

Erster Gutachter: Prof. Dr. W. Schülke
Zweiter Gutachter: Prof. Dr. F. Bell
Tag der mündlichen Prüfung: 22. Dezember 2000

Contents

Introduction	1
1 Compton scattering	5
1.1 Inelastic x-ray scattering	5
1.2 Impulse approximation	8
1.3 Compton profile	12
1.3.1 Non-relativistic limit	12
1.3.2 Relativistic effects	13
1.3.3 Electron momentum density	14
1.4 Reciprocal form factor	19
2 The dynamic structure factor at metallic densities	21
2.1 Polarization function	21
2.1.1 Fluctuation-dissipation theorem	21
2.1.2 Dielectric response	22
2.2 Self-energy effects	26
2.2.1 Spectral density function	26
2.2.2 Self-energy correction	28
2.2.3 Lindhard approximation	29
2.2.4 Self-energy effects on the dynamic structure factor in the Compton limit	30
2.3 Vertex correction	32
2.3.1 Local field approximation	32
2.3.2 First and second order vertex correction	33

3	Final state interaction in Compton scattering from lithium	35
3.1	Experiment	37
3.1.1	Experimental setup	37
3.1.2	Data evaluation	39
3.2	Experimental results	47
3.3	Valence Compton profile asymmetry	52
3.3.1	Self-energy correction	54
3.3.2	Vertex correction	56
3.4	Influence of the spectral density function of the particle on the valence Compton profile	58
3.5	Reciprocal form factor	65
3.6	Summary	68
4	Temperature effects in Compton scattering from lithium	69
4.1	Experiment	72
4.1.1	Experimental setup	72
4.1.2	Data evaluation	74
4.2	Experimental results	78
4.3	The homogeneous interacting electron gas	84
4.4	Pseudopotential calculation	88
4.4.1	Pseudopotential scheme	88
4.4.2	Temperature dependent pseudopotential calculation	89
4.5	Summary	94
	Conclusion	95
	A The fully dressed Green's function	99
	B Local field approximation	103
	Bibliography	105
	Figures	113
	Tables	115

Introduction

In the early 1920's the Compton effect, i.e. the softening of scattered x-rays, was discovered and correctly interpreted [Compton 1923, Debye 1923] and a few years later DuMond [DuMond 1929] has shown that the measured Compton profile of beryllium was in line with the predictions of the Fermi-Dirac statistics. In the following years the relation between the Compton profile and the electron momentum distribution was investigated systematically [DuMond and Kirkpatrick 1931, DuMond and Hoyt 1931, DuMond et al. 1932]. Kappeler [Kappeler 1936] measured Compton profiles of the solids lithium, carbon, sodium fluoride and the gases neon, oxygen and nitrogen obtaining reasonable agreement with theory, except for the Compton profile of lithium, which was by a factor of 2.5 wider than the theoretical predictions. Each attempt to explain this discrepancy on the theoretical side failed. In spite of the physical significance of this experimental technique Compton scattering faded away in the late 1930's for a period of roughly 25 years, which may be due to the enormous experimental difficulties the experimentalists had to overcome.

With the development of efficient scintillation counters and rotating anode x-ray generators the revival of Compton scattering started in the middle of the 1960's with the experimental work of Cooper et al. [Cooper et al. 1965] showing that the experimental result for lithium obtained by Kappeler [Kappeler 1936] was incorrect and confirming the former theoretical predictions. At this time the interplay between theory and experiment was incited since a discussion of the validity of the impulse approximation has been presented by Platzman and Tzoar [Platzman and Tzoar 1965] and the effect of electron-electron correlation on the Compton profile has been discussed [Lam and Platzman 1974]. From the experimental point of view Compton scattering studies have been restricted to the light elements since only x-ray sources having low x-ray energies and intensities were accessible at this time.

The advent of synchrotron radiation along with the use of solid state detectors [Holt et al. 1978] followed by the crystal-dispersive analysis of the scattered photons [Loupas et al. 1980] established the applicability of Compton scattering to a variety of heavier and more complex materials. Along with this high improvement on the experimental side Compton scattering became an excellent tool to investigate the ground state properties of electronic sys-

tems so that problems related to fermiology and electronic structure were extensively studied for ordered and disordered systems [Loupas et al. 1984, Bauer and Schneider 1985, Bansil 1993, Manninen et al. 1996, Bansil et al. 1998, Marangolo et al. 1999, Stutz et al. 1999, Dugdale et al. 2000]. Especially, the effect of electron-electron correlation on the electron momentum density attracted more and more interest and was investigated on pretended simple systems like aluminium, lithium, beryllium and sodium [Cardwell and Cooper 1989, Suortti et al. 2000, Sakurai et al. 1995, Schülke et al. 1996, Huotari et al. 2000, Hämäläinen 2000]. Recently, Compton scattering was applied to study the electronic properties of high temperature superconductors [Shukla et al. 1999] and the technique to extract information from the Compton profiles with respect to the chemical bonding utilizing the Fourier transform of the Compton profile was renewed [Asthalter and Weyrich 1997, Anastassopoulos et al. 1998, Isaacs et al. 1999, Shukla et al. 1999]. This method has been used in the early 1980's by Pattison et al. [Pattison et al. 1981] to investigate bonding effects in diamond and silicon and has its origin in the very early work of Schülke [Schülke 1977] and Weyrich [Weyrich et al. 1979]. Furthermore, circularly polarized synchrotron radiation was utilized to separate the spin dependent part of the Compton scattering cross section yielding information about the spin density [Sakai 1996, Cooper and Duffy 2000]. The progress on the experimental side was attended by the permanent improvement of the theoretical approaches [Holm and Ribberfors 1989, Bansil 1993, Blaas et al. 1995, Sakurai et al. 1995, Weyrich 1996, Králik et al. 1998, Duffy et al. 2000].

Within this thesis the valence Compton profile of lithium is investigated which is of a particular interest, in the history and in the present, since for lithium a significant discrepancy was found between experimentally obtained Compton profiles and results from band structure calculations [Sakurai et al. 1995, Schülke et al. 1996, Filippi and Ceperley 1999]. This discrepancy was widely discussed in terms of electron-electron correlation with respect to the value of the renormalization constant describing the discontinuity of the electron momentum density at the Fermi momentum [Kubo 1997, Schülke 1999, Eguiluz et al. 2000, Dobrzyński 2000]. Furthermore, it was suggested that temperature effects can explain this discrepancy [Dugdale and Jarlborg 1998] and new theoretical approaches were tested [Baruah et al. 1999, Barbiellini 2000]. Schülke et al. [Schülke et al. 1996] stated that final state interaction may play an important role in interpreting the valence Compton profile of lithium even for relatively high incident photon energies around 30 keV. To investigate the features of the Compton profile which are related to the discontinuity at the Fermi momentum, measurements of the valence Compton profile have to be performed at low incident energy to obtain an appropriate momentum space resolution [Hämäläinen et al. 1996]. Utilizing this low incident energy may cause problems to fulfill the prerequisites of the impulse approximation.

With respect to the unsatisfactory situation in interpreting the valence Compton profiles of lithium the aim of this thesis is to examine some of the above mentioned aspects in detail. The effect of the final state interaction on the Compton profile of lithium will be studied systematically so that the validity of the impulse approximation can be investigated by a Compton scattering experiment on lithium performed at low incident energies having a momentum space resolution in the order of a few percent of the Fermi momentum. Furthermore, the effect of temperature on the lithium valence Compton profile will be measured and discussed according to the theoretical predictions of Dugdale and Jarlborg [Dugdale and Jarlborg 1998].

Within chapter 1 the fundamentals of Compton scattering are presented. The theoretical formalism to calculate the dynamic structure factor in terms of the polarization function is discussed in chapter 2. It is shown how final state interaction is considered within the calculation of the polarization function using self-energy and vertex corrections. Then the effect of the final state interaction in the Compton scattering limit is discussed. Chapter 3 is dedicated to the high resolution Compton profile measurements on lithium which are interpreted in terms of final state interaction followed by the presentation and discussion of the measured temperature effect in chapter 4.

Chapter 1

Compton scattering

Chapter 1 comprehends the theoretical fundamentals of the inelastic x-ray scattering process. The dynamic structure factor, which describes the dynamical response of the electron system to the perturbation mediated by the photon field, is introduced and treated within the so-called Compton limit utilizing the impulse approximation thus yielding the Compton profile in momentum space, which, for valence electrons, is discussed in terms of electron-electron and electron-ion interaction. Finally, the properties of the reciprocal form factor for interpreting Compton profiles are emphasized.

1.1 Inelastic x-ray scattering

Within the inelastic x-ray scattering process the incoming photon with energy $\hbar\omega_1$, wave vector \vec{k}_1 and polarization vector $\vec{\epsilon}_1$ is scattered into a photon having energy $\hbar\omega_2$, wave vector \vec{k}_2 and polarization vector $\vec{\epsilon}_2$. The photon transfers the energy $\hbar\omega = \hbar(\omega_1 - \omega_2)$ and the momentum $\hbar\vec{q} = \hbar(\vec{k}_1 - \vec{k}_2)$ to the scattering system. The momentum transfer $|\vec{q}|$ and the scattering angle θ are related via $|\vec{q}| = 2|\vec{k}_1|\sin(\theta/2)$ provided $\omega \ll \omega_1$. The kinematics of the scattering process are illustrated in Fig. 1.1. Natural units in which $\hbar = c = 1$ are used for the derivation of the double differential cross section, the quantity measured in an IXSS (inelastic x-ray scattering spectroscopy) experiment.

Inelastic x-ray scattering by electrons is well described within the non-relativistic limit in the lowest order Born approximation (first order perturbation theory) [Van Hove 1954]. The double differential cross section of a system of N electrons within a volume V_c is given by

$$\frac{d^2\sigma}{d\Omega d\omega_2} = N_0 \frac{\rho}{I_0} \sum_{|i\rangle} w_{|i\rangle} P_{|i\rangle \rightarrow |f\rangle}(\vec{q}, \omega), \quad (1.1)$$

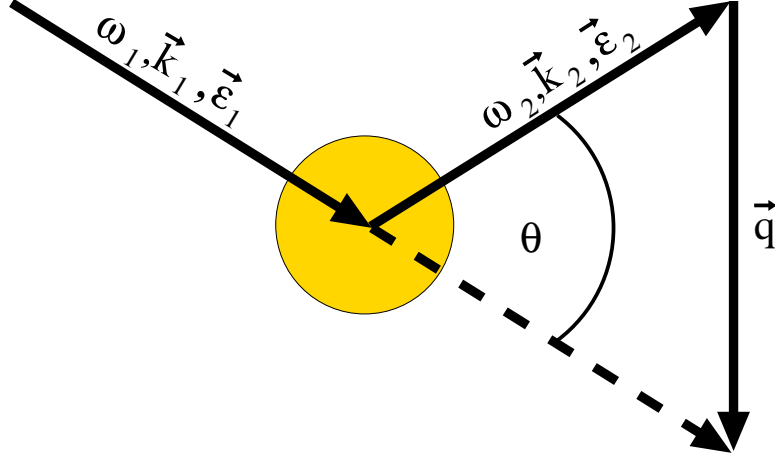


Figure 1.1: The inelastic scattering process.

where N_0 denotes the number of incoming photons, $\rho = V_c \omega_2^2 / (2\pi)^3$ the density of final photon states, $I_0 = N_0 / V_c$ the incident photon flux, and $w_{|i\rangle}$ the probability for the electron system to be in the initial many-particle state $|i\rangle$ [Blume 1985]. According to Fermi's golden rule the transition probability per unit time for the photon to transfer momentum \vec{q} and energy ω to the system is

$$P_{|i\rangle \rightarrow |f\rangle}(\vec{q}, \omega) = 2\pi \sum_{|f\rangle} \left| \langle f | H_{\text{int}} | i \rangle \right|^2 \delta(\omega + (E_i - E_f)) \quad (1.2)$$

with the sum calculated over all many-particle final states $|f\rangle$, the interaction Hamiltonian H_{int} and the δ -function, which specifies the energy conservation of the scattering process. The interaction Hamiltonian is given by

$$H_{\text{int}} = \sum_j \frac{e^2}{2m} \vec{A}(\vec{r}_j)^2 - \sum_j \frac{e}{m} \vec{p}_j \cdot \vec{A}(\vec{r}_j), \quad (1.3)$$

where the vector potential of the photon field $\vec{A}(\vec{r}_j)$ is used within the Coulomb gauge ($\vec{\nabla} \cdot \vec{A}(\vec{r}_j) = 0$) and the magnetic contributions are neglected, since they are smaller in amplitude by ω/m compared with the charge terms. \vec{r}_j is the position of the j th electron and \vec{p}_j the corresponding momentum operator. The vector potential can be expanded in terms of the photon annihilation operator $a(\lambda, \vec{k})$ and creation operator $a^\dagger(\lambda, \vec{k})$ via

$$\vec{A}(\vec{r}_j) = \sum_{\lambda, \vec{k}} \sqrt{\frac{2\pi}{V_c \omega_{\vec{k}}}} \left(\vec{\epsilon}(\lambda, \vec{k}) a(\lambda, \vec{k}) e^{i\vec{k} \cdot \vec{r}_j} + \vec{\epsilon}^*(\lambda, \vec{k}) a^\dagger(\lambda, \vec{k}) e^{-i\vec{k} \cdot \vec{r}_j} \right). \quad (1.4)$$

$\vec{\epsilon}(\lambda, \vec{k})$ presents the polarization vector of the transversal electromagnetic wave ($\vec{\epsilon}(\lambda, \vec{k}) \cdot \vec{k} = 0$) and λ denotes its two possible polarizations. In first order perturbation theory only the \vec{A}^2 -term contributes since the scattering process is a two photon process. As long as $\omega \gg k_B T$, the electron system can be considered to be in the ground state and the sum over the initial states $|i\rangle$ with weight $w_{|i\rangle}$ in Eq. (1.1) may be replaced by the many-particle ground state $|i_0\rangle$. One gets for the double differential cross section

$$\begin{aligned} \frac{d^2\sigma}{d\Omega d\omega_2} &= \frac{e^4}{m^2} (\vec{\epsilon}_1 \cdot \vec{\epsilon}_2)^2 \frac{\omega_2}{\omega_1} \sum_{|f\rangle} \left| \langle f | \sum_j e^{i\vec{q} \cdot \vec{r}_j} | i_0 \rangle \right|^2 \delta(\omega + (E_{i_0} - E_f)) \quad (1.5) \\ &= \left(\frac{d\sigma}{d\Omega} \right)_{\text{Th}} \frac{\omega_2}{\omega_1} S(\vec{q}, \omega) \quad (1.6) \end{aligned}$$

in which the dynamic structure factor $S(\vec{q}, \omega)$ describes the dynamical response of the system to the perturbation whereas the Thomson scattering cross section

$$\left(\frac{d\sigma}{d\Omega} \right)_{\text{Th}} = r_0^2 (\vec{\epsilon}_1 \cdot \vec{\epsilon}_2)^2 \quad (1.7)$$

reflects the coupling of the photon field with the electrons of the system. $r_0 = e^4/m^2$ denotes the classical electron radius and the polarization of the incoming and the outgoing photon is given by $\vec{\epsilon}_1$ and $\vec{\epsilon}_2$. A detailed discussion of the dynamical structure factor is presented in chapter 3.

Whenever the transferred energy ω and the transferred momentum q are much larger than characteristic energies and reciprocal distances of the scattering system, the impulse approximation can be applied to Eq. (1.5) and the double differential scattering cross section in the Compton scattering limit will be obtained, which is discussed within the following section.

1.2 Impulse approximation

Starting from Eq. (1.5) and using the Fourier representation of the δ -function

$$\delta(\omega + (E_{i_0} - E_f)) = \delta(E_f - E_{i_0} - \omega) = \frac{1}{2\pi} \int dt e^{i(\omega + (E_{i_0} - E_f))t} \quad (1.8)$$

yields

$$\begin{aligned} \frac{d^2\sigma}{d\Omega d\omega_2} = & \left(\frac{d\sigma}{d\Omega} \right)_{\text{Th}} \frac{\omega_2}{\omega_1} \frac{1}{2\pi} \int dt e^{-i\omega t} \sum_{|f\rangle} \langle i_0 | \sum_{j'} e^{-i\vec{q}\cdot\vec{r}_{j'}} | f \rangle \\ & \times \langle f | e^{iE_f t} \sum_j e^{i\vec{q}\cdot\vec{r}_j} e^{-iE_{i_0} t} | i_0 \rangle . \end{aligned} \quad (1.9)$$

The Hamilton operator of the electron system $H = H_0 + V$ acting on the corresponding many-particle eigenfunctions $|i_0\rangle, |f\rangle$ with the kinetic term H_0 and the potential V is inserted into Eq. (1.9) via

$$e^{-iHt}|i_0\rangle = e^{-iE_{i_0}t}|i_0\rangle, \quad \langle f|e^{iHt} = \langle f|e^{iE_f t}. \quad (1.10)$$

Utilizing the completeness relation

$$\sum_{|f\rangle} |f\rangle\langle f| = 1 \quad (1.11)$$

gives

$$\frac{d^2\sigma}{d\Omega d\omega_2} = \left(\frac{d\sigma}{d\Omega} \right)_{\text{Th}} \frac{\omega_2}{\omega_1} \frac{1}{2\pi} \int dt e^{-i\omega t} \langle i_0 | \sum_{j'} e^{-i\vec{q}\cdot\vec{r}_{j'}} e^{iHt} \sum_j e^{i\vec{q}\cdot\vec{r}_j} e^{-iHt} | i_0 \rangle . \quad (1.12)$$

Now, the Hamiltonian exponential is expanded into

$$e^{iHt} \approx e^{iH_0 t} e^{iVt} e^{-\frac{1}{2}[H_0, V]t^2} \quad (1.13)$$

neglecting terms of higher order in the time t . The integral in Eq. (1.12) provides significant contributions only for $t \approx 1/\omega$ due to the time dependence of the matrix element describing the excitation of the system. Thus the approximation

$$e^{-\frac{1}{2}[H_0, V]t^2} \simeq 1 \quad (1.14)$$

is justified as long as

$$\frac{1}{2}\langle [H_0, V] \rangle \approx E_c^2 \ll \omega^2, \quad (1.15)$$

where E_c denotes characteristic energies of the system, i.e. the binding energies of the core or the valence electrons [Eisenberger and Platzman 1970]. The contribution of V in Eq. (1.12) cancels since it commutes with \vec{r} , the electron position, so that

$$\frac{d^2\sigma}{d\Omega d\omega_2} = \left(\frac{d\sigma}{d\Omega} \right)_{\text{Th}} \frac{\omega_2}{\omega_1} \frac{1}{2\pi} \int dt e^{-i\omega t} \left\langle i_0 \left| \sum_{j'} e^{-i\vec{q}\cdot\vec{r}_{j'}} e^{iH_0 t} \sum_j e^{i\vec{q}\cdot\vec{r}_j} e^{-iH_0 t} \right| i_0 \right\rangle \quad (1.16)$$

is obtained. Therefore, the essence of the impulse approximation consists in the assumption that the excitation process evolves under a constant potential V so that the energy of the system is measured in relation to this constant potential both in the initial and in the final state. Eq. (1.16) is separated into one- and two-particle contributions by

$$\begin{aligned} \frac{d^2\sigma}{d\Omega d\omega_2} = & \left(\frac{d\sigma}{d\Omega} \right)_{\text{Th}} \frac{\omega_2}{\omega_1} \frac{1}{2\pi} \int dt e^{-i\omega t} \left\{ N \left\langle i_0 \left| e^{-i\vec{q}\cdot\vec{r}_1} e^{iH_0 t} e^{i\vec{q}\cdot\vec{r}_1} e^{-iH_0 t} \right| i_0 \right\rangle \right. \\ & \left. + 2 \binom{N}{2} \left\langle i_0 \left| e^{-i\vec{q}\cdot\vec{r}_1} e^{iH_0 t} e^{i\vec{q}\cdot\vec{r}_2} e^{-iH_0 t} \right| i_0 \right\rangle \right\}, \quad (1.17) \end{aligned}$$

where N is the number of electrons. Then the spin-free one-particle density matrix $\gamma(\vec{r}_1|\vec{r}_1')$ and the spin-free two-particle density matrix $\Gamma(\vec{r}_1\vec{r}_2|\vec{r}_1'\vec{r}_2')$ can be introduced, according to Löwdin's convention [Löwdin 1955], yielding

$$\begin{aligned} \frac{d^2\sigma}{d\Omega d\omega_2} = & \left(\frac{d\sigma}{d\Omega} \right)_{\text{Th}} \frac{\omega_2}{\omega_1} \frac{1}{2\pi} \int dt e^{-i\omega t} \left\{ \int d\vec{r}_1 e^{-i\vec{q}\cdot\vec{r}_1} e^{iH_0 t} e^{i\vec{q}\cdot\vec{r}_1} e^{-iH_0 t} \gamma(\vec{r}_1|\vec{r}_1') \right. \\ & \left. + 2 \int \int d\vec{r}_1 d\vec{r}_2 e^{-i\vec{q}\cdot\vec{r}_1} e^{iH_0 t} e^{i\vec{q}\cdot\vec{r}_2} e^{-iH_0 t} \Gamma(\vec{r}_1\vec{r}_2|\vec{r}_1'\vec{r}_2') \right\}. \quad (1.18) \end{aligned}$$

In what follows only the first term of Eq. (1.18) will be discussed since it has been shown by Benesch and Smith [Benesch and Smith 1973] that the contribution of

the two-particle density matrix can be neglected within the limits of the impulse approximation. Now a complete set $\sum_{|\vec{p}\rangle} |\vec{p}\rangle\langle\vec{p}|$ of eigenfunctions $|\vec{p}\rangle$ of H_0

$$|\vec{p}\rangle = \frac{1}{\sqrt{V_c}} e^{i\vec{p}\cdot\vec{r}} \quad (1.19)$$

is inserted into Eq. (1.18) with $H_0 |\vec{p}\rangle = \epsilon_{\vec{p}} |\vec{p}\rangle$ and the free-particle energy $\epsilon_{\vec{p}} = |\vec{p}|^2/2m$. This insertion induces a double \vec{r} integration according to the Löwdin formalism ending up with

$$\begin{aligned} \frac{d^2\sigma}{d\Omega d\omega_2} = & \left(\frac{d\sigma}{d\Omega} \right)_{\text{Th}} \frac{\omega_2}{\omega_1} \frac{1}{2\pi V_c} \int dt e^{-i\omega t} \sum_{\vec{p}} \int d\vec{r}_1 e^{-i\vec{q}\cdot\vec{r}_1} e^{iH_0 t} e^{i\vec{p}\cdot\vec{r}_1} \\ & \times \int d\vec{r}'_1 e^{-i\vec{p}\cdot\vec{r}'_1} e^{i\vec{q}\cdot\vec{r}'_1} e^{-iH_0 t} \gamma(\vec{r}_1 | \vec{r}'_1) . \end{aligned} \quad (1.20)$$

The Hamiltonian H_0 acts on the eigenfunctions $|\vec{p}\rangle$ as follows:

$$\begin{aligned} e^{-i\vec{q}\cdot\vec{r}_1} e^{iH_0 t} e^{i\vec{p}\cdot\vec{r}_1} &= e^{-i\vec{q}\cdot\vec{r}_1} e^{i\epsilon_{\vec{p}} t} e^{i\vec{p}\cdot\vec{r}_1} = e^{i\epsilon_{\vec{p}} t} e^{i(\vec{p}-\vec{q})\cdot\vec{r}_1} \\ e^{-i\vec{p}\cdot\vec{r}'_1} e^{i\vec{q}\cdot\vec{r}'_1} e^{-iH_0 t} &= e^{-i(\vec{p}-\vec{q})\cdot\vec{r}'_1} e^{-iH_0 t} = e^{-i(\vec{p}-\vec{q})\cdot\vec{r}'_1} e^{-i\epsilon_{\vec{p}-\vec{q}} t} . \end{aligned} \quad (1.21)$$

This yields

$$\begin{aligned} \frac{d^2\sigma}{d\Omega d\omega_2} = & \left(\frac{d\sigma}{d\Omega} \right)_{\text{Th}} \frac{\omega_2}{\omega_1} \frac{1}{2\pi V_c} \sum_{\vec{p}} \int dt e^{i(\epsilon_{\vec{p}} - \epsilon_{\vec{p}-\vec{q}} - \omega) t} \\ & \times \int \int d\vec{r}_1 d\vec{r}'_1 e^{i(\vec{p}-\vec{q})\cdot\vec{r}_1} e^{-i(\vec{p}-\vec{q})\cdot\vec{r}'_1} \gamma(\vec{r}_1 | \vec{r}'_1) . \end{aligned} \quad (1.22)$$

Since the one-particle density matrix in momentum space $\gamma(\vec{p} | \vec{p}')$ is defined as the 6-dimensional Fourier transform of the spin-free one-particle density matrix in position space $\gamma(\vec{r}_1 | \vec{r}'_1)$ [Benesch et al. 1971]

$$\gamma(\vec{p} | \vec{p}') = \frac{1}{(2\pi)^3} \int \int d\vec{r} d\vec{r}' e^{-i(\vec{p}\cdot\vec{r} - \vec{p}'\cdot\vec{r}')} \gamma(\vec{r} | \vec{r}') \quad (1.23)$$

one obtains after rewriting the time integral as a δ -function

$$\frac{d^2\sigma}{d\Omega d\omega_2} = \left(\frac{d\sigma}{d\Omega} \right)_{\text{Th}} \frac{\omega_2}{\omega_1} \frac{(2\pi)^3}{V_c} \sum_{\vec{p}} \gamma(\vec{p} - \vec{q} | \vec{p} - \vec{q}) \delta(\epsilon_{\vec{p}} - \epsilon_{\vec{p}-\vec{q}} - \omega) . \quad (1.24)$$

The sum over \vec{p} is written as an integral and the substitution $\vec{p} - \vec{q} = \vec{p}'$ is performed. Finally \vec{p}' is replaced by \vec{p} ending up with

$$\frac{d^2\sigma}{d\Omega d\omega_2} = \left(\frac{d\sigma}{d\Omega} \right)_{\text{Th}} \frac{\omega_2}{\omega_1} \int d\vec{p} \gamma(\vec{p}|\vec{p}) \delta \left(\omega - \frac{\vec{p} \cdot \vec{q}}{m} - \frac{q^2}{2m} \right). \quad (1.25)$$

The double differential cross section within the impulse approximation can be derived directly from Eq. (1.5) utilizing the one-particle picture, if the energy difference $E_{i_0} - E_f$ is calculated for free particles and the final state is assumed to be a plane wave. The momentum space integral of the electron momentum density represented by the diagonal elements of the spin-free one-particle density matrix is called the Compton profile, which can be considered as the projection of the ground state electron momentum density on the direction of the scattering vector \vec{q} and is discussed as follows.

1.3 Compton profile

The Compton profile is presented first in the non-relativistic limit. Then the relativistic Compton scattering cross section is described followed by a discussion of the electron momentum density for valence electrons.

1.3.1 Non-relativistic limit

In the non-relativistic limit the Compton profile is defined as

$$J(\vec{p} \cdot \vec{q}) = \int d\vec{p} \gamma(\vec{p} | \vec{p}) \delta \left(\omega - \frac{\vec{p} \cdot \vec{q}}{m} - \frac{q^2}{2m} \right). \quad (1.26)$$

with the momentum density $\gamma(\vec{p} | \vec{p})$, representing the probability to find an electron with momentum \vec{p} in the ground state. The δ -function describes the energy conservation of the process where $q^2/2m$ is the non-relativistic Compton shift for an electron initially at rest and $\vec{p} \cdot \vec{q}/m$ gives the Doppler shift according to the finite momentum \vec{p} of the electron in the initial state. When the scattering vector \vec{q} points into z -direction, performing of the p_z integration leads to

$$J(p_z) = \int \int dp_x dp_y \gamma(\vec{p} | \vec{p}), \quad (1.27)$$

where

$$p_z = \frac{m}{q} \omega - \frac{q}{2} \quad (1.28)$$

$$= m \frac{\omega_1 - \omega_2 - \frac{\omega_1 \omega_2}{m} (1 - \cos \theta)}{\sqrt{\omega_1^2 + \omega_2^2 - 2\omega_1 \omega_2 \cos \theta}}. \quad (1.29)$$

The double differential scattering cross section for Compton scattering is directly proportional to the Compton profile $J(p_z)$ utilizing Eq. (1.25)

$$\frac{d^2 \sigma}{d\Omega d\omega_2} = \left(\frac{d\sigma}{d\Omega} \right)_{\text{Th}} \frac{\omega_2}{\omega_1} \frac{m}{q} J(p_z). \quad (1.30)$$

The total Compton profile can be decomposed into contributions from the core electrons and the valence electrons, of which the core Compton profiles can be calculated properly [Holm and Ribberfors 1989]. The Compton profiles extracted

from the experiment have to be normalized with respect to the normalization condition

$$\int dp_z J(p_z) = N , \quad (1.31)$$

where N is the number of electrons per atom.

1.3.2 Relativistic effects

Within the non-relativistic limit it was shown that the double differential cross section can be separated into two parts, one describing the coupling of the probe to the electrons and the other the dynamical response of the scattering system. This strict separation is lost, when a fully relativistic treatment is applied. Nevertheless, it was emphasized by Ribberfors [Ribberfors 1975] that in the case of Compton scattering an approximate relativistic treatment yields

$$\frac{d^2\sigma}{d\Omega d\omega_2} = \frac{r_0^2}{2} \frac{\omega_2}{\omega_1} X(p_z) \frac{m}{q} J(p_z) . \quad (1.32)$$

The factorization of the two contributions is recovered and remains to be valid for arbitrary scattering angles and even anisotropic momentum distributions. The X -factor for linear polarized photons is calculated by the sum over the two polarization states of the scattered photons to

$$X(p_z) = \frac{R}{R'} + \frac{R'}{R} - 2 \sin^2 \theta \cos^2 \beta , \quad (1.33)$$

where β denotes the angle between the scattering plane and the polarization vector of the incident photons, θ the scattering angle and the factors R and R' are given by

$$\begin{aligned} R &= \omega_1 \left(m - (\omega_1 - \omega_2 \cos \theta) \frac{p_z}{q} \right) \\ R' &= R - \omega_1 \omega_2 (1 - \cos \theta) . \end{aligned} \quad (1.34)$$

In the case of unpolarized photons the average over all polarization vectors has to be calculated ending up with

$$X(p_z) = \frac{R}{R'} + \frac{R'}{R} - \sin^2 \theta . \quad (1.35)$$

If $p_z = 0$ a.u. (atomic units), the X -factor reduces to the Klein-Nishina X -factor which describes the relativistic photon scattering from a free electron.

1.3.3 Electron momentum density

The valence electron Compton profile of solids is now discussed by calculating the electron momentum density of the valence electrons $\gamma(\vec{p}|\vec{p})$. Thus, the one-particle density matrix $\gamma(\vec{r}|\vec{r}')$ is expressed in terms of the electron field operators $\Psi^\dagger(\vec{r}, t)$ and $\Psi(\vec{r}, t)$ [Lundqvist and Lydén 1971]

$$\gamma(\vec{p}|\vec{p}) = \frac{1}{(2\pi)^3} \int \int d\vec{r} d\vec{r}' e^{i\vec{p}\cdot(\vec{r}-\vec{r}')} \langle \Psi^\dagger(\vec{r}, 0) \Psi(\vec{r}', 0) \rangle, \quad (1.36)$$

where $\langle \rangle$ denotes the thermal average of a system of N electrons within the crystal volume V_c . The field operators are expanded in terms of Bloch waves $\phi_{\nu, \vec{k}}(\vec{r})$

$$\Psi(\vec{r}, 0) = \sum_{\nu, \vec{k}} a_{\nu, \vec{k}}(0) \phi_{\nu, \vec{k}}(\vec{r}) \quad (1.37)$$

with the electron annihilation operator $a_{\nu, \vec{k}}(t)$ for the band ν and the Bloch wave vector \vec{k} . Then the plane wave expansion of the Bloch wave functions with expansion coefficients $\alpha_\nu(\vec{k} + \vec{g})$ is introduced via

$$\phi_{\nu, \vec{k}}(\vec{r}) = \sum_{\vec{g}} \frac{1}{\sqrt{V_c}} \alpha_\nu(\vec{k} + \vec{g}) e^{i(\vec{k} + \vec{g})\cdot\vec{r}}, \quad (1.38)$$

where the sum is over all reciprocal lattice vectors \vec{g} yielding

$$\begin{aligned} \gamma(\vec{p}|\vec{p}) &= \frac{1}{(2\pi)^3 V_c} \sum_{\nu, \vec{k}, \vec{g}} \int d\vec{r} e^{-i(\vec{k} + \vec{g} - \vec{p})\cdot\vec{r}} \alpha_\nu^*(\vec{k} + \vec{g}) \\ &\times \sum_{\nu', \vec{k}', \vec{g}'} \int d\vec{r}' e^{i(\vec{k}' + \vec{g}' - \vec{p}')\cdot\vec{r}'} \alpha_{\nu'}(\vec{k}' + \vec{g}') \langle a_{\nu, \vec{k}}^\dagger a_{\nu', \vec{k}'} \rangle. \end{aligned} \quad (1.39)$$

The position space integrations are performed utilizing the integral representation of the δ -function and with the definition of the mean occupation number for Bloch states

$$n_{\nu, \nu'}(\vec{k}) = \langle a_{\nu, \vec{k}}^\dagger a_{\nu', \vec{k}} \rangle \quad (1.40)$$

the electron momentum density can be expressed as

$$\gamma(\vec{p}|\vec{p}) = \sum_{\nu, \nu', \vec{k}} \sum_{\vec{g}} \alpha_{\nu}^*(\vec{k} + \vec{g}) \alpha_{\nu'}(\vec{k} + \vec{g}) n_{\nu, \nu'}(\vec{k}) \delta(\vec{k} + \vec{g} - \vec{p}). \quad (1.41)$$

In the case of non-interacting electrons all elements of the mean occupation number $n_{\nu, \nu'}$ are zero except the diagonal elements which have the value 1 for $p \leq p_F$, where p_F denotes the Fermi momentum. For interacting electrons the diagonal elements represent the mean occupation number of a Bloch state with wave vector \vec{k} in the band ν whereas the non-diagonal elements have non-zero values describing the mixing of different bands due to electron-electron correlation. Within the nearly free-electron approximation the contributions from the non-diagonal elements are assumed to be negligible and the electron momentum density is then given by

$$\gamma(\vec{p}|\vec{p}) = \sum_{\nu, \vec{k}} \sum_{\vec{g}} |\alpha_{\nu}(\vec{k} + \vec{g})|^2 n_{\nu}(\vec{k}) \delta(\vec{k} + \vec{g} - \vec{p}), \quad (1.42)$$

where correlation effects are predominantly associated with the occupation numbers while lattice and core orthogonalization effects are mainly assigned to the squared plane wave expansion coefficients [Lundqvist and Lydén 1971]. The electron momentum density and the corresponding valence Compton profile will be discussed as follows in terms of electron-electron correlation and electron-ion interaction.

Free electron gas

In the free electron gas model the electron-electron and electron-ion interaction is fully neglected. The radial symmetric electron momentum density is presented by

$$\gamma^f(\vec{p}|\vec{p}) = \Theta(p_F - |\vec{p}|), \quad (1.43)$$

where the Heavyside function $\Theta(p_F - |\vec{p}|)$ has the value 1 for $p < p_F$ and 0 otherwise. The resulting free electron valence Compton profile is an inverted parabola with $J(p_z) = \pi(p_F^2 - p_z^2)$.

Electron-electron correlation

With respect to electron-electron correlation the electron momentum density of the free electron like metals is described more properly within the model of the homogeneous interacting electron gas. Utilizing this model, $\gamma(\vec{p}|\vec{p})$ is separated into

a continuous function $\gamma^c(p)$ which characterizes the contribution of the electron-electron interaction and a Heavyside function with stepsize z_F at the Fermi momentum,

$$\gamma^h(\vec{p}|\vec{p}) = z_F \Theta(p_F - |\vec{p}|) + \gamma^c(|\vec{p}|) . \quad (1.44)$$

z_F is called the renormalization constant. The momentum distribution is still isotropic since lattice effects are not considered but now states with $p > p_F$ become occupied. Thus, the valence Compton profile exhibits tails and the sharp feature at p_F , referred to as Fermi break, is diminished. This reduction of the Fermi break is characterized by the value of z_F . Fig. 1.2 shows the electron momentum density and the Compton profile of the free electron gas (dashed line) and the homogeneous interacting electron gas (solid line) in the case of lithium.

Compton profiles calculated within the limits of the local density approximation (LDA) necessarily have to be corrected for correlation effects utilizing the so-called Lam-Platzman scheme [Lam and Platzman 1974]: For non-interacting and interacting electron distributions in Hartree-Fock approximation the momentum density is given by Eq. (1.36). When solving the Kohn-Sham equations within density functional theory (DFT) Eq. (1.36) has to be modified by adding the derivative of the total exchange correlation energy with respect to the individual electron energies. Then the isotropic term correcting LDA for electron-electron correlation is calculated utilizing the difference of the electron momentum density of the homogeneous interacting and the free electron gas, both as a function of the local density $\rho(\vec{r})$, via

$$\Delta\gamma_{[\rho(\vec{r})]}^{\text{LDA}}(\vec{p}|\vec{p}) = \int d\vec{r} \rho(\vec{r}) (\gamma_{[\rho(\vec{r})]}^h(\vec{p}|\vec{p}) - \gamma_{[\rho(\vec{r})]}^f(\vec{p}|\vec{p})) , \quad (1.45)$$

where the integral is over the unit cell. The electron momentum densities $\gamma_{[\rho(\vec{r})]}^h$ and $\gamma_{[\rho(\vec{r})]}^f$ as functional of the local density are normalized to one electron.

Electron-ion interaction

The influence of the electron-ion interaction on the electron momentum density can be clarified considering Eq. (1.42). By calculating the electron momentum density for momentum \vec{p} not only states with Bloch wave vector $\vec{k} = \vec{p}$ but also states having $\vec{k} + \vec{g} = \vec{p}$ contribute. These contributions, arising from the so-called Umklapp-processes for $\vec{g} \neq \vec{0}$, are called higher momentum components which modify the valence Compton profile by the appearance of tails at $p > p_F$ as illustrated in Fig. 1.2 by a dashed dotted line.

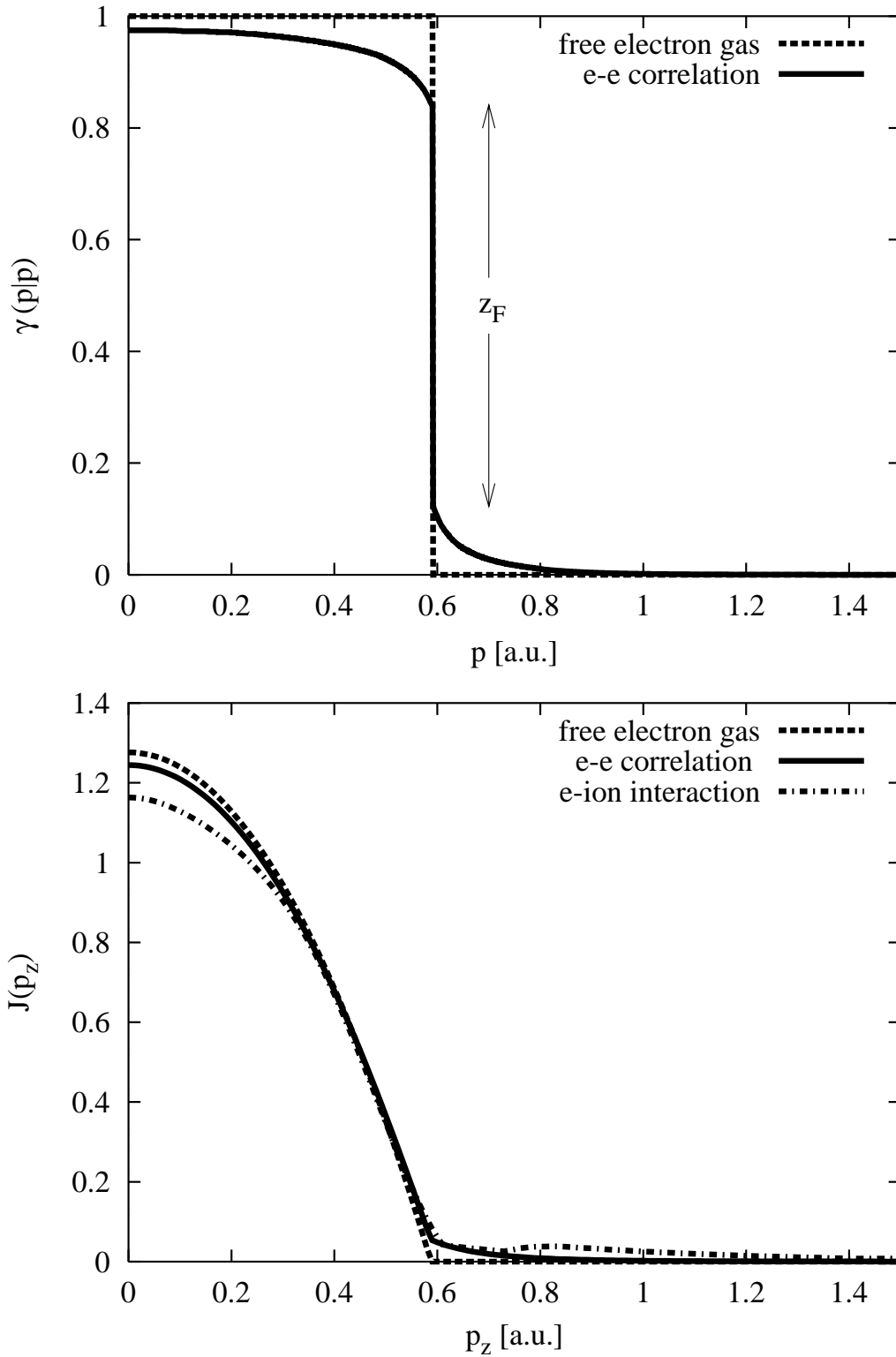


Figure 1.2: Electron momentum densities of the free (dashed line) and the homogeneous interacting electron gas (dotted line) with the corresponding valence Compton profiles in the case of lithium. The Compton profile influenced by the lattice potential due to Umklapp-processes is plotted for $\vec{q} \parallel [110]$ as dashed-dotted line. Electron-electron correlation and electron-ion interaction cause the extension of the Compton profile to $p_z > p_F$, p_F being the Fermi momentum.

Due to the influence of the lattice potential, momentum density is transferred out of the primary Fermi sphere of the extended zone scheme.

An appropriate theoretical treatment of the electron momentum density has to take into account both correlation and lattice effects.

1.4 Reciprocal form factor

The properties of the Compton profile are up to now discussed in momentum space. The reciprocal form factor $B(\vec{r})$, a quantity in position space, is introduced as the 3-dimensional Fourier transform of the electron momentum density [Pattison et al. 1977, Weyrich 1978] by

$$B(\vec{r}) = \int d\vec{p} \gamma(\vec{p} | \vec{p}) e^{i\vec{p} \cdot \vec{r}} \quad (1.46)$$

and can be represented in terms of the non-diagonal one-particle density matrix in position space $\gamma(\vec{r}' | \vec{r}' + \vec{r})$ via

$$B(\vec{r}) = \int d\vec{r}' \gamma(\vec{r}' | \vec{r}' + \vec{r}) . \quad (1.47)$$

$B(z)$ can be expressed as the one-dimensional Fourier transform of the Compton profile

$$B(z) = \int dp_z J(p_z) e^{ip_z z} , \quad (1.48)$$

so that by measuring many directional Compton profiles in order to obtain $B(\vec{r})$ on a fine grid in position space according to Eq. (1.48), the electron momentum density $\gamma(\vec{p} | \vec{p})$ can be reconstructed [Hansen 1980].

For valence electrons the $B(\vec{r})$ can be calculated utilizing the electron momentum density given by Eq. (1.42). Due to the δ -function the \vec{p} integration ends up with

$$B(\vec{r}) = \sum_{\nu, \vec{k}} \sum_{\vec{g}} |\alpha_{\nu}(\vec{k} + \vec{g})|^2 n_{\nu}(\vec{k}) e^{i(\vec{k} + \vec{g}) \cdot \vec{r}} . \quad (1.49)$$

This expression can be evaluated at positions of the lattice translation vectors \vec{R} utilizing the normalization condition of Bloch waves

$$\sum_{\vec{g}} |\alpha_{\nu}(\vec{k} + \vec{g})|^2 = 1 \quad (1.50)$$

and the definition of the occupation function

$$n(\vec{k}) = \sum_{\nu} n_{\nu}(\vec{k}) . \quad (1.51)$$

Replacing the sum over \vec{k} by a \vec{k} integration over the first Brillouin zone yields the following result

$$B(\vec{R}) = \frac{V_{\text{B}}}{(2\pi)^3} \int d\vec{k} n(\vec{k}) e^{i\vec{k}\cdot\vec{R}}, \quad (1.52)$$

where V_{B} is the volume of the first Brillouin zone. In the case of insulator and semiconductor $B(\vec{R}) = 0$ for all $\vec{R} \neq \vec{0}$, since each band is fully occupied or unoccupied neglecting thermal excitation and correlation. For metals the occupation function can be expanded into a Fourier series

$$n(\vec{k}) = \sum_{\vec{R}} B(\vec{R}) e^{-i\vec{k}\cdot\vec{R}} \quad (1.53)$$

which offers the possibility to reconstruct $n(\vec{k})$ from directional valence Compton profiles [Schülke 1977] utilizing the experimentally obtained values of the reciprocal form factor $B(\vec{R})$ at different lattice translation vectors. Eq. (1.52) shows that the reciprocal form factor is sensitive to the modifications of $n(\vec{k})$ caused by electron-electron correlation. This is of special significance for experimental studies of electron-electron correlation since the reciprocal form factor for small \vec{R} can be measured properly even with moderate momentum space resolution [Bauer and Schneider 1985].

Chapter 2

The dynamic structure factor at metallic densities

The subject of this chapter is the presentation of a theoretical formalism utilized for the calculation of the dynamic structure factor at metallic densities. The relation between the polarization function and the dynamic structure factor is shown and the polarization function is expressed in terms of the so-called proper polarization function. Utilizing the model of the homogeneous interacting electron gas, the modification of the free electron gas polarizability due to electron-electron correlation is described and discussed using self-energy and vertex corrections to the free-particle polarization. Finally, the consequences of the correlation corrections within the Compton scattering limit are emphasized.

2.1 Polarization function

The fundamental property which describes the excitation spectrum as measured by an inelastic x-ray scattering experiment is the polarization function $\chi(\vec{q}, \omega)$, which determines the response of the many-particle system to an external probe. The polarizability is directly related to the experimentally obtained quantity, the dynamic structure factor $S(\vec{q}, \omega)$, via the fluctuation-dissipation theorem.

2.1.1 Fluctuation-dissipation theorem

Starting from Eq. (1.5) the dynamical structure factor can be written, following van Hove [Van Hove 1954], as the Fourier transform in time and space of the pair distribution function $g(\vec{r}, t)$

$$S(\vec{q}, \omega) = \frac{N}{2\pi} \int \int d\vec{r} dt g(\vec{r}, t) e^{i(\vec{q}\cdot\vec{r} - \omega t)} \quad (2.1)$$

describing the correlation between a particle at time t and position $\vec{r} + \vec{r}'$ and a particle at $t = 0$ and position \vec{r}' , averaged over all possible positions \vec{r}' of the reference particle. Thus, the dynamic structure factor yields information about the correlated motion within the many-particle system caused by the probe. Pines and Nozières [Pines and Nozières 1966] showed the relation between the density fluctuations of the system specified by the dynamic structure factor $S(\vec{q}, \omega)$ and the dissipative part of the density-density response or polarization function $\chi(\vec{q}, \omega)$ via the fluctuation-dissipation theorem

$$S(\vec{q}, \omega) - S(-\vec{q}, -\omega) = -\frac{1}{\pi} \text{Im} \chi(\vec{q}, \omega). \quad (2.2)$$

$S(-\vec{q}, -\omega) = S(\vec{q}, \omega) e^{-\beta\omega}$ can be neglected since $\omega \gg 1/\beta = k_B T$, where k_B is the Boltzmann factor and T the temperature. In what follows the dielectric response of the system described by the dielectric function $\epsilon(\vec{q}, \omega)$ is related to the polarization function $\chi(\vec{q}, \omega)$ and to the proper polarization function $\chi_{\text{sc}}(\vec{q}, \omega)$.

2.1.2 Dielectric response

Response to an external field

The response of the many-particle system to an external potential is measured by the polarization or density-density response function $\chi(\vec{q}, \omega)$ as long as the coupling is considered to be weak. The polarization function is represented by

$$\chi(\vec{q}, \omega) = \frac{\langle \rho(\vec{q}, \omega) \rangle}{\varphi(\vec{q}, \omega)} \quad (2.3)$$

with the density fluctuations in Fourier space $\langle \rho(\vec{q}, \omega) \rangle$ characterizing the response of the system. The average is over the states of the system in presence of the test particle. $\varphi(\vec{q}, \omega)$ is the Fourier transform in space and time of the scalar potential acting on the electron system

$$\varphi(\vec{q}, \omega) = \frac{4\pi e^2}{|\vec{q}|^2} \rho_e(\vec{q}, \omega), \quad (2.4)$$

where $e\rho_e(\vec{q}, \omega)$ denotes the Fourier transform of the external charge density. $\chi(\vec{q}, \omega)$ depends only on the system properties in absence of the probe. The relation to the dielectric response of the many-particle system is then described utilizing the dielectric function $\epsilon(\vec{q}, \omega)$ via

$$\frac{1}{\epsilon(\vec{q}, \omega)} = 1 + \frac{\langle \rho(\vec{q}, \omega) \rangle}{\rho_e(\vec{q}, \omega)} \quad (2.5)$$

$$= 1 + v(q)\chi(\vec{q}, \omega) \quad (2.6)$$

with the Fourier transform of the bare Coulomb potential

$$v(q) = \frac{4\pi e^2}{|\vec{q}|^2}. \quad (2.7)$$

Response to a screened field

If the density fluctuations are induced by a screened charge the so-called proper polarization $\chi_{\text{sc}}(\vec{q}, \omega)$, which measures the response of the many-particle system to the screened external potential, is defined as

$$\chi_{\text{sc}}(\vec{q}, \omega) = \frac{\langle \rho(\vec{q}, \omega) \rangle}{\varphi(\vec{q}, \omega)/\epsilon(\vec{q}, \omega)} \quad (2.8)$$

$$= \chi(\vec{q}, \omega)\epsilon(\vec{q}, \omega). \quad (2.9)$$

Thus, the dielectric response of the system to a screened field is given by

$$\epsilon(\vec{q}, \omega) = 1 - v(q)\chi_{\text{sc}}(\vec{q}, \omega). \quad (2.10)$$

Proper polarization function

The relation between the polarization and the proper polarization function utilizing Eq. (2.6) and Eq. (2.10) is

$$\chi(\vec{q}, \omega) = \frac{\chi_{\text{sc}}(\vec{q}, \omega)}{1 - v(q)\chi_{\text{sc}}(\vec{q}, \omega)}, \quad (2.11)$$

where the polarization function $\chi(\vec{q}, \omega)$ describes the response of the many-particle system to an external field and the proper polarization function $\chi_{\text{sc}}(\vec{q}, \omega)$ specifies the response to a screened field. If $v(q) \ll 1$ the polarization function can be replaced by the proper polarization $\chi(\vec{q}, \omega) \approx \chi_{\text{sc}}(\vec{q}, \omega)$.

The proper polarization function $\chi_{\text{sc}}(\vec{q}, \omega)$ may be expressed by the one-particle Green's function $G(\vec{p}, \epsilon)$ [Awa et al. 1981]

$$\chi_{\text{sc}}(\vec{q}, \omega) = 2 \int \frac{d\epsilon}{(2\pi i)} \int \frac{d\vec{p}}{(2\pi)^3} G(\vec{p}, \epsilon) G(\vec{p} + \vec{q}, \epsilon + \omega) \tilde{\Lambda}(\vec{p}, \epsilon; \vec{q}, \omega) \quad (2.12)$$

with the proper vertex function $\tilde{\Lambda}(\vec{p}, \epsilon; \vec{q}, \omega)$ represented by

$$\begin{aligned} \tilde{\Lambda}(\vec{p}, \epsilon; \vec{q}, \omega) = & 1 + \int \frac{d\epsilon'}{(2\pi i)} \int \frac{d\vec{p}'}{(2\pi)^3} I(\vec{p}, \epsilon, \vec{p}', \epsilon'; \vec{q}, \omega) \\ & \times G(\vec{p}', \epsilon') G(\vec{p}' + \vec{q}, \epsilon' + \omega) \tilde{\Lambda}(\vec{p}', \epsilon'; \vec{q}, \omega), \end{aligned} \quad (2.13)$$

where $I(\vec{p}, \epsilon, \vec{p}', \epsilon'; \vec{q}, \omega)$ is the irreducible interaction term. According to Hedin [Hedin 1965] $I(\vec{p}, \epsilon, \vec{p}', \epsilon'; \vec{q}, \omega)$ can be expressed by the momentum and energy dependent screened Coulomb potential

$$I_{\text{sc}}^{\text{C}}(\vec{p}, \epsilon, \vec{p}', \epsilon') = \frac{v(\vec{p}' - \vec{p})}{\epsilon^{\text{RPA}}(\vec{p}' - \vec{p}, \epsilon' - \epsilon)}, \quad (2.14)$$

where the screening is described by the Lindhard dielectric function $\epsilon^{\text{RPA}}(\vec{p}' - \vec{p}, \epsilon' - \epsilon)$ within the random phase approximation (RPA) [Lindhard 1954] which is discussed in detail within section 2.2.3. The bare Coulomb potential cannot be seen as a reasonable approximation as long as the polarizability of the system is large, especially at metallic densities. The interaction is mediated by the electron system itself via plasmon excitation and deexcitation. Two different corrections to the free-particle polarizability have to be distinguished, one due to the interaction of the particle with the hole left behind (particle-hole vertex correction) and the other due to the interaction of the excited particle (hole) with the rest of the many-particle system (self-energy correction), which is caused by the polarization originating from the existence of the excited particle (hole). The self-energy contribution to the polarization function is treated by using the fully dressed one-particle Green's function $G^{\text{SE}}(\vec{p}, \epsilon) = G^0(\vec{p}, \epsilon + \Sigma(\vec{p}, \epsilon))$ instead of $G^0(\vec{p}, \epsilon)$, the Green's function of a free particle, $\Sigma(\vec{p}, \epsilon)$ being the self-energy of the quasiparticle. $G^0(\vec{p}, \epsilon)$ is given by

$$G^0(\vec{p}, \epsilon) = \left(\frac{\Theta(E_{\text{F}} - \epsilon_{\vec{p}})}{\epsilon - \epsilon_{\vec{p}} - i\eta} + \frac{\Theta(\epsilon_{\vec{p}} - E_{\text{F}})}{\epsilon - \epsilon_{\vec{p}} + i\eta} \right), \quad (2.15)$$

where $\epsilon_{\vec{p}} = p^2/2m$ denotes the energy of a free particle, E_{F} is the Fermi energy and $\eta = 0^+$. The vertex correction comprises the calculation of the proper vertex function in Eq. (2.13) utilizing the interaction term $I_{\text{sc}}^{\text{C}}(\vec{p}, \epsilon, \vec{p}', \epsilon')$. The

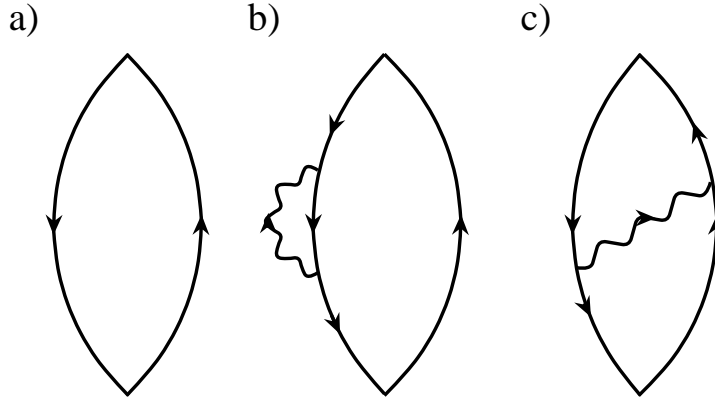


Figure 2.1: Feynman diagrams for the calculation of the proper polarization function: (a) free-particle polarizability, (b) self-energy correction in first order and (c) vertex correction in first order.

vertex correction is known to cancel to a certain extent the self-energy correction [Singwi and Tosi 1981] which emphasizes the necessity of a combined treatment of both corrections in calculating the polarization function. To obtain a consistent calculation, the same approximation for the irreducible interaction term has to be used both when calculating the self-energy correction and when calculating the vertex correction, namely $I_{sc}^C(\vec{p}, \epsilon, \vec{p}', \epsilon')$.

Fig. 2.1 shows the three different types of Feynman diagrams contributing to the calculation of the proper polarization function. The solid lines represent the free-particle Green's functions $G^0(\vec{p}, \epsilon)$ and the wiggly line the screened Coulomb interaction $I_{sc}^C(\vec{p}, \epsilon, \vec{p}', \epsilon')$. Fig. 2.1(a) describes the free-particle polarization. Diagrams of type (b), where the screened Coulomb potential acts on the quasiparticle itself, denote the self-energy type corrections to the polarizability. Diagrams of type (c), where the interaction acts between the particle and the hole, represent the type of vertex corrections. Only the first order terms in the screened Coulomb interaction are shown.

2.2 Self-energy effects

In what follows, the self-energy contribution to the free-particle polarizability is discussed and the limit of the free-particle approximation utilizing the free-particle Green's function is derived ending up with the well known Lindhard expression. Furthermore, a concept is presented to consider the finite lifetime of the particle corresponding to the imaginary part of the self-energy within the Compton scattering limit.

2.2.1 Spectral density function

The fully dressed one-particle Green's function $G^{\text{SE}}(\vec{p}, \epsilon)$ takes into account the self-energy contribution to the proper polarization function up to all orders in the Coulomb potential screened by the RPA dielectric function [Holas et al. 1979]. This is possible since the series of type (b) diagrams can be summed up into a geometric series which is demonstrated in Appendix A. $G^{\text{SE}}(\vec{p}, \epsilon)$ can be expressed utilizing the spectral representation of the self-energy $\Sigma(\vec{p}, E)$ via the spectral density function $A(\vec{p}, E)$

$$G^{\text{SE}}(\vec{p}, \epsilon) = \frac{1}{2\pi} \left(\int_{-\infty}^{E_{\text{F}}} \frac{A(\vec{p}, E) dE}{\epsilon - E - i\eta} + \int_{E_{\text{F}}}^{\infty} \frac{A(\vec{p}, E) dE}{\epsilon - E + i\eta} \right) \quad (2.16)$$

with

$$A(\vec{p}, E) = -2 \text{Im} G^{\text{SE}}(\vec{p}, E) \quad (2.17)$$

$$= -2 \frac{\text{Im} \Sigma(\vec{p}, E)}{(E - \epsilon_{\vec{p}} - \text{Re} \Sigma(\vec{p}, E))^2 + (\text{Im} \Sigma(\vec{p}, E))^2} . \quad (2.18)$$

The spectral density function $A(\vec{p}, E)$ describes the probability to find the many-particle system in a state with energy E ($-E$) above the ground state right after injection of a particle (hole) with momentum \vec{p} . $\text{Im} \Sigma(\vec{p}, E)$ is the decay-probability of the excitation of the system at energy E and $\text{Re} \Sigma(\vec{p}, E)$ yields the deviation of the energy E of the correlated system from the free-particle energy $\epsilon_{\vec{p}}$.

Fig. 2.2 presents $\text{Im} \Sigma(\vec{p}, E)$ and $\text{Re} \Sigma(\vec{p}, E)$ as a function of energy E for different momenta \vec{p} calculated for $r_s = 3.25$, where r_s is the free electron gas parameter. The crossings of the straight line with $\text{Re} \Sigma(\vec{p}, E)$ give the solutions of the Dyson equation $E - \epsilon_{\vec{p}} = \text{Re} \Sigma(\vec{p}, E)$. From Eq. (2.18) it follows that $A(\vec{p}, E)$ has a significant spectral weight for the solutions of the Dyson equation if the corresponding

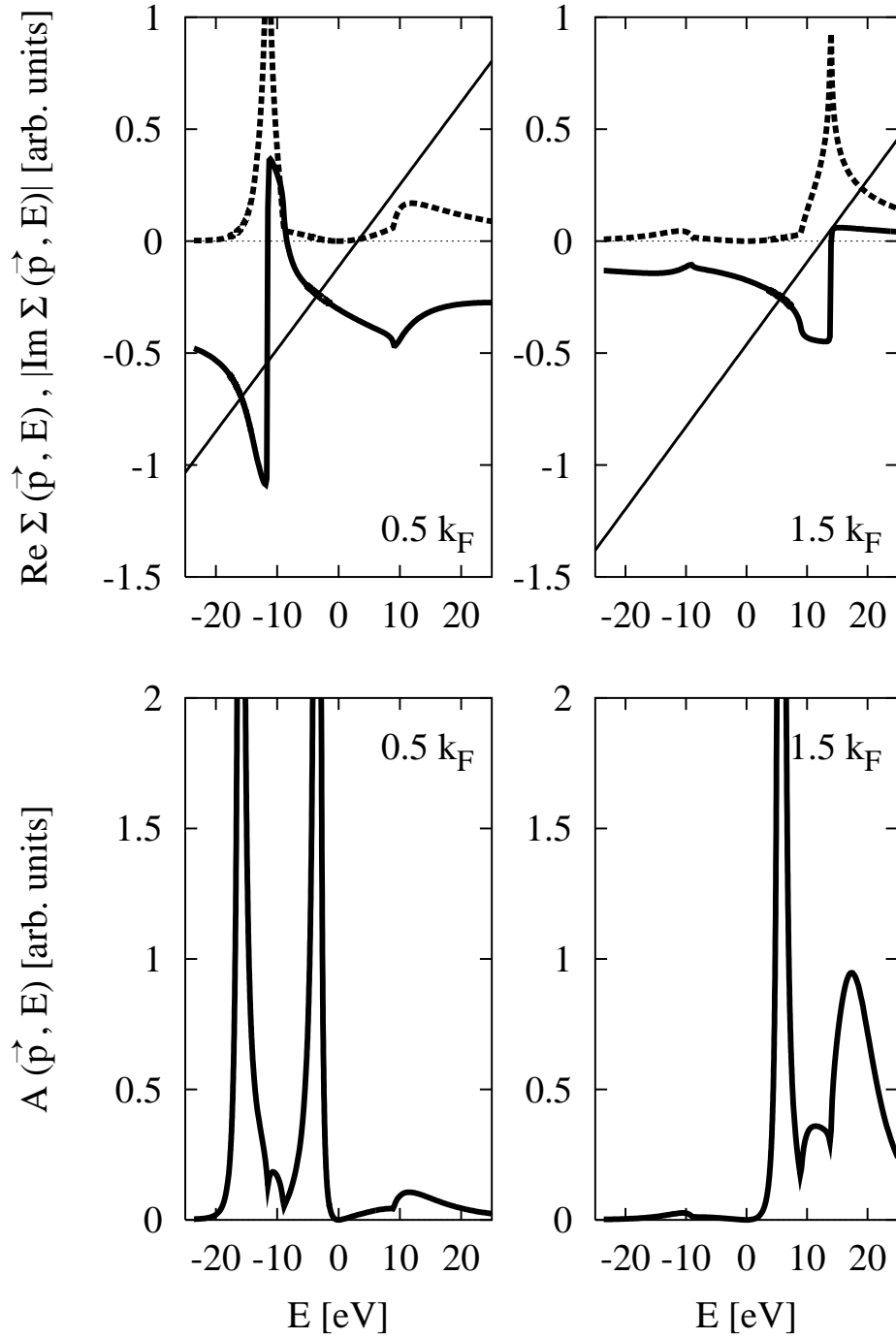


Figure 2.2: Real part (solid) and the absolute value of the imaginary part (dashed) of the self-energy together with the Dyson plot $\epsilon = E - \epsilon_{\vec{p}}$ (thin solid line) for different momenta \vec{p} compared to the corresponding spectral density function $A(\vec{p}, E)$, calculated for lithium having a free electron gas parameter of $r_s = 3.25$.

values of $\text{Im} \Sigma(\vec{p}, E)$ are small, otherwise the excitation is strongly damped due to the imaginary part of the self-energy characterizing the small lifetime of the excitation. Typically, the spectral density function shows one quasiparticle peak and two side bands. The quasiparticle peak describes the excitation probability of the particle or the hole, respectively. For $|\vec{p}| < p_F$ a second excitation gets dominant spectral weight. This excitation, the so-called plasmaron, is due to a hole state modified by a coherent contribution from hole-plasmon pair states [Lundqvist 1967].

2.2.2 Self-energy correction

To focus on the influence of the self-energy to the proper polarization function the vertex correction is neglected. Then Eq. (2.12) is calculated in zeroth order while the proper polarization function has to be expressed in terms of the fully dressed Green's function $G^{\text{SE}}(\vec{p}, \epsilon)$, which includes the self-energy contribution to the free-particle polarizability up to all orders, yielding

$$\chi_{\text{sc}}^{\text{SE}}(\vec{q}, \omega) = 2 \int \frac{d\epsilon}{(2\pi i)} \int \frac{d\vec{p}}{(2\pi)^3} G^{\text{SE}}(\vec{p}, \epsilon) G^{\text{SE}}(\vec{p} + \vec{q}, \epsilon + \omega). \quad (2.19)$$

$G^{\text{SE}}(\vec{p}, \epsilon)$ is replaced using Eq. (2.16) and the ϵ integration is performed by calculating the resulting Cauchy integrals. Finally, the Heavyside function $\Theta(x - x')$ is introduced ending up with

$$\begin{aligned} \chi_{\text{sc}}^{\text{SE}}(\vec{q}, \omega) = & 2 \int \frac{d\vec{p}}{(2\pi)^3} \int \frac{dE}{(2\pi)} \int \frac{dE'}{(2\pi)} \\ & \times \left(\frac{A(\vec{p}, E)A(\vec{p} + \vec{q}, E')}{\omega + E - E' + i\eta} \Theta(E_F - E)\Theta(E' - E_F) \right. \\ & \left. - \frac{A(\vec{p}, E)A(\vec{p} + \vec{q}, E')}{\omega + E - E' - i\eta} \Theta(E - E_F)\Theta(E_F - E') \right). \quad (2.20) \end{aligned}$$

$\text{Im} \chi_{\text{sc}}^{\text{SE}}(\vec{q}, \omega)$, the quantity which is related to the experiment via the dynamic structure factor, is calculated for $\eta \rightarrow 0$ by introducing the δ -function $\delta(\omega + E - E')$ and performing the E' integration, resulting in

$$\text{Im} \chi_{\text{sc}}^{\text{SE}}(\vec{q}, \omega) = - \int \frac{d\vec{p}}{(2\pi)^3} \int_{E_F - \omega}^{E_F} \frac{dE}{(2\pi)} A(\vec{p}, E)A(\vec{p} + \vec{q}, E + \omega), \quad (2.21)$$

where the E integration limits are determined by the evaluation of the corresponding Heaviside functions.

As a main result of the calculus it can be stressed, that the excitation spectrum characterized by $\text{Im} \chi_{\text{sc}}^{\text{SE}}(\vec{q}, \omega)$ is given by the convolution of the spectral density function of the hole state $A(\vec{p}, E)$ and the particle state $A(\vec{p} + \vec{q}, E + \omega)$ for given momentum transfer \vec{q} and energy transfer ω . Before the consequences of the self-energy correction to the Compton excitation spectrum are discussed, the proper polarization function in the Lindhard approximation will be derived.

2.2.3 Lindhard approximation

For the case of a non-interacting (free) electron gas the spectral density function for a free particle $A^0(\vec{q}, \omega)$, which determines the excitation probability of quasiparticle states having infinite lifetimes, can be written as

$$A^0(\vec{p}, E) = 2\pi\delta(E - \epsilon_{\vec{p}}). \quad (2.22)$$

This relation is obtained from Eq. (2.18) setting $\text{Re} \Sigma(\vec{p}, E) = 0$ and $\text{Im} \Sigma(\vec{p}, E) \rightarrow 0^-$ and leads to the free-particle Green's function $G^0(\vec{p}, \epsilon)$ of Eq. (2.15). Then the well-known Lindhard equation for the proper polarization function is obtained [Green et al. 1987] via

$$\begin{aligned} \chi_{\text{sc}}^0(\vec{q}, \omega) &= 2 \int \frac{d\epsilon}{(2\pi i)} \int \frac{d\vec{p}}{(2\pi)^3} G^0(\vec{p}, \epsilon) G^0(\vec{p} + \vec{q}, \epsilon + \omega) \\ &= 2 \int \frac{d\vec{p}}{(2\pi)^3} \left(\frac{\Theta(E_{\text{F}} - \epsilon_{\vec{p}})\Theta(\epsilon_{\vec{p}+\vec{q}} - E_{\text{F}})}{\omega + \epsilon_{\vec{p}} - \epsilon_{\vec{p}+\vec{q}} + i\eta} - \frac{\Theta(\epsilon_{\vec{p}} - E_{\text{F}})\Theta(E_{\text{F}} - \epsilon_{\vec{p}+\vec{q}})}{\omega + \epsilon_{\vec{p}} - \epsilon_{\vec{p}+\vec{q}} - i\eta} \right) \\ &= 2 \sum_{|\vec{p}'| < p_{\text{F}} < |\vec{p}'+\vec{q}|} \left(\frac{1}{\omega + \epsilon_{\vec{p}'} - \epsilon_{\vec{p}'+\vec{q}} + i\eta} + \frac{1}{-\omega + \epsilon_{\vec{p}'} - \epsilon_{\vec{p}'+\vec{q}} + i\eta} \right). \quad (2.23) \end{aligned}$$

The density-density response $\chi_{\text{sc}}^0(\vec{q}, \omega)$ for a single particle-hole pair is the dominant contribution to $\chi_{\text{sc}}(\vec{q}, \omega)$ at high electron densities and leads to the RPA result for the polarization function $\chi(\vec{q}, \omega)$ via the sum over the electron-hole pair excitations coupled by the bare Coulomb potential (see Eq. (2.11)). Utilizing Eq. (2.10) the RPA dielectric function is given by

$$\epsilon^{\text{RPA}}(\vec{q}, \omega) = 1 - v(q) \chi_{\text{sc}}^0(\vec{q}, \omega). \quad (2.24)$$

2.2.4 Self-energy effects on the dynamic structure factor in the Compton limit

The dynamic structure factor $S(\vec{q}, \omega)$ can be expressed by the proper polarization function in terms of the spectral density function for the excited particle and the remaining hole using the fluctuation-dissipation theorem with Eq. (2.21)

$$S^{\text{SE}}(\vec{q}, \omega) = \frac{1}{\pi} \int \frac{d\vec{p}}{(2\pi)^3} \int_{E_{\text{F}}-\omega}^{E_{\text{F}}} \frac{dE}{(2\pi)} A(\vec{p}, E) A(\vec{p} + \vec{q}, E + \omega), \quad (2.25)$$

where $S^{\text{SE}}(-\vec{q}, -\omega)$ is negligible and $\chi(\vec{q}, \omega) = \chi_{\text{sc}}^{\text{SE}}(\vec{q}, \omega)$ for $v(q) \ll 1$. According to the impulse approximation the energy of the ground state E is replaced by the energy of a free particle $\epsilon_{\vec{p}} = p^2/2m$ in the spectral density function of the final state and the energy shift due to the real part of the self-energy is neglected, $\text{Re} \Sigma(\vec{p} + \vec{q}, \epsilon_{\vec{p}} + \omega) = 0$, yielding

$$A_{\text{IA}}(\vec{p} + \vec{q}, \epsilon_{\vec{p}} + \omega) = \frac{-2 \text{Im} \Sigma(\vec{p} + \vec{q}, \epsilon_{\vec{p}} + \omega)}{(\epsilon_{\vec{p}} + \omega - \epsilon_{\vec{p}+\vec{q}})^2 + (\text{Im} \Sigma(\vec{p} + \vec{q}, \epsilon_{\vec{p}} + \omega))^2}. \quad (2.26)$$

The energy difference between the initial and the final state is given by the energy difference of free-particle states, $\omega = \epsilon_{\vec{p}+\vec{q}} - \epsilon_{\vec{p}}$, so that $A_{\text{IA}}(\vec{p} + \vec{q}, \epsilon_{\vec{p}} + \omega)$ describes a free-particle final state having a finite lifetime due to the imaginary part of the self-energy. Finally, the fully correlated electron momentum density $\gamma(\vec{p} | \vec{p})$ is introduced [Mahan 1981] via

$$\gamma(\vec{p} | \vec{p}) = \frac{2}{(2\pi)^3} \int_{-\infty}^{E_{\text{F}}} \frac{dE}{2\pi} A(\vec{p}, E). \quad (2.27)$$

In the Compton limit, $\omega \gg E_{\text{F}}$, one ends up with

$$S_{\text{IA}}^{\text{SE}}(\vec{q}, \omega) = \frac{1}{2\pi} \int d\vec{p} \gamma(\vec{p} | \vec{p}) A_{\text{IA}}(\vec{p} + \vec{q}, \epsilon_{\vec{p}} + \omega), \quad (2.28)$$

the 3-dimensional convolution of the fully correlated electron momentum density $\gamma(\vec{p} | \vec{p})$ with the spectral density function of the excited particle in the limit of Compton scattering $A_{\text{IA}}(\vec{p} + \vec{q}, \epsilon_{\vec{p}} + \omega)$.

Neglecting the self-energy effects within this approximation by setting $\text{Im} \Sigma(\vec{p} + \vec{q}, \epsilon_{\vec{p}} + \omega) \rightarrow 0^-$ yields

$$\begin{aligned} A_{\text{IA}}^0(\vec{p} + \vec{q}, \epsilon_{\vec{p}} + \omega) &= 2\pi\delta(\omega + \epsilon_{\vec{p}} - \epsilon_{\vec{p}+\vec{q}}) \\ &= 2\pi\delta(\omega - \vec{p} \cdot \vec{q}/m - q^2/2m) \end{aligned} \quad (2.29)$$

the energy conservation of the Compton scattering process. Thus, the direct relation between the dynamic structure factor $S(\vec{q}, \omega)$ and the Compton profile $J(p_z)$ using Eq. (1.27) with \vec{q} pointing into z -direction is given by

$$S_{\text{IA}}(q, \omega = p_z q/m + q^2/2m) = \frac{m}{q} J(p_z). \quad (2.30)$$

Until now, the theoretical treatment of the self-energy influence in calculating the proper polarization function was discussed in terms of the spectral density function within the model of the free electron gas in the Lindhard approximation and in the limit of Compton scattering. However, the excitation spectrum characterized by the imaginary part of the proper polarization function is not only affected by the self-energy of the quasiparticles but also by the interaction between the excited particle and the remaining hole, which will be examined as follows by calculating the vertex correction.

2.3 Vertex correction

The interaction between the excited particle and the hole is described by the vertex correction to the proper polarization function $\chi_{sc}(\vec{q}, \omega)$. First, the vertex correction is discussed in the limit of the local field approximation. Then the first order vertex correction utilizing the Coulomb interaction $I_{sc}^C(\vec{p}, \epsilon, \vec{p}', \epsilon')$ screened by the RPA dielectric function is analyzed and one type of second order vertex correction is presented.

2.3.1 Local field approximation

The local field approximation is a correction to the free-particle proper polarization function $\chi_{sc}^0(\vec{q}, \omega)$ assuming a screened Coulomb interaction $I(q, \omega)$ between the excited particle and the hole

$$I(\vec{p}, \epsilon, \vec{p}', \epsilon'; \vec{q}, \omega) = 2I(q, \omega) = -2v(q)g(q, \omega), \quad (2.31)$$

$g(q, \omega)$ being the local field, which accounts for the screening by an effective correction to the bare Coulomb potential $v(q)$ [Green et al. 1987]. Within this approximation the interaction is not mediated by the many-particle system, which means that both the momentum and the energy of the excited particle and the hole are not changed due to the interaction between these quasiparticles. If either a time dependent or a static local field is used to describe the interaction, Eq. (2.12) can be expressed as a geometric series, shown in Appendix B, yielding

$$\chi_{sc}^{LF}(\vec{q}, \omega) = \frac{\chi_{sc}^0(\vec{q}, \omega)}{1 + v(q)g(q, \omega)\chi_{sc}^0(\vec{q}, \omega)}. \quad (2.32)$$

In this approximation the vertex correction is considered up to all orders in $I(q, \omega)$.

If the interaction between the excited particle and the hole is mediated by the rest of the many-particle system, energy and momentum is transferred between the quasiparticles, which means that the irreducible interaction term becomes dependent on $\vec{p}, \epsilon, \vec{p}', \epsilon'$. Then Eq. (2.12) can no longer be written as the sum of a geometric series and the different contributions to the vertex correction have to be calculated separately.

Using the time dependent or the static local field is the only approximation which decouples the Green's function integrals.

2.3.2 First and second order vertex correction

The calculation of the vertex correction is performed using $I_{\text{sc}}^{\text{C}}(\vec{p}, \epsilon, \vec{p}', \epsilon')$ so that the self-energy correction and the vertex correction are consistent, based on the same theoretical approximation for the interaction term in Eq. (2.13). The corresponding Feynman diagrams are presented in Fig. 2.3.

Starting from Eq. (2.12) with the fully dressed Green's functions $G^{\text{SE}}(\vec{p}, \epsilon)$, $G^{\text{SE}}(\vec{p} + \vec{q}, \epsilon + \omega)$ and using the Coulomb potential screened by the Lindhard dielectric function, the first order vertex correction is calculated applying the diagram representation of Fig. 2.3(b) as follows

$$\begin{aligned} \chi_{\text{sc}}^{\text{VE}_1}(\vec{q}, \omega) = & 2 \int \frac{d\epsilon}{(2\pi i)} \int \frac{d\vec{p}}{(2\pi)^3} G^{\text{SE}}(\vec{p}, \epsilon) G^{\text{SE}}(\vec{p} + \vec{q}, \epsilon + \omega) \\ & \times \int \frac{d\epsilon'}{(2\pi i)} \int \frac{d\vec{p}'}{(2\pi)^3} \frac{v(\vec{p}' - \vec{p})}{\epsilon^{\text{RPA}}(\vec{p}' - \vec{p}, \epsilon' - \epsilon)} \\ & \times G^{\text{SE}}(\vec{p}', \epsilon') G^{\text{SE}}(\vec{p}' + \vec{q}, \epsilon' + \omega). \end{aligned} \quad (2.33)$$

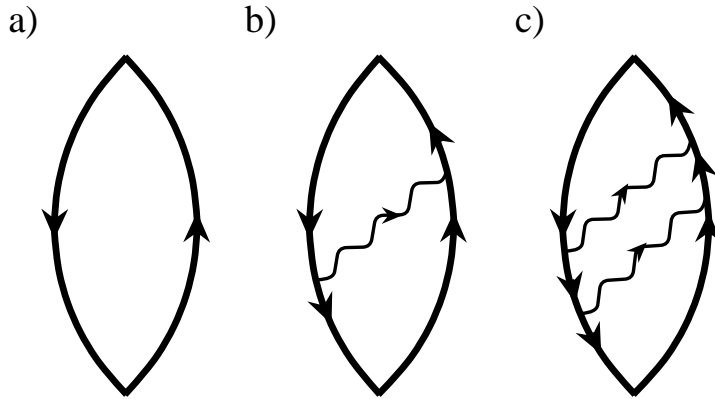


Figure 2.3: The fully self-energy corrected particle-hole bubble is shown in diagram (a). Diagrams (b) and (c) present the first and the second order vertex correction to the proper polarization function. The thick solid lines denote the fully dressed Green's functions $G^{\text{SE}}(\vec{p}, \epsilon)$ including the total self-energy correction and the wiggly line represents the screened Coulomb interaction $I_{\text{sc}}^{\text{C}}(\vec{p}, \epsilon, \vec{p}', \epsilon')$.

The calculation of the second order vertex correction (Fig. 2.3(c)) leads to

$$\begin{aligned}
\chi_{\text{sc}}^{\text{VE}_2}(\vec{q}, \omega) = & 2 \int \frac{d\epsilon}{(2\pi i)} \int \frac{d\vec{p}}{(2\pi)^3} G^{\text{SE}}(\vec{p}, \epsilon) G^{\text{SE}}(\vec{p} + \vec{q}, \epsilon + \omega) \\
& \times \int \frac{d\epsilon'}{(2\pi i)} \int \frac{d\vec{p}'}{(2\pi)^3} \frac{v(\vec{p}' - \vec{p})}{\epsilon^{\text{RPA}}(\vec{p}' - \vec{p}, \epsilon' - \epsilon)} \\
& \quad \times G^{\text{SE}}(\vec{p}', \epsilon') G^{\text{SE}}(\vec{p}' + \vec{q}, \epsilon' + \omega) \\
& \times \int \frac{d\epsilon''}{(2\pi i)} \int \frac{d\vec{p}''}{(2\pi)^3} \frac{v(\vec{p}'' - \vec{p}')}{\epsilon^{\text{RPA}}(\vec{p}'' - \vec{p}', \epsilon'' - \epsilon')} \\
& \quad \times G^{\text{SE}}(\vec{p}'', \epsilon'') G^{\text{SE}}(\vec{p}'' + \vec{q}, \epsilon'' + \omega). \tag{2.34}
\end{aligned}$$

The vertex corrections $\chi_{\text{sc}}^{\text{VE}_1}$ and $\chi_{\text{sc}}^{\text{VE}_2}$ obviously include the time inverted counterparts of the diagrams (b) and (c) of Fig. 2.3. Within the utilized approximation for $I(\vec{p}, \epsilon, \vec{p}', \epsilon')$ in Eq. (2.13) only contributions to the basic self-energy corrected free-particle polarization diagram, shown in Fig. 2.3(a), are included. Beyond this type of second order vertex correction there exist diagrams including two particle-hole bubbles interacting via plasmon excitation and deexcitation in second order of the screened Coulomb potential, which are neglected within the presented theoretical approach [Green et al. 1985] so that a second order treatment of this kind is just of exemplary nature.

Chapter 3

Final state interaction in Compton scattering from lithium

The availability of high intense synchrotron radiation allows for a momentum space resolution in Compton scattering experiments down to a few percent of the Fermi momentum, which gives the unique possibility to investigate experimentally correlation induced features of the electron momentum density close to the Fermi momentum. However, this high momentum space resolution along with an appropriate statistical accuracy has been obtained until now only at low incident x-ray energies around 10 keV [Hämäläinen et al. 1996]. At these low incident energies the validity of the impulse approximation becomes a serious problem in interpreting Compton profiles. Indeed, measurements of the Compton profile of e.g. neon, helium [Wong et al. 1982] and aluminium [Holt et al. 1979] resulted in an asymmetry of the Compton profile with respect to $p_z = 0$ a.u. and a lot of effort has been spent to explain these deviations from the impulse approximation on the theoretical side [Issolah et al. 1988, Holm and Ribberfors 1989].

The aim of the present study is to examine how final state interaction effects affect the valence Compton profile of lithium and thus, how the deviations from the impulse approximation modify the results of a Compton profile measurement and the information on the electron momentum density drawn from it. A systematic study of the validity of the impulse approximation is urgently requested since Schülke et al. [Schülke et al. 1996] pointed out that final state interactions play an important role in the interpretation of valence Compton profiles, even for simple metals like lithium, while it was generally assumed so far that the valence Compton profile measured at incident photon energies around 10 keV can be discussed within the limits of the impulse approximation [Platzman and Tzoar 1965]. The investigation, how final state interaction effects influence the features of the electron momentum density around the Fermi momentum of lithium, is of special interest since strong discrepancies between experimentally obtained valence Compton profiles [Sakurai et al. 1995, Schülke et al. 1996] and calculations utilizing LDA [Sakurai et al. 1995] or Quantum Monte Carlo (QMC) [Filippi and Ceperley 1999]

schemes have been found as far as the Fermi break is concerned.

In this chapter the high resolution Compton scattering experiment on single crystalline lithium is described. The results of the experiment are discussed in terms of final state interaction, i.e. self-energy and vertex correction. Finally, the valence Compton profiles are analyzed utilizing the reciprocal form factor.

3.1 Experiment

The experiment was performed at the inelastic x-ray scattering beamline G3 of HASYLAB (Hamburger Synchrotronstrahlungslabor) at DESY (Deutsches Elektronen Synchrotron). The experimental setup is represented followed by a description of the data evaluation procedure extracting the valence Compton profiles from the measured spectra.

3.1.1 Experimental setup

The experimental setup is illustrated in Fig. 3.1. The synchrotron radiation from a bending magnet source was monochromatized utilizing a Ge(311) double crystal monochromator and the scattered photons were analyzed in Rowland geometry using a spherically bent Ge(800) analyzer crystal and detected by a Ge detector [Schülke and Nagasawa 1984]. Two monitor detectors were used, a Ge and a NaI detector detecting the radiation from the sample and from a Kapton scattering foil, respectively.

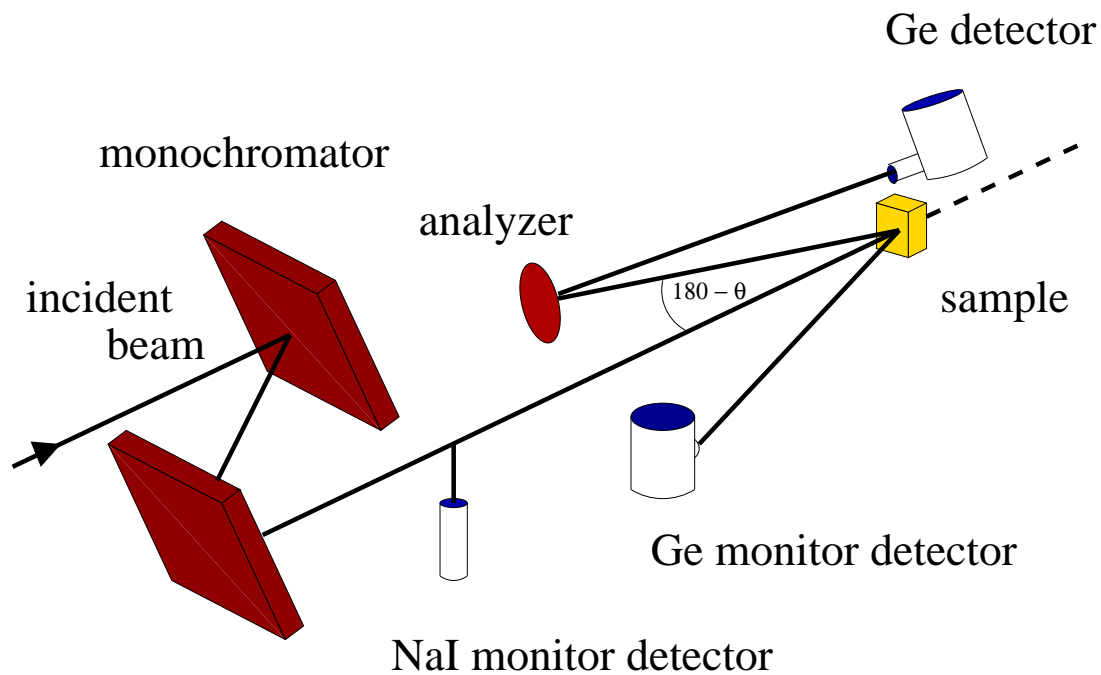


Figure 3.1: Experimental setup of the inelastic x-ray scattering beamline G3 of HASYLAB/DESY utilizing inverse geometry. Sample, analyzer and Ge detector are fixed on the Rowland circle. The incident energy is varied using a double crystal monochromator.

The measurement was accomplished using the so-called inverse geometry, i.e. by scanning the incident energy ω_1 and keeping the analyzer energy fixed at $\omega_2 = 8789$ eV corresponding to a Bragg angle of 86° , so that the Compton profile was measured as a function of the incident energy.

The lithium single crystal was a cuboid with 6.5 mm side length and 9 mm height. The crystallographic orientation of the single crystal, which is sketched in Fig. 3.2, was tested utilizing Laue diffraction in transmission geometry and was precisely adjusted with a goniometer setup. Lithium oxidizes in a humid atmosphere and loses its metallic shine of the surface. Therefore, the sample was stored within water-free paraffin oil. At the beginning of the measurement the oil was removed using heptan. Then the sample was etched in highly pure methanol to metallic luster and again cleaned by xylol. Just after the etching process the lithium sample was mounted into the scattering chamber, which was evacuated to 10^{-5} mbar to avoid oxidation. The sample retained the metallic shine until the end of the measurements, so that a contamination of the sample surface by oxidation which could influence the experimental result can be ruled out.

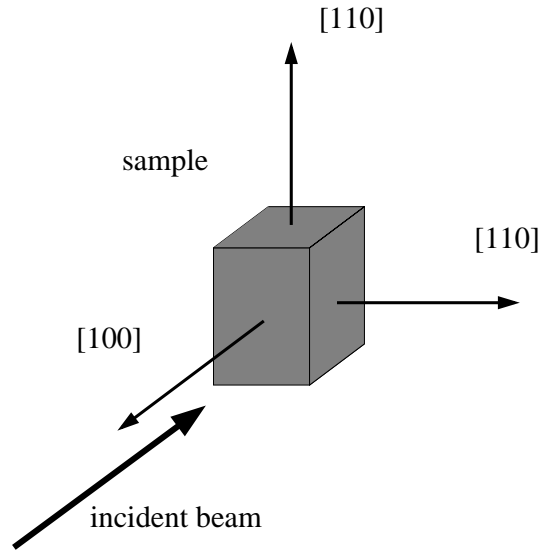


Figure 3.2: Crystallographic orientation of the lithium single crystal.

Directional Compton profiles were measured with scattering vector $\vec{q} \parallel [100], [110], [111]$ and $[311]$ at a scattering angle of $\theta = 164^\circ$. The incident energy was scanned from 8770 eV to 9650 eV with a stepsize of 0.7 eV. The momentum transfer $|\vec{q}|$ ranged from 4.66 a.u. to 5.12 a.u. and reached the value of 4.83 a.u. at the maximum of the Compton profile. For each direction of \vec{q} 7 - 8 single spectra were measured, summed up and normalized to the monitor signal of the NaI detector detecting the scattered photons from the Kapton foil. Fig. 3.3 shows a raw spectrum, which consist of the quasi-elastic line, the lithium K-edge

and the total Compton profile. The total Compton profile can be separated into two components, the broad core electron contribution and the valence electron Compton profile, respectively.

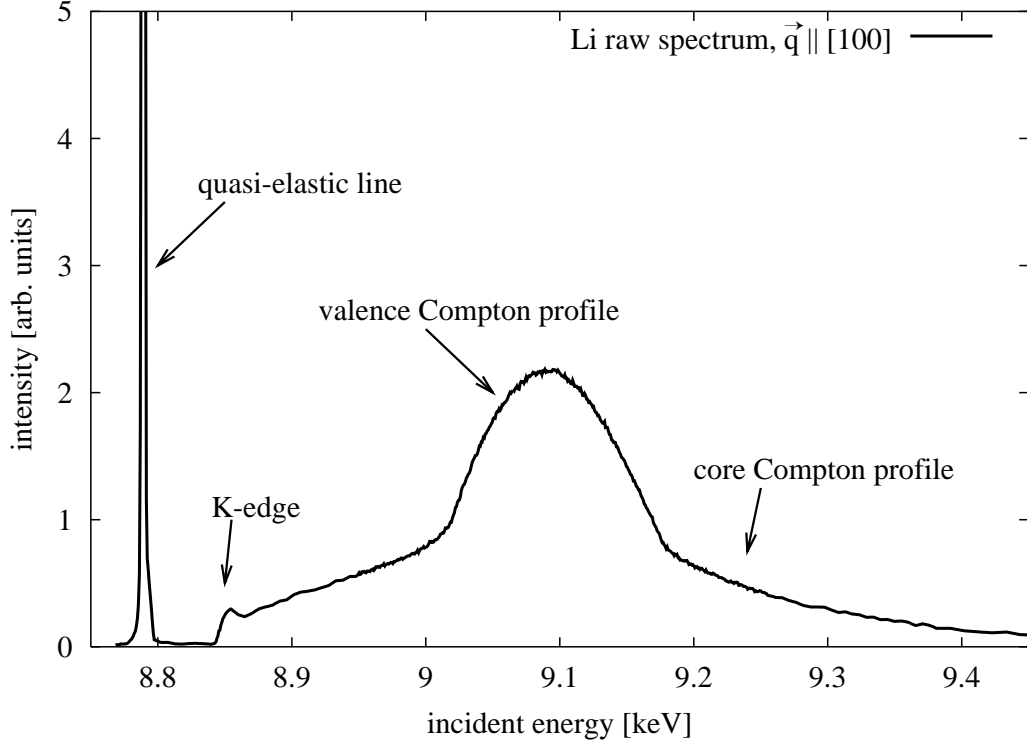


Figure 3.3: Raw spectrum of lithium for $\vec{q} \parallel [100]$ with quasi-elastic line, K-edge, core and valence Compton profile.

3.1.2 Data evaluation

The Compton profiles are evaluated from the sum spectra after calibrating the energy scale considering background subtraction, absorption, the elastic and inelastic scattering detected by the NaI monitor detector, the relativistic correction of the double differential scattering cross section and the subtraction of the multiple scattering contribution. The resulting Compton profiles are normalized utilizing Eq. (1.31). The measured normalized intensity I can be expressed as a function of the incident energy ω_1 via

$$I(\omega_1) = \frac{I_{\text{detector}}(\omega_1)}{I_{\text{monitor}}(\omega_1)} = B + \frac{S(\omega_1)}{M(\omega_1)} C (J(p_z(\omega_1)) + M_S(p_z(\omega_1))) \quad (3.1)$$

B being the scattering background, $M(\omega_1)$ the energy dependent corrections of the monitor signal, $S(\omega_1)$ the energy dependent corrections of the detector signal, and $M_S(p_z(\omega_1))$ the multiple scattering contribution. The constant C contains all factors which are not energy dependent and can be evaluated using the normalization condition.

Energy scale

The K absorption edges of lithium, beryllium and graphite were measured and each energy position is determined by the position of the maximum of the first derivative in the regime of the absorption edge. Then the energy scale is calibrated according to the energy positions of the absorption edges of $E_{\text{KLi}} = 54.7$ eV, $E_{\text{KBe}} = 111.5$ eV and $E_{\text{KC}} = 284.2$ eV [Cardona and Ley 1978] and the error of the energy axis is evaluated to be $\Delta\omega_1^{\text{abs}} \approx 0.5$ eV. After performing the energy dependent corrections, the energy scale can be converted to the momentum scale using Eq. (1.29). Together with the uncertainty of the absolute value of the scattering angle $\Delta\theta^{\text{abs}} \approx 1^\circ$ defined by the spectrometer setup, the position of $p_z = 0$ a.u. is fixed to ± 0.006 a.u. assuming a quadratic error propagation for the two contributions.

Radiation background

The background radiation, determined at the low energy tail of the quasi-elastic line, is assumed to be constant over the whole energy range and found to be of the same value for all measured directions of \vec{q} . This constant radiation background B is subtracted as shown in Eq. (3.1).

Energy dependent corrections of the monitor signal

If inverse geometry is utilized, the monitor signal becomes energy dependent since the incident energy ω_1 is varied. The NaI detector detects the elastic and the inelastic scattered photons from the Kapton scattering foil, where the energy of the scattered photons ω_f is given by ω_1 for elastic scattering and is approximated by $\omega_{\text{max}}^{\text{CP}}$, the energy position of the maximum of the corresponding Compton profile, for inelastic scattering. $\omega_{\text{max}}^{\text{CP}}$ can be calculated utilizing Eq. (1.28) by setting $p_z = 0$ a.u. with the incident energy ω_1 and the scattering angle $\theta_{\text{monitor}} = 90^\circ$. Thus, the energy dependent correction factor of the monitor signal can be expressed as $M(\omega_1) = M^{\text{el}}(\omega_1) + M^{\text{in}}(\omega_1, \omega_{\text{max}}^{\text{CP}})$ performing the correction separately for the elastic $M^{\text{el}}(\omega_1)$ and the inelastic $M^{\text{in}}(\omega_1, \omega_{\text{max}}^{\text{CP}})$ scattering.

The radiation from the Kapton scattering foil passed a Kapton window at the exit of the vacuum tube and a distance in air before it reached the entrance beryllium

window of the NaI detector. The intensity measured by the NaI detector is corrected due to absorption of the Kapton scattering foil $M_{\text{abs}}^{\text{foil}}$, the Kapton window $M_{\text{abs}}^{\text{Kap}}$, the beryllium window $M_{\text{abs}}^{\text{Be}}$ and air $M_{\text{abs}}^{\text{air}}$. Furthermore, the energy dependent scattering intensities for inelastic $I^{\text{in}}(\omega_1)$ and elastic $I^{\text{el}}(\omega_1)$ scattering have to be considered. Thus, the separated total energy dependent correction factors of the monitor signal can be written as

$$M^{\text{el}}(\omega_1) = I^{\text{el}}(\omega_1) M_{\text{abs}}^{\text{foil}}(\omega_1, \omega_1) M_{\text{abs}}^{\text{Kap}}(\omega_1) M_{\text{abs}}^{\text{air}}(\omega_1) M_{\text{abs}}^{\text{Be}}(\omega_1) M_{\text{abs}}^{\text{t}}(\omega_1) \quad (3.2)$$

and

$$M^{\text{in}}(\omega_1, \omega_{\text{max}}^{\text{CP}}) = I^{\text{in}}(\omega_1) M_{\text{abs}}^{\text{foil}}(\omega_1, \omega_{\text{max}}^{\text{CP}}) M_{\text{abs}}^{\text{Kap}}(\omega_{\text{max}}^{\text{CP}}) M_{\text{abs}}^{\text{air}}(\omega_{\text{max}}^{\text{CP}}) \\ \times M_{\text{abs}}^{\text{Be}}(\omega_{\text{max}}^{\text{CP}}) M_{\text{abs}}^{\text{t}}(\omega_1), \quad (3.3)$$

where the absorption of the transmitted beam by the Kapton scattering foil and the Kapton window between the vacuum tube and the scattering chamber is corrected via $M_{\text{abs}}^{\text{t}}(\omega_1)$.

The intensity of the incident beam is attenuated by the absorption of the Kapton scattering foil, which holds as well for the scattered radiation. The correction to this absorption is then given by

$$M_{\text{abs}}^{\text{foil}}(\omega_1, \omega_f) = \frac{1 - e^{-(\mu_{\text{Kap}}(\omega_1) + \mu_{\text{Kap}}(\omega_f))d_{\text{foil}} / \cos \alpha_{\text{foil}}}}{(\mu_{\text{Kap}}(\omega_1) + \mu_{\text{Kap}}(\omega_f)) / \cos \alpha_{\text{foil}}}, \quad (3.4)$$

$d_{\text{foil}} = 0.025$ mm being the thickness of the scattering foil, $\alpha_{\text{foil}} = 45^\circ$ the angle between the direction of the incident beam and the surface normal of the scattering foil and μ_{Kap} the absorption coefficient of Kapton. The directions of the incident and the scattered beam are symmetrical with respect to the surface normal. Furthermore, the beryllium window ($d_{\text{Be}} = 0.3$ mm), the air distance ($d_{\text{air}} = 5$ mm) and the Kapton window ($d_{\text{Kap1}} = 0.1$ mm) cause an absorption of the scattered beam which is considered via

$$\begin{aligned} M_{\text{abs}}^{\text{Be}}(\omega_f) &= e^{-\mu_{\text{Be}}(\omega_f)d_{\text{Be}}} \\ M_{\text{abs}}^{\text{air}}(\omega_f) &= e^{-\mu_{\text{air}}(\omega_f)d_{\text{air}}} \\ M_{\text{abs}}^{\text{Kap}}(\omega_f) &= e^{-\mu_{\text{Kap}}(\omega_f)d_{\text{Kap1}}}. \end{aligned} \quad (3.5)$$

The absorption correction for the transmitted beam is given by

$$M_{\text{abs}}^t(\omega_1) = e^{\mu_{\text{Kap}}(\omega_1)d_{\text{foil}}/\cos\alpha_{\text{foil}}} e^{\mu_{\text{Kap}}(\omega_1)d_{\text{Kap}2}} , \quad (3.6)$$

$d_{\text{Kap}2} = 0.025$ mm is the thickness of the Kapton window between the vacuum tube and the scattering chamber, in which the sample is mounted. All absorption coefficients are calculated using ln-ln mass attenuation coefficients [McMaster et al. 1970].

The energy dependent scattering intensities $I^{\text{el}}(\omega_1)$ and $I^{\text{in}}(\omega_1)$ are calculated utilizing the corresponding elastic and inelastic scattering factors according to Wang et al. [Wang et al. 1993]. Within this calculation the scattering intensity of a free electron for elastic and inelastic scattering is described by the Thomson and the Klein-Nishina scattering cross section, respectively.

Energy dependent corrections of the detector signal

The signal of the Ge detector is corrected due to the sample absorption and due to the relativistic treatment of the double differential scattering cross section by

$$S(\omega_1) = S_{\text{abs}}^{\text{sample}}(\omega_1) S_{\text{rel}}(\omega_1) \quad (3.7)$$

utilizing the absorption correction

$$S_{\text{abs}}^{\text{sample}}(\omega_1) = \frac{1 - e^{-(\mu_{\text{Li}}(\omega_1) + \mu_{\text{Li}}(\omega_2))d_{\text{Li}}/\cos\alpha_{\text{Li}}}}{(\mu_{\text{Li}}(\omega_1) + \mu_{\text{Li}}(\omega_2))/\cos\alpha_{\text{Li}}} \quad (3.8)$$

for fixed analyzer energy ω_2 . $d_{\text{Li}} = 6.5$ mm denotes the sample thickness and $\alpha_{\text{Li}} = 8^\circ$. The relativistic correction of the Compton scattering cross section discussed in section 1.3.2 is considered to be as follows

$$S_{\text{rel}}(\omega_1) = \frac{r_0^2}{2} \frac{\omega_2}{\omega_1} \left(\frac{R}{R'} + \frac{R'}{R} - 2 \sin^2 \theta \cos^2 \beta \right) , \quad (3.9)$$

where the incident beam is linear polarized in the scattering plane so that $\beta = 0$.

Fig. 3.4 shows the total correction factor of the NaI signal along with the relativistic scattering cross section correction and the sample absorption. After performing the energy dependent corrections, the energy scale is converted to momentum scale utilizing Eq. (1.29).

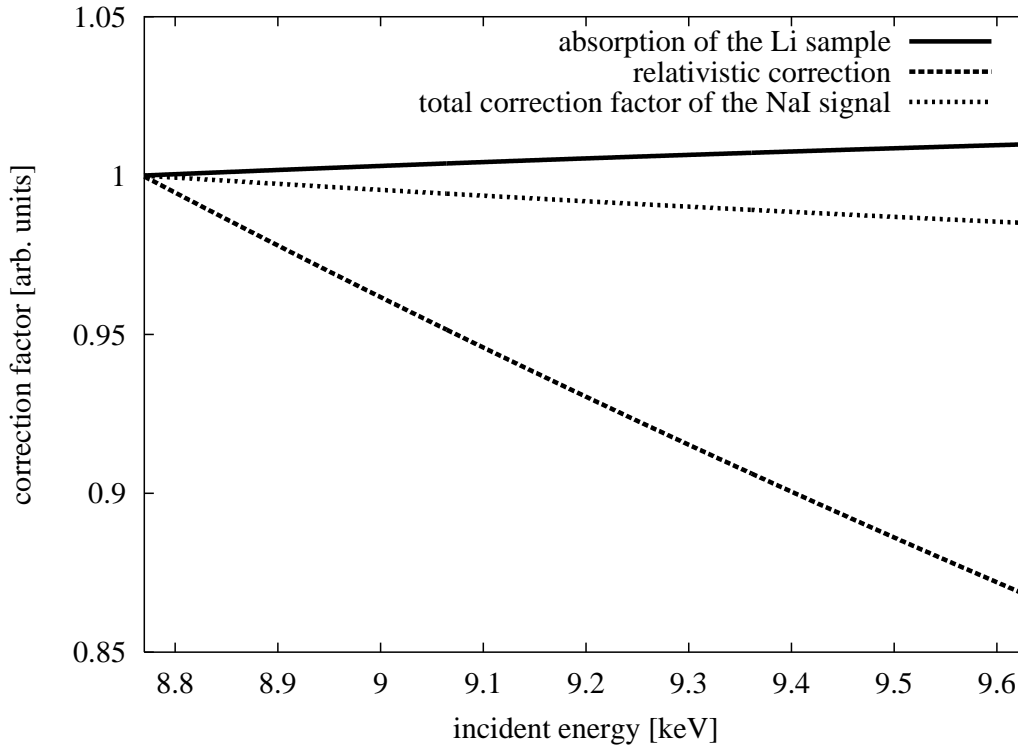


Figure 3.4: Energy dependent correction factors for the measured lithium spectra. The first value of each correction factor is normalized to one what enables the comparability of the different contributions.

Multiple scattering

In the course of the scattering process a finite probability is given for multiple scattering within the sample. The multiple scattering contribution to the measured spectra is modeled utilizing a Monte Carlo code [Felsteiner and Schülke 1997] which simulates the scattering of the photons within the sample considering sample geometry, scattering angle, incident energy and polarization of the radiation. To account for inelastic scattering processes the simulation is performed on the basis of the experimentally obtained Compton profiles neglecting the multiple scattering contribution. $2 \cdot 10^7$ photons are simulated for each calculated multiple scattering spectrum. Since the code cannot be applied to experimental setups accomplishing inverse geometry, the distribution of the multiple scattered photons as a function of the analyzed energy is determined for 10 incident energies ranging from 8.8 keV to 9.4 keV. This is done for all measured directions of \vec{q} considering the corresponding sample geometry. The multiple scattering spectra show a slight asymmetry (see Fig. 3.5) but exhibit neither a significant dependence on the incident energy nor on the direction of the scattering vector. Thus, the average over all calculated

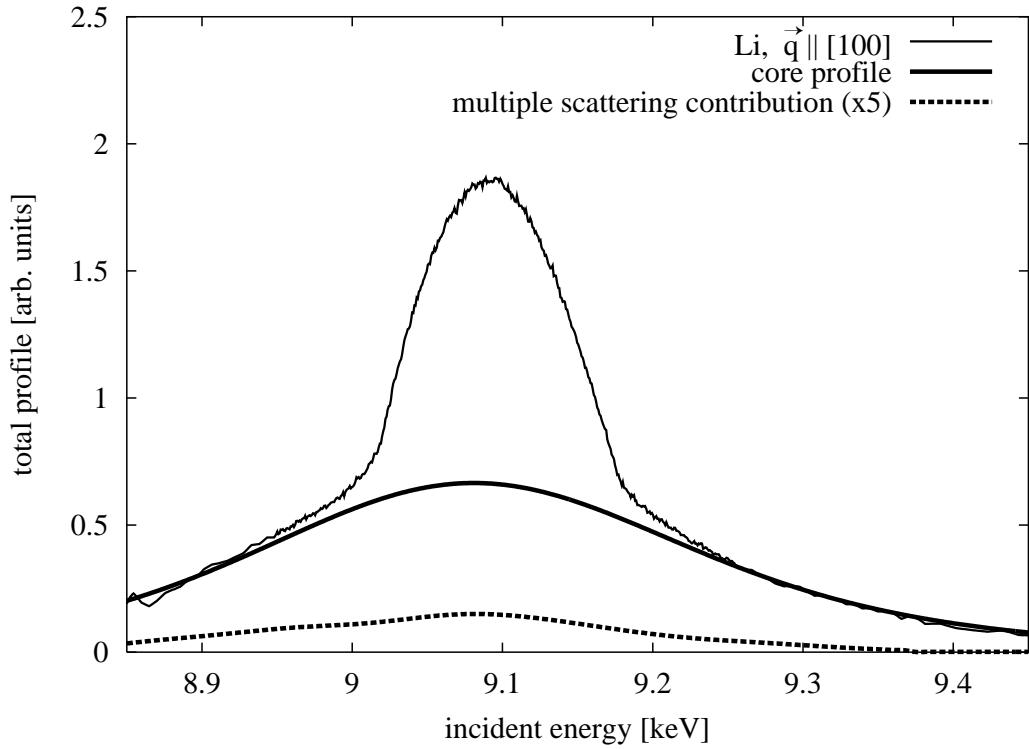


Figure 3.5: Total profile after energy dependent corrections for $\vec{q} \parallel [100]$ plotted as thin solid line together with the calculated asymmetrical core electron Compton profile (bold solid line) and the multiple scattering contribution (dashed line), enhanced by a factor of 5.

multiple scattering distributions is assumed to be a good approximation to correct the experimental spectra for multiple scattering. The integral intensity of the total multiple scattering contribution is calculated to be roughly 2.3% of the total intensity where the triple scattering accounts only for 0.06% of the total intensity. The multiple scattering contribution $M_S(p_z(\omega_1))$, presented in Fig. 3.5 as a dashed line, is subtracted from the total profile following Eq. (3.1).

Core Compton profile

The total Compton profile of lithium consists of the 1s core electron and the valence electron contribution. The valence electron Compton profile can be extracted utilizing core electron profiles, which can properly be calculated using Hartree-Fock wave functions provided the impulse approximation is valid [Biggs et al. 1975]. However, deviations from the impulse approximation resulting in an asymmetry of the core Compton profile have been found by several exper-

iments [Holt et al. 1979, Wong et al. 1982]. On the theoretical side the asymmetrical 1s core electron contribution of graphite was calculated for 12.8 keV incident energy and 135° scattering angle utilizing the hydrogenic approximation [Issolah et al. 1988] and a first correction to the non-relativistic Compton scattering cross section in the impulse approximation was discussed by Holm and Ribberfors [Holm and Ribberfors 1989] explaining the asymmetry of the core Compton profile for aluminium [Holt et al. 1979]. Their calculation scheme is applied to correct the symmetric Hartree-Fock core Compton profile of lithium obtaining an asymmetrical 1s core electron Compton profile which is plotted in Fig. 3.5 as a bold line compared to the total profile and to the multiple scattering contribution. The calculated core electron Compton profile fits the total profile at high incident energies between 9.25 keV and 9.45 keV, where the contribution of the valence electron Compton profile is negligible. However, in the regime of the lithium K-edge between 8.85 keV and 8.90 keV the core profile deviates from the total Compton profile due to the strong influence of the absorption edge. The subtraction of the core electron contribution and their influence on the interpretation of the valence electron Compton profile of lithium will be discussed in detail later.

Normalization

The Compton profiles are obtained on absolute scale utilizing the normalization condition of Eq. (1.31). To calculate the normalization constant C , Eq. (3.1) is integrated as follows

$$C = \frac{\int_{-p_v}^{p_v} dp_z \frac{M(\omega_1)}{S(\omega_1)} (I(\omega_1) - B)}{\left(N_{\text{val}} + \int_{-p_v}^{p_v} dp_z (J_{\text{core}}(p_z(\omega_1)) + M_S(p_z(\omega_1))) \right)}, \quad (3.10)$$

where the total Compton profile $J(p_z)$ is separated into the valence electron contribution $J_{\text{val}}(p_z)$ and the core electron Compton profile $J_{\text{core}}(p_z)$. As long as the valence Compton profile contributes to the total profile only within the integration range from $-p_v$ to p_v , the normalization condition of Eq. (1.31) can be applied. N_{val} , the number of valence electrons, equals one in the case of lithium.

Momentum space resolution

The momentum space resolution Δp_z is determined by the energy resolution of the spectrometer $\Delta\omega$ and the full width of half maximum (FWHM) of the certain

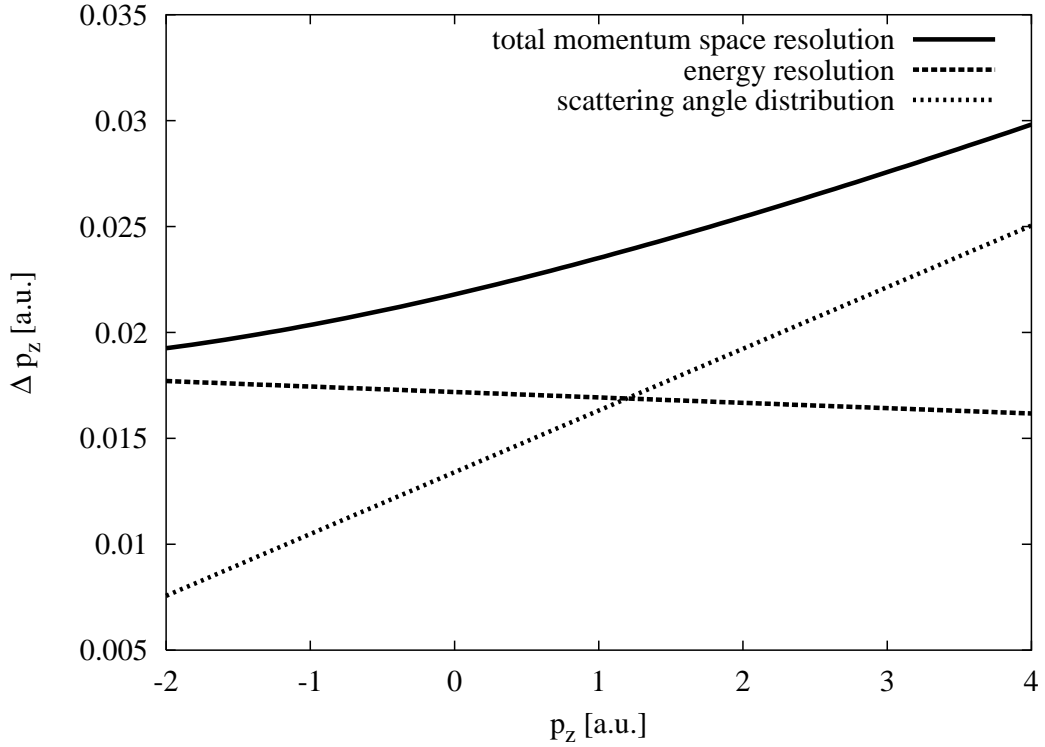


Figure 3.6: Contribution of the energy resolution $\Delta\omega$ and of the distribution of scattering angles $\Delta\theta$ to the total momentum space resolution Δp_z as a function of p_z .

distribution of scattering angles $\Delta\theta$ accepted by the analyzer crystal. This distribution is determined by the diameter of the analyzer crystal of 40 mm and the distance between analyzer and sample of 860 mm. The FWHM of the distribution is then given by $\Delta\theta = 2.31^\circ$. The energy resolution is $\Delta\omega = 2.3$ eV estimated by the FWHM of the quasi-elastic line. Thus, the total momentum space resolution is obtained using Eq. (1.29) to

$$\Delta p_z = \sqrt{\left(\frac{\partial p_z}{\partial \theta}\right)^2 \Delta\theta^2 + \left(\frac{\partial p_z}{\partial \omega_1}\right)^2 \Delta\omega^2}. \quad (3.11)$$

The resolution function slightly varies as a function of p_z and is shown in Fig. 3.6. If the experimentally obtained Compton profiles are compared to theory, the resolution function of the experiment is considered by convoluting the calculated Compton profiles with a Gaussian resolution function. The FWHM of this Gaussian is assumed to be constant, namely $\Delta p_z = 0.022$ a.u., corresponding to the total momentum space resolution at the Compton profile maximum.

3.2 Experimental results

The experimentally obtained Compton profiles of lithium for $\vec{q} \parallel [100], [110], [111]$ and $[311]$ are presented in Figs. 3.7 and 3.8. The total Compton profile, which consist of the core and the valence electron Compton profile, is normalized to the number of electrons and thus presented on an absolute scale. The relative statistical error at the maximum of the total Compton profile is about 0.7%. The experimental results are compared to a calculation of the valence electron Compton profiles performed by Bansil and Kaprzyk [Sakurai et al. 1995] utilizing a self-consistent KKR (Korringa-Kohn-Rostocker) bandstructure scheme within the LDA, which includes the Lam-Platzman correction to electron-electron correlation [Lam and Platzman 1974]. The core electron contribution is calculated using the first correction to the non-relativistic Compton scattering cross section as discussed in section 3.1.2 and is added to the LDA valence profiles. Finally, the computed total Compton profiles are convoluted with the momentum space resolution function of the experiment.

The experimentally observed Compton profiles exhibit a clear asymmetry with respect to $p_z = 0$ a.u. and the maxima of the valence Compton profiles, obtained after subtraction of the asymmetrical core contribution, are shifted to negative p_z values which are given in Tab. 3.1. The p_z position of the valence Compton profile maximum is determined by the maximum of a parabola fitted to the experimentally obtained valence Compton profiles within the range between -0.3 a.u. and 0.3 a.u. The averaged position of the valence Compton profile maximum is $p_z^{\text{CPmax}} = -0.031 \pm 0.004$ a.u. It can be ruled out that this asymmetry is due to the uncertainty of the p_z scale since $p_z = 0$ a.u. could be fixed to ± 0.006 a.u. Furthermore, the Fermi breaks are significantly broadened beyond the experimental resolution compared to the LDA calculations for all measured directions of \vec{q} . No sharp Fermi break can be resolved.

This is stressed even more by concerning the second derivatives of the valence Compton profiles, since the width and the amplitude of the second derivative gives an estimate for the smearing of the Fermi break. The positions, the width and the amplitudes of the second derivative at the Fermi breaks for positive and negative p_z are determined by fitting the second derivative utilizing the following model function $F(p_z)$

$$F(p_z) = a_1 \exp\left(-4 \ln(2) \left(\frac{p_z - p_1}{f}\right)^2\right) + a_2 \exp\left(-4 \ln(2) \left(\frac{p_z - p_2}{f}\right)^2\right) + a_3 \left(\operatorname{arccot}\left(\frac{b}{p_1 - p_z}\right) + \operatorname{arccot}\left(\frac{b}{p_2 - p_z}\right)\right). \quad (3.12)$$

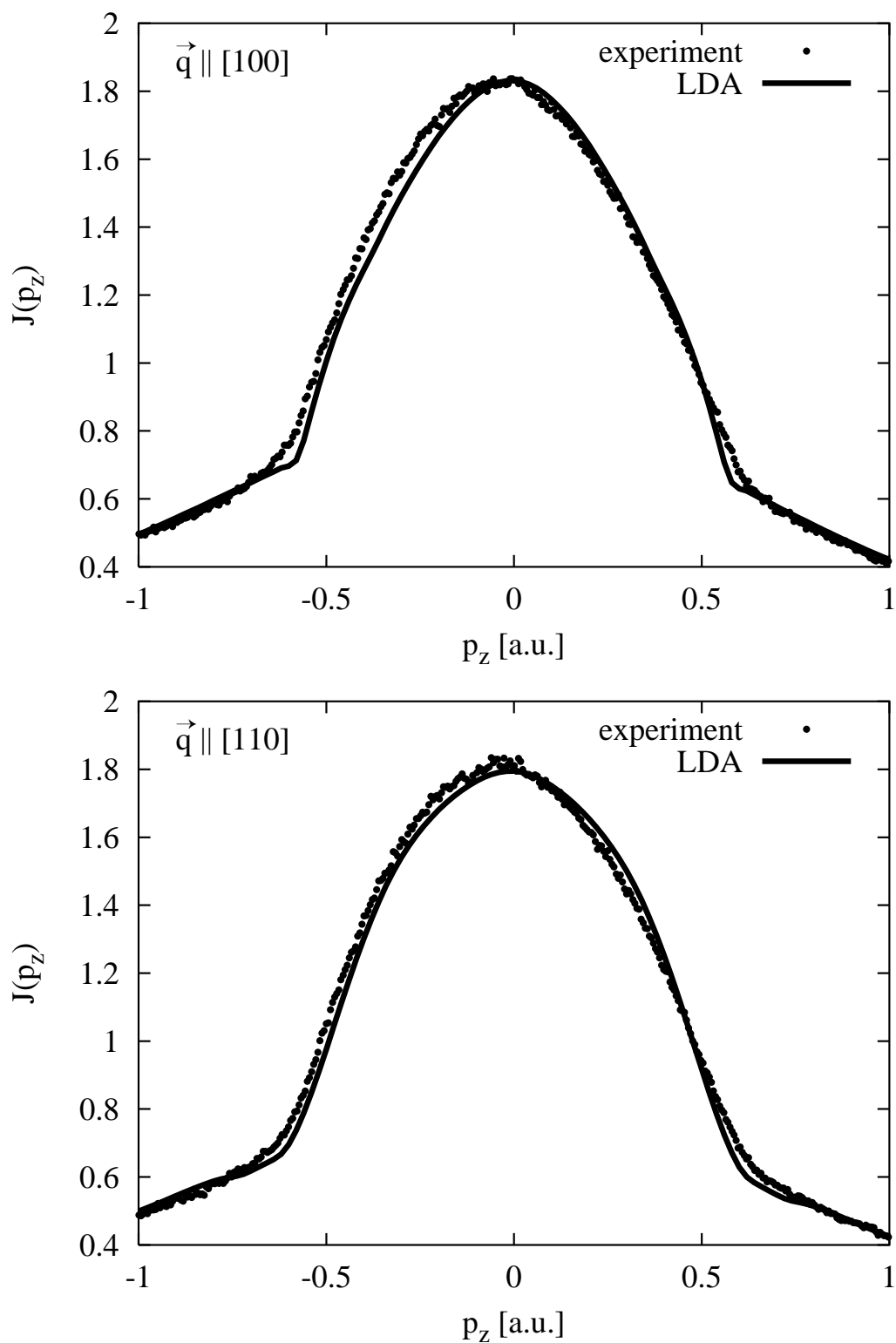


Figure 3.7: Experimental lithium Compton profile for $\vec{q} \parallel [100]$ and $[110]$ compared to LDA theory

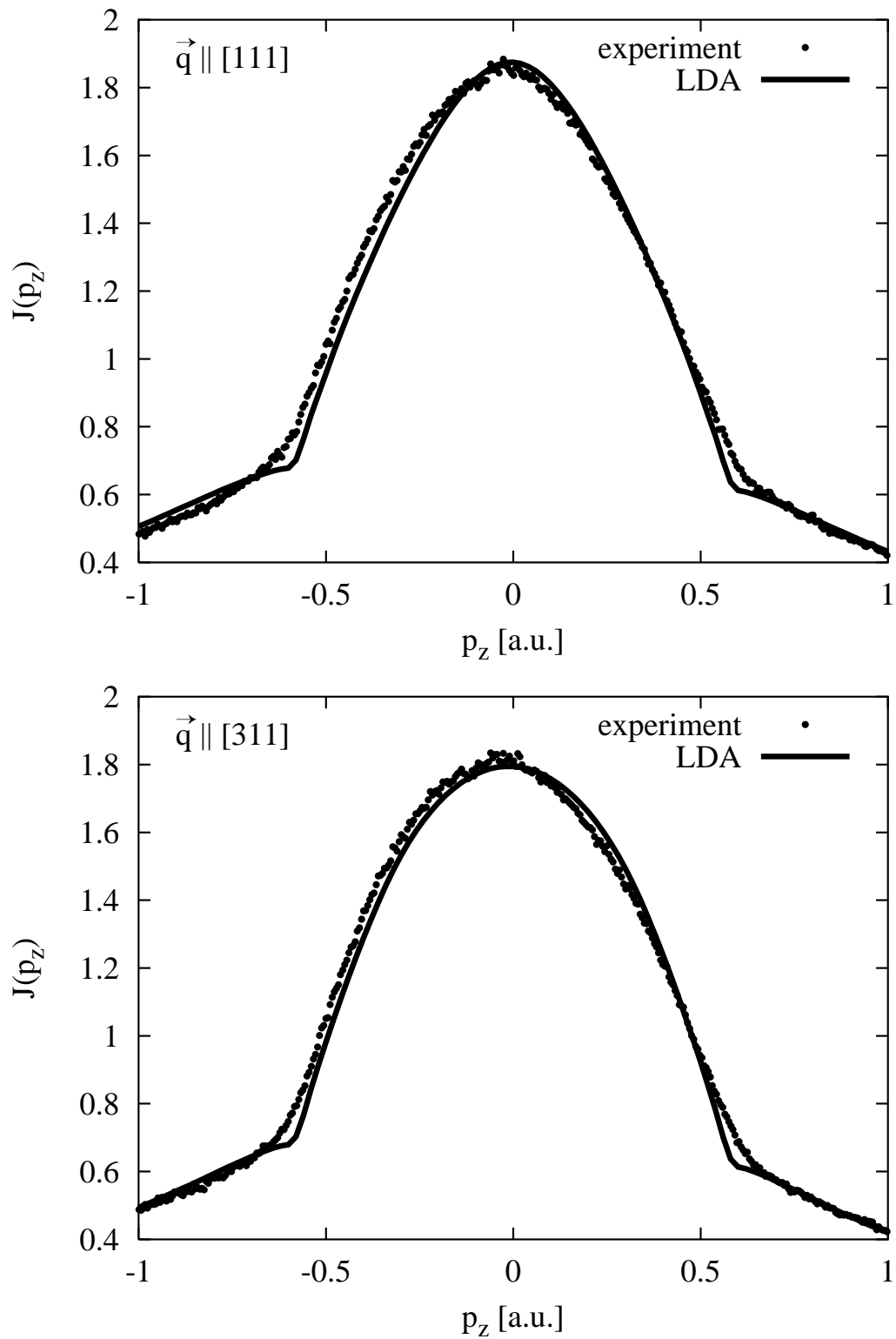


Figure 3.8: Experimental lithium Compton profile for $\vec{q} \parallel [111]$ and $[311]$ compared to LDA theory.

The positions p_1, p_2 and the amplitudes a_1, a_2 of the Gaussians are fitted independently and the FWHM f is chosen to be identical for both Gaussians since the variation of the momentum space resolution of 0.002 a.u. in the regime of the valence Compton profile is negligible. The arccot function accounts for the negative contribution to the second derivative for $|p_z| < 0.5$ a.u. and its amplitude is fitted by varying the parameter b . Due to the statistical error of the experimental data, both the theoretically and the experimentally obtained Compton profiles have to be convoluted by a Gaussian before calculating the second derivatives. The lowest additional convolution for which the fit procedure yields reasonable results is $f_a = 0.12$ a.u. The second derivatives are analyzed with respect to differences between experiment and theory appearing in spite of this additional convolution. For larger additional convolutions f_a the information obtained from the experimental spectra is reduced, whereas for smaller additional convolutions the results are more and more affected by the statistical error of the experiment. If $f_a < 0.07$ a.u. the fit procedure fails. The error in analyzing the second derivatives is estimated by applying the fit procedure to the experimental Compton profiles utilizing various additional convolutions between 0.07 a.u. and 0.17 a.u.

The symmetrized second derivatives of the valence Compton profiles compared to the corresponding LDA results are shown in Fig. 3.9, where the derivatives are calculated at $f_a = 0.12$ a.u. extra convolution. The results for $F(p_z)$ are symmetrized and plotted as a thin solid line in Fig. 3.9 exhibiting a good agreement with the experimental results. In contradiction to the predictions of LDA theory the second derivatives of the experimentally obtained Compton profiles are significantly smaller in amplitude and show a larger FWHM around p_F .

$\vec{q} \parallel$	[100]	[110]	[111]	[311]
p_z^{CPmax} [a.u.]	-0.030	-0.031	-0.021	-0.041
$p_F^+ + p_F^-$ [a.u.]	0.007	-0.002	-0.004	0.002

Table 3.1: Position of the valence Compton profile maximum p_z^{CPmax} and the difference of the Fermi break positions $p_F^+ + p_F^-$ determined from the experiment.

The positions of the Fermi break determined via the model function $F(p_z)$ are found to be symmetric with respect to $p_z = 0$ a.u. within experimental error. Tab. 3.1 shows the shift of the position of the Fermi breaks $p_F^+ + p_F^-$ ¹ obtained by fitting the model function to the second derivatives and its error is estimated to be ± 0.01 a.u. as described above.

The asymmetry of the Compton profiles and its additional broadening is discussed in detail and interpreted in terms of final state effects in what follows.

¹ p_F^+ and p_F^- corresponds to positive p_z and to negative p_z , respectively.

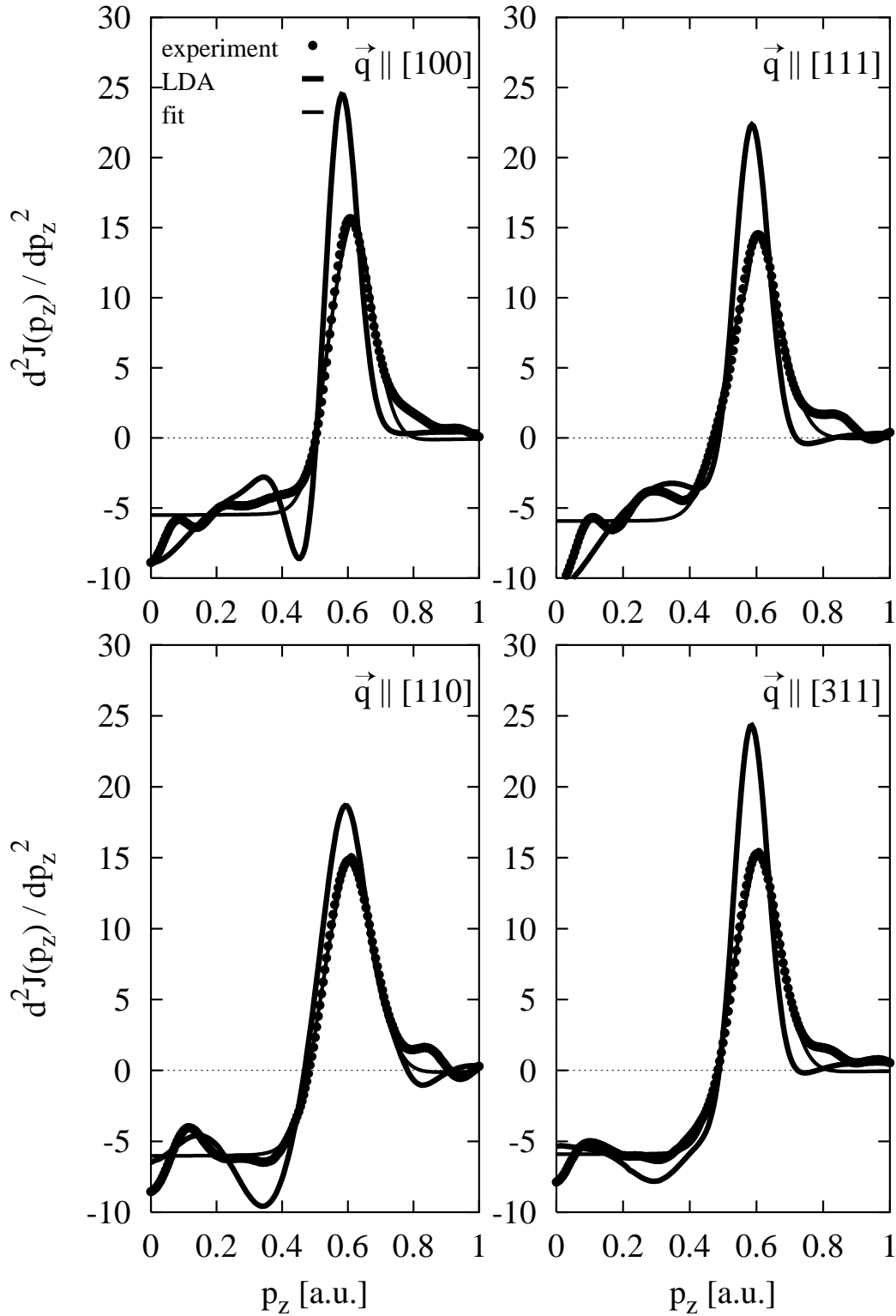


Figure 3.9: Second derivatives of the experimentally observed lithium Compton profiles for $\vec{q} \parallel [100]$, $[110]$, $[111]$ and $[311]$ (dots) compared to LDA theory (bold line). The second derivatives are calculated at $f_a = 0.12$ a.u. extra convolution and the thin solid line represents the result obtained for the model function $F(p_z)$.

3.3 Valence Compton profile asymmetry

The asymmetry of the total Compton profile is calculated by the difference $J(p_z) - J(-p_z)$ and represented in Fig. 3.10 (upper panel) for all measured directions of \vec{q} . For clarity only each fourth experimental datapoint is plotted and the experimental error is presented exemplarily in the case of the [110] asymmetry. The asymmetries exhibit no significant \vec{q} dependence. Thus, the average over all directions is calculated and shown in Fig. 3.10 (lower panel). Its error is given by the standard deviation of the several asymmetries from the average and is in the order of the experimental error of the asymmetry for one single direction.

The total asymmetry can be separated into two different regimes: (i) For $|p_z| > p_F$ ($= 0.589$ a.u. for jellium) the core asymmetry dominates. The experimentally obtained asymmetry of the core electron Compton profile is in good agreement with the predictions of Holm and Ribberfors [Holm and Ribberfors 1989] even though its shape is affected by the lithium K-edge for $|p_z| > 1.4$ a.u. The asymmetry of the calculated core Compton profile is plotted as a solid line in Fig. 3.10 (lower panel). Nevertheless, the amplitude of the core asymmetry is dependent on the asymmetry of the multiple scattering contribution and is also sensitive to small changes of the energy dependent correction factors. Therefore, the comparison between the measured asymmetry of the core Compton profile and the theoretical predictions should be considered with care. (ii) For $|p_z| < p_F$ the shape of the total asymmetry changes rapidly with p_z due to the asymmetry of the valence Compton profile. To extract this contribution from the total asymmetry, the calculated asymmetry of the core Compton profile is subtracted. The result, shown in Fig. 3.11, is hardly influenced by small changes of the energy dependent correction factors and is well separated from the widespread asymmetries of the core Compton profile and the multiple scattering contribution.

Different theoretical approaches within the impulse approximation, e.g. LDA [Sakurai et al. 1995] or QMC [Filippi and Ceperley 1999], failed to overcome the discrepancies between experiment and theory in the case of the valence Compton profile of lithium. Thus, in this study the jellium model is chosen to go beyond the impulse approximation to interpret the experimental results presented so far. It is stated that this choice is justified since no significant \vec{q} dependence of the asymmetry is found. In terms of the jellium model the interpretation of the impulse approximation is, to neglect all final state effects, namely the interaction of the excited particle with the many-particle system and the interaction of the particle with the hole left behind. These two effects are theoretically described by the self-energy correction and the vertex correction to the free-particle polarizability $\chi_{sc}^0(\vec{q}, \omega)$. Within the range of energy and momentum transfer of the experiment the polarization function $\chi(\vec{q}, \omega)$, which is directly related to the dynamic structure factor $S(\vec{q}, \omega)$, can be replaced by the proper polarization function $\chi_{sc}(\vec{q}, \omega)$.

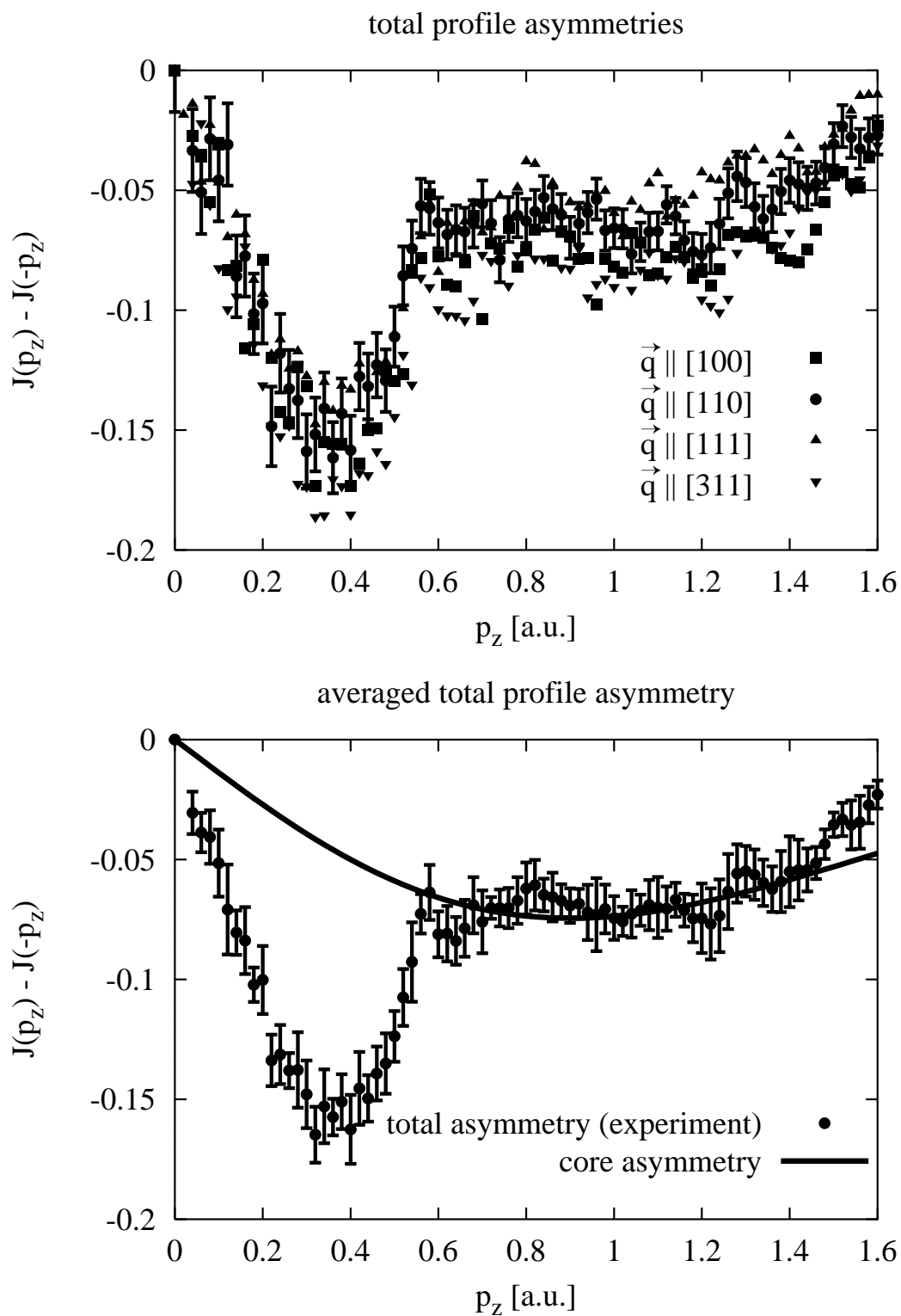


Figure 3.10: Total Compton profile asymmetry of lithium for $\vec{q} \parallel [100]$, $[110]$, $[111]$ and $[311]$ (upper panel) and the directional average of the asymmetry compared to the calculated asymmetry of the core Compton profile (lower panel).

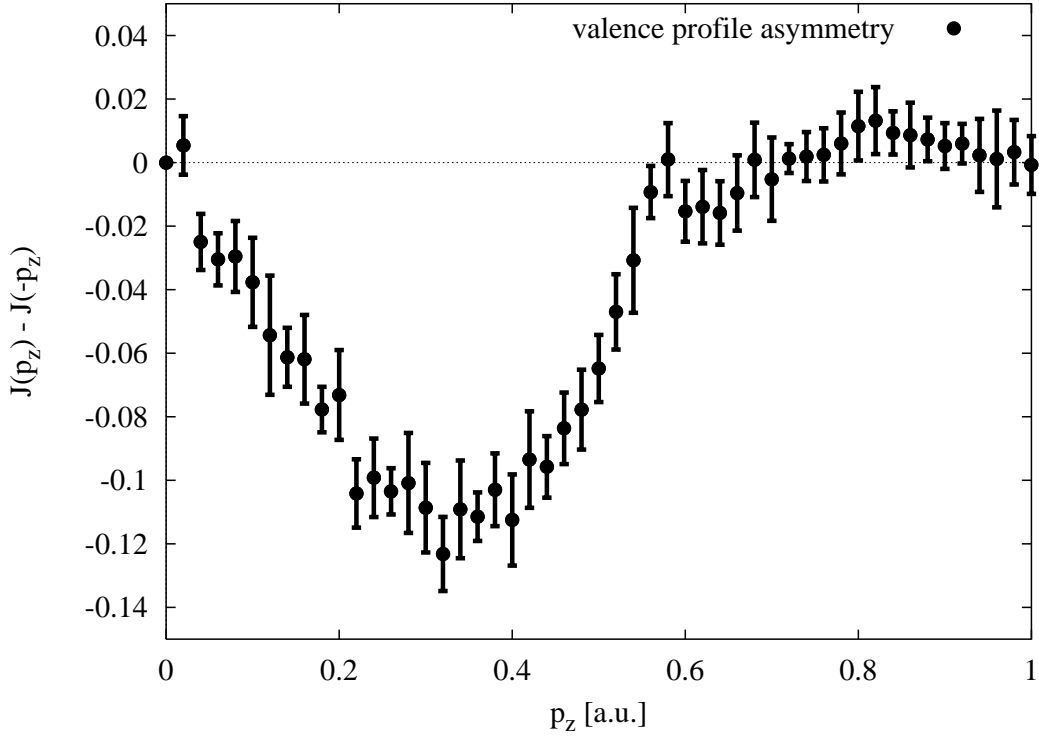


Figure 3.11: Valence Compton profile asymmetry of lithium.

3.3.1 Self-energy correction

The self-energy $\Sigma(\vec{p}, E)$ is calculated according to Hedin [Hedin 1965] within the standard GW approximation and by screening the bare Coulomb potential dynamically with the RPA dielectric function, see Eq. (2.14). Within this calculation the self-energy is separated into its particular components to overcome integration problems. Then the spectral density function $A(\vec{p}, E)$ is determined utilizing Eq. (2.18). The self-energy correction of the proper polarization $\chi_{sc}^{SE}(\vec{q}, \omega)$ up to all orders in the screened Coulomb potential is represented by Eq. (2.20) and thus, the dynamic structure factor $S(\vec{q}, \omega)$ reads as

$$S(\vec{q}, \omega) = \frac{1}{\pi} \int \frac{d\vec{p}}{(2\pi)^3} \int_{E_F - \omega}^{E_F} \frac{dE}{(2\pi)} A(\vec{p}, E) A(\vec{p} + \vec{q}, E + \omega - \omega_s) \quad (3.13)$$

utilizing a slightly modified expression compared to Eq. (2.21) by introducing ω_s . The adjustable parameter ω_s takes approximately into account the deviations of the excitation energies from the jellium model which are induced by the lattice potential [Borstel 1985]. This parameter is estimated to be $\omega_s = -3.5$ eV by

fitting the energy positions of the Fermi breaks of the calculated dynamic structure factor to the experimentally obtained peak positions of the second derivatives at p_F , which are symmetrical with respect to $p_z = 0$ a.u. The calculated asymmetry $S(p_z) - S(-p_z)$ is presented in Fig. 3.12 compared with the asymmetry of the valence Compton profile of the experiment.

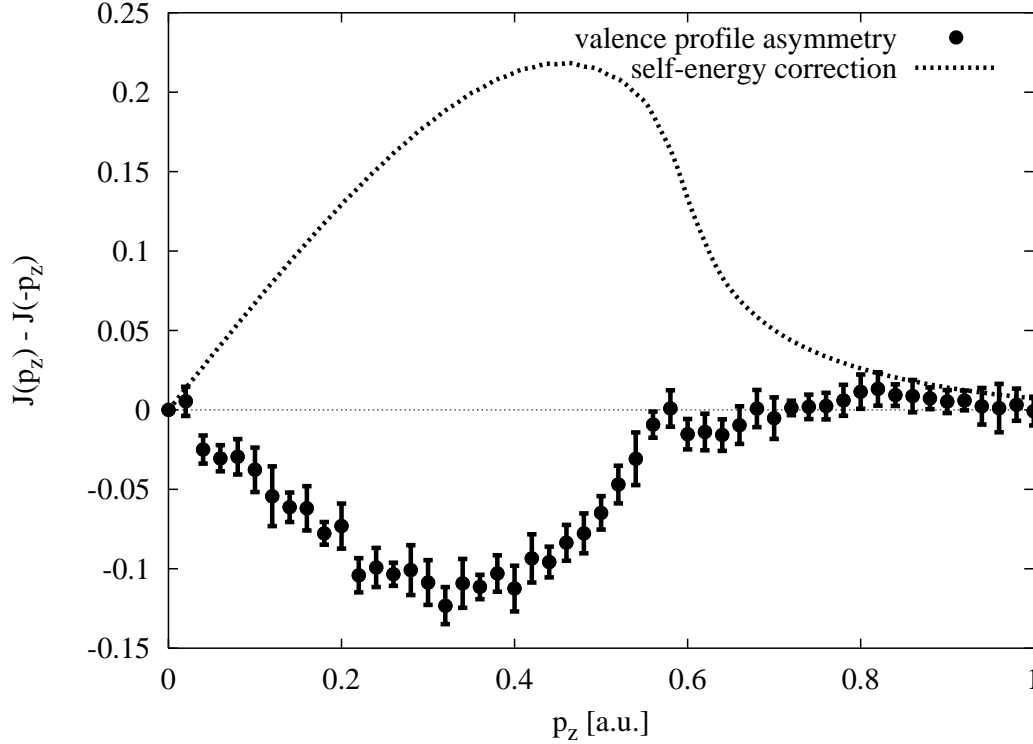


Figure 3.12: Lithium valence Compton profile asymmetry obtained from the experiment compared to the calculated asymmetry taking into account the full self-energy correction (short dashed line).

The fully self-energy corrected proper polarization function yields an asymmetry which is different from the asymmetry of the experiment in sign and in amplitude. A similar disagreement is found within a jellium calculation of the dynamic structure factor of aluminium taking into account the full self-energy correction [Ng and Dabrowski 1986]. The measurement of the dynamic structure factor of aluminium shows that even in the liquid phase the shape of the experimental result disagrees with the calculation a fact which is assigned to the cancellation of the self-energy correction by the vertex correction [Sternemann et al. 1998]. Thus, it is necessary to account for the vertex correction within the calculation of the fully self-energy corrected proper polarization function.

3.3.2 Vertex correction

The particle-hole vertex correction in first order to the fully self-energy corrected proper polarization function $\chi_{sc}^{SE}(\vec{q}, \omega)$ is calculated utilizing Eq. (2.33) according to diagram (b) of Fig. 2.3. The corresponding asymmetry is shown in Fig. 3.13 and compared to the experimental findings. The vertex correction to the fully self-energy corrected proper polarization function changes the sign and the amplitude of the asymmetry. A good qualitative agreement between theory and experiment is obtained. This agreement is slightly improved, if the vertex correction in second order according to Eq. (2.34) by calculating diagram (c) of Fig. 2.3 is added (see Fig. 3.13). It has to be stressed that there exist diagrams of second order in the dynamically screened Coulomb interaction, which are neglected within the presented calculation. Due to this fact only an estimate of the magnitude of the second order corrections is given. The vertex corrections in third order will contribute to the asymmetry by less than the experimental error.

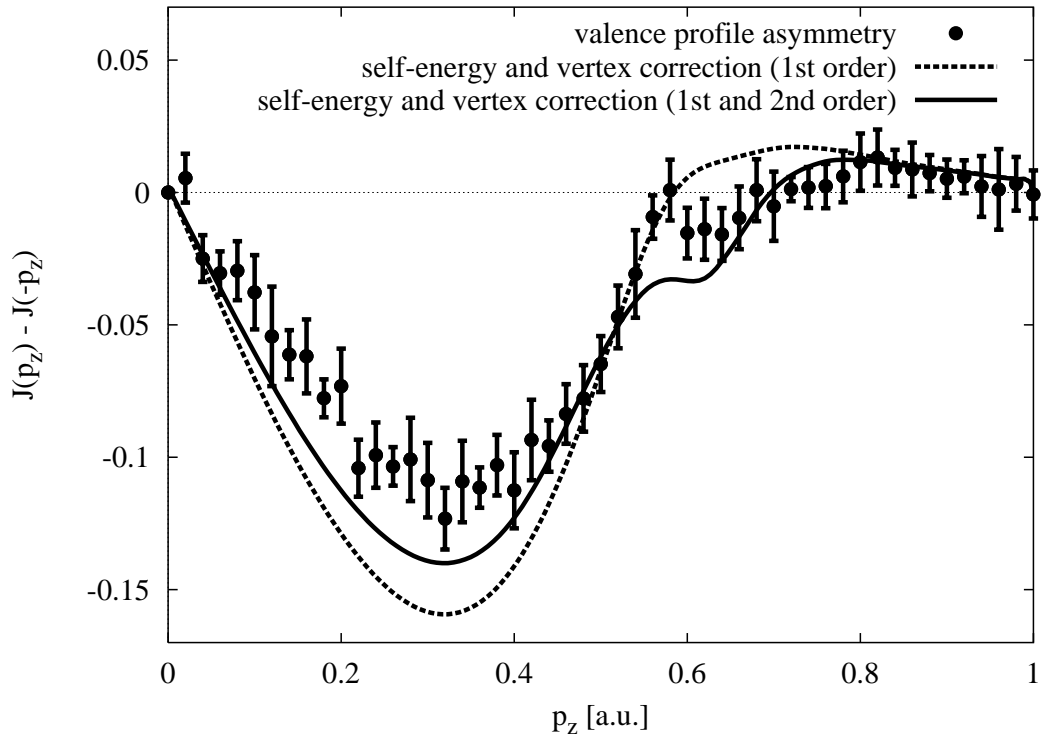


Figure 3.13: Lithium valence Compton profile asymmetry obtained from the experiment compared to the calculated asymmetry taking into account the full self-energy correction and in addition the first order (dashed line) and the first together with the second order vertex correction (solid line).

To summarize, the asymmetry of the valence Compton profile is attributed to an incomplete cancellation of the vertex correction and the self-energy correction. A significant deviation from the impulse approximation for the valence electron Compton profiles is found in the sense, that final state effects have to be considered to explain the asymmetry, which is a direct evidence of the electron-hole interaction in the course of the Compton scattering process.

3.4 Influence of the spectral density function of the particle on the valence Compton profile

The effect of the finite lifetime of the excited particle on the dynamic structure factor in the Compton scattering limit consists in a convolution of the fully correlated electron momentum density $\gamma(\vec{p}|\vec{p})$ with the spectral density function of the excited particle $A_{\text{IA}}(\vec{p} + \vec{q}, \epsilon_{\vec{p}} + \omega)$, which can be written according to Eq. (2.26) as

$$A_{\text{IA}}\left(\vec{p} + \vec{q}, \frac{p^2}{2m} + \omega\right) = \frac{-2 \text{Im} \Sigma\left(\vec{p} + \vec{q}, \frac{p^2}{2m} + \omega\right)}{\left(\omega - \frac{\vec{p} \cdot \vec{q}}{m} - \frac{q^2}{2m}\right)^2 + \left(\text{Im} \Sigma\left(\vec{p} + \vec{q}, \frac{p^2}{2m} + \omega\right)\right)^2}. \quad (3.14)$$

This function is presented in Fig. 3.14 calculated for three different momentum transfers $|\vec{p} + \vec{q}|$.²

The shape and the amplitude of the particle spectral density function varies hardly within the considered range of momentum transfer. Thus, $A_{\text{IA}}(\vec{p} + \vec{q}, p^2/2m + \omega)$ can be approximated in shape and in amplitude by the spectral density function of the excited particle for $|\vec{q}| = 4.83$ a.u. corresponding to the Compton profile maximum. This means, that in Eq. (2.28) $A_{\text{IA}}(\vec{p} + \vec{q}, p^2/2m + \omega)$ can be substituted by $A_{\text{CP}_{\text{max}}}(\omega - \vec{p} \cdot \vec{q}/m - q^2/2m)$, which is the spectral density function of the excited particle calculated corresponding to the maximum of the Compton profile but centered at the energy position $\omega = \vec{p} \cdot \vec{q}/m + q^2/2m$. If \vec{q} points into z -direction, it follows

$$S_{\text{CP}}^{\text{SE}}(\vec{q}, \omega) = \frac{1}{2\pi} \int d\vec{p} \gamma(\vec{p}|\vec{p}) A_{\text{CP}_{\text{max}}}\left(\omega - \frac{p_z q}{m} - \frac{q^2}{2m}\right). \quad (3.15)$$

Performing the p_x and the p_y integration yields

$$S_{\text{CP}}^{\text{SE}}(\vec{q}, \omega) = \frac{1}{2\pi} \int dp_z J(p_z) A_{\text{CP}_{\text{max}}}\left(\omega - \frac{p_z q}{m} - \frac{q^2}{2m}\right). \quad (3.16)$$

Finally, $\tilde{\omega} = p_z q/m + q^2/2m$ is substituted and the valence Compton profile on the energy scale $\tilde{J}(\tilde{\omega}) = J(p_z = \tilde{\omega} m/q - q/2)$ is introduced, ending up with

²The spectral density functions of the particle centered at the energy positions $\omega = \vec{p} \cdot \vec{q}/m + q^2/2m$ are shifted to $\omega = 0$ eV and $\vec{p} = \vec{0}$ a.u.

$$S_{\text{CP}}^{\text{SE}}(\vec{q}, \omega) = \frac{m}{q} \int \frac{d\tilde{\omega}}{2\pi} \tilde{J}(\tilde{\omega}) A_{\text{CP}_{\text{max}}}(\omega - \tilde{\omega}) . \quad (3.17)$$

Within this approximation the finite lifetime of the final state due to the imaginary part of its self-energy affects the fully correlated valence Compton profile by a convolution with the spectral density function of the excited particle on the energy scale, resulting in an additional broadening of the valence Compton profile.

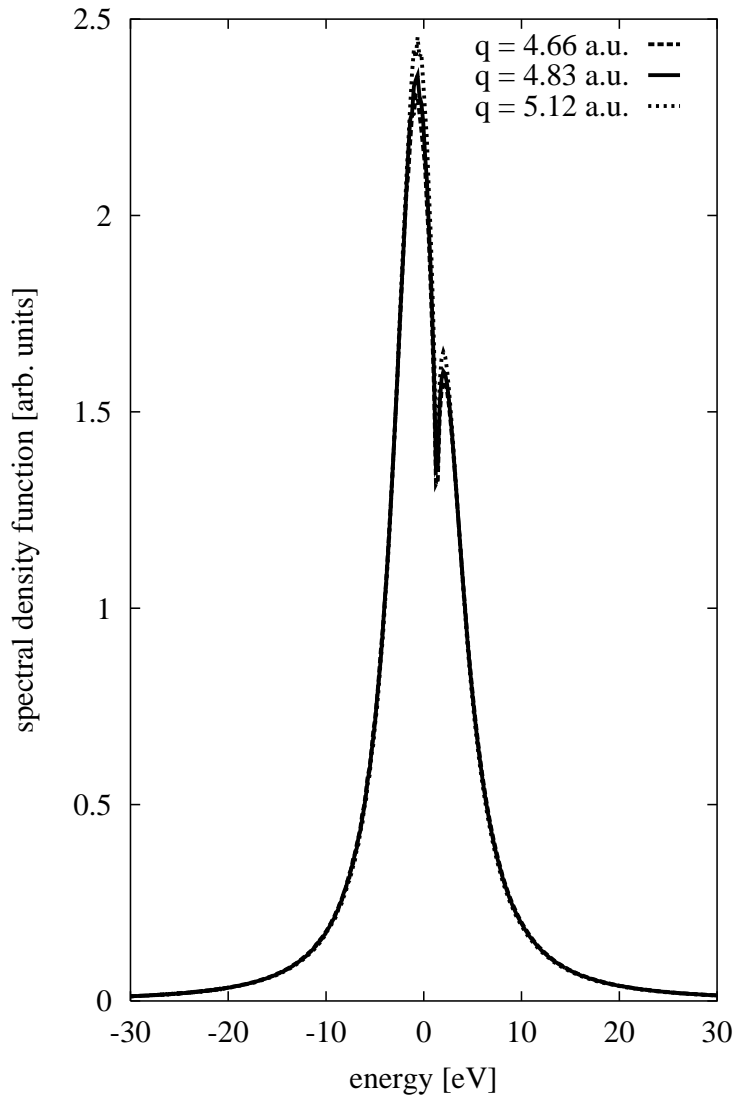


Figure 3.14: Spectral density function of the excited particle for different $|\vec{q}|$.

In Fig. 3.15 the measured total Compton profiles are plotted in the range from 0.5 a.u. to 0.7 a.u. around the Fermi momentum and compared to the LDA Compton profiles with and without convolution with the spectral density function of the excited particle, where the asymmetrical core Compton profile is added to the LDA valence Compton profiles.

Taking into account the final state interaction given by the convolution of Eq. (3.17) results in a clear broadening of the Fermi break, which improves the agreement between experiment and theory. To quantify this broadening it is most suitable to investigate the second derivatives of the Compton profiles around p_F .

Since the second derivatives of the experimentally observed valence Compton profiles at the Fermi break are found to be symmetric with respect to $p_z = 0$ a.u., the symmetrized second derivatives are shown in Fig. 3.16 with the corresponding LDA calculations and the results obtained by convoluting the LDA valence Compton profiles with the spectral density function $A_{\text{CP}_{\text{max}}}(\omega - \tilde{\omega})$. Before calculating the second derivatives an additional convolution with a Gaussian having $f_a = 0.12$ a.u. is applied to the experimentally and theoretically obtained valence Compton profiles as discussed in section 3.2. The consideration of the final state interaction by the convolution of Eq. (3.17) significantly improves the agreement between experiment and theory and explains most of the broadening of the Compton profile beyond the experimental momentum space resolution.

The averaged amplitude $a = (a_1 + a_2)/2$ and the FWHM of the second derivatives of the calculated a_t, f_t and the experimentally determined a_e, f_e valence Compton profiles are estimated using the model function of Eq. (3.12) and the results are shown in Tab. 3.2³.

The difference of the squares of the FWHM of theory f_t and experiment f_e given by $\Delta = \sqrt{f_e^2 - f_t^2}$ yields the additional Gaussian convolution needed to get the same broadening in theory as observed in the experiment. The error of this difference is determined by evaluating the FWHM for different additional convolutions f_a between 0.7 a.u. and 1.7 a.u. as described in section 3.2 and the negative sign of Δ indicates $f_e < f_t$.

The FWHM of the Gaussian which causes the same broadening as a convolution with the spectral density function (SDF) is estimated to be 0.088 a.u. at $f_a = 0.12$ a.u. extra convolution. This value is in good agreement with the averaged value

³The statistical error of a_e and f_e is estimated as follows: The LDA Compton profile convoluted with the spectral density function is randomly noised by the statistical error of the experiment. Then the additional convolution with $f_a = 0.12$ a.u. is applied to the noised spectra and their averaged amplitude a_n and their FWHM f_n is determined utilizing the fit of the model function from Eq. (3.12). This procedure is repeated until the standard deviation of the various a_n and f_n converges. Assuming a Gaussian distribution of the obtained a_n and f_n the error of a_e and f_e is given by its standard deviation.

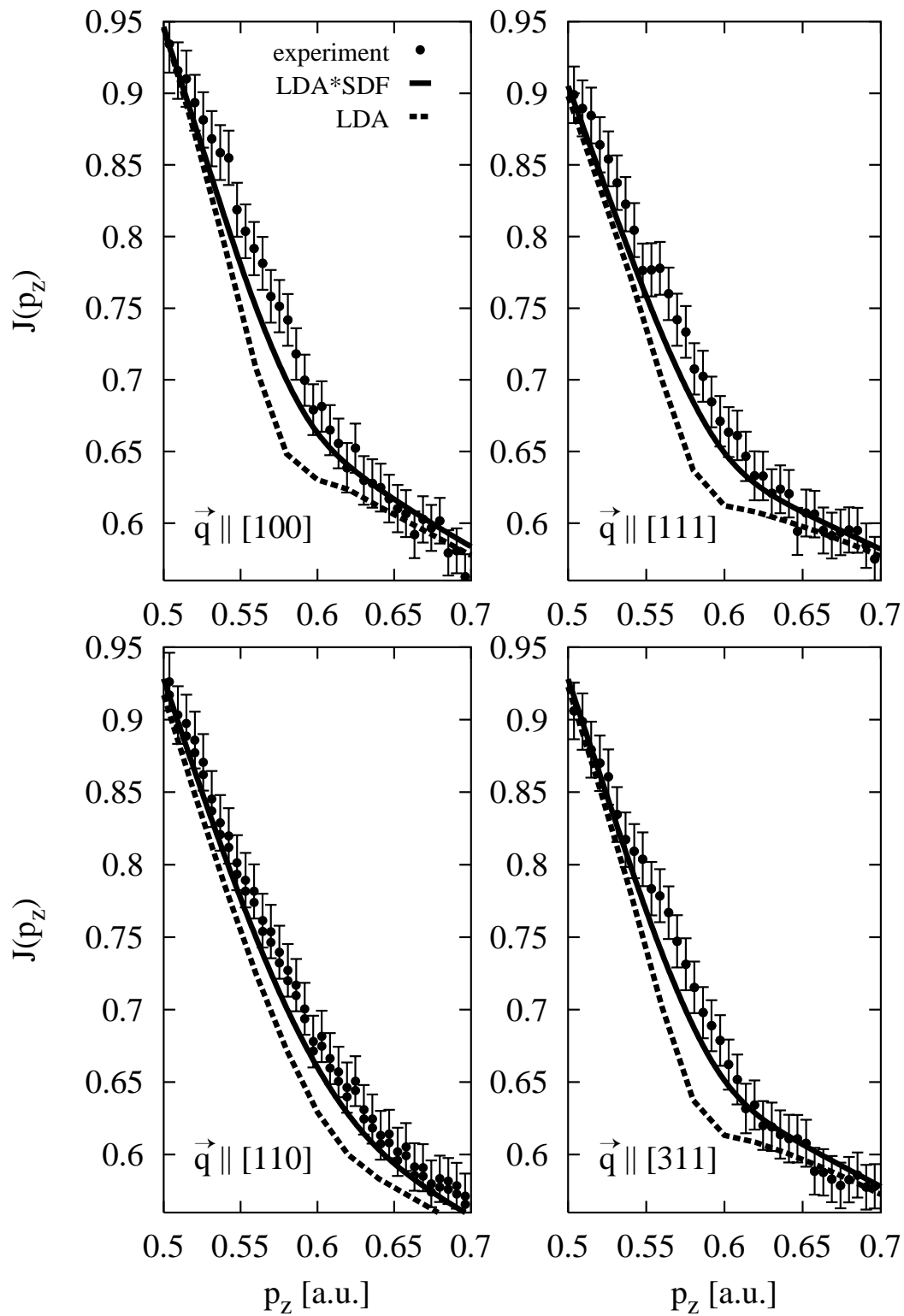


Figure 3.15: Experimental Compton profiles plotted around the Fermi break (dots) compared to the LDA calculations with (solid line) and without (dashed line) convolution with the spectral density function of the excited particle (SDF).

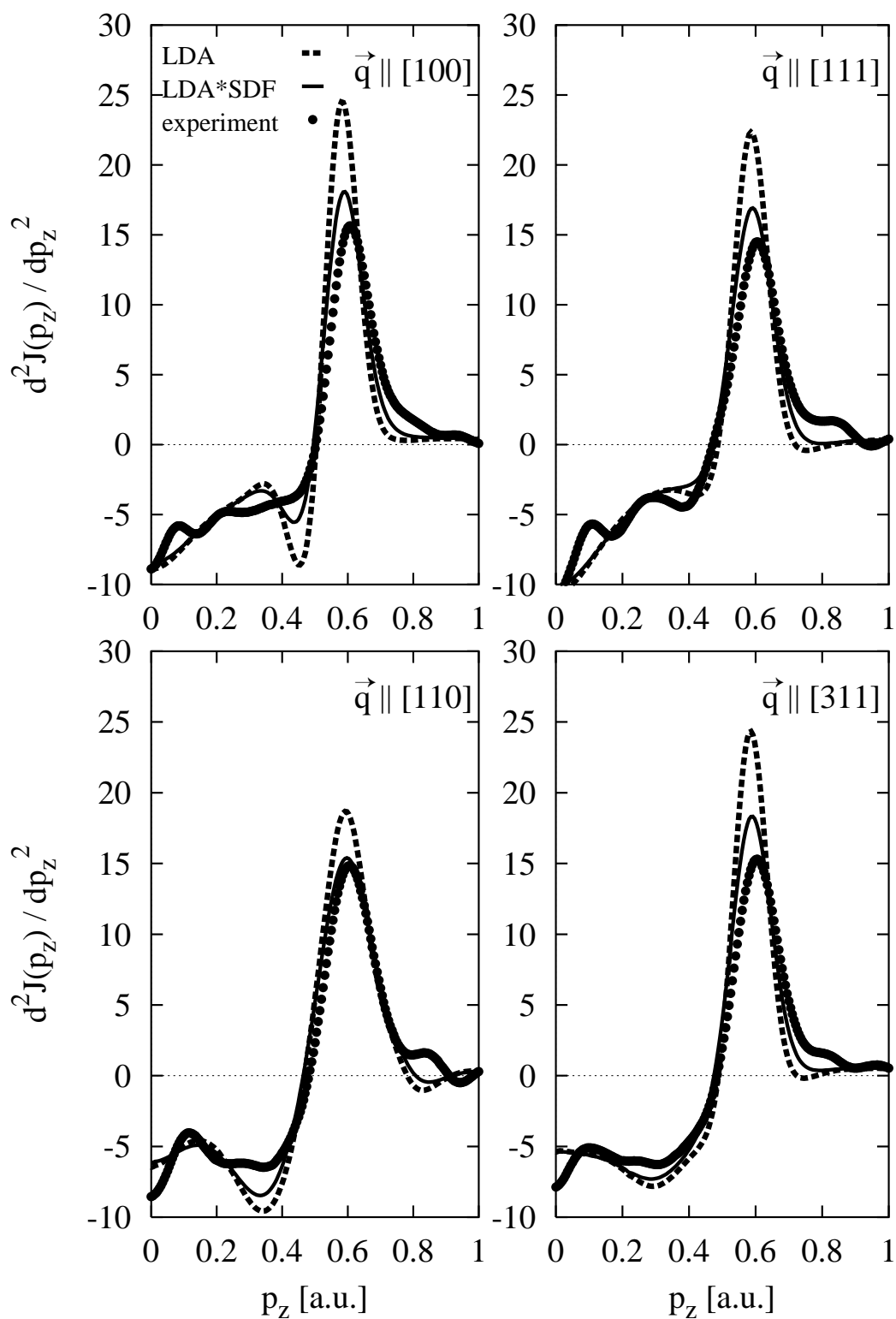


Figure 3.16: Symmetrized second derivatives of the experimentally obtained valence Compton profiles (dots) compared to LDA results with (solid line) and without (dashed line) convolution with the spectral density function of the excited particle (SDF).

3.4. Influence of the spectral density function of the particle on the valence Compton profile 63

of $\Delta_{\text{SDF}} = 0.092$ a.u. calculated from the LDA result for f_t with and without convolution by the spectral density function of the excited particle and confirms the assumption of Gaussian distributions in calculating Δ .

$\vec{q} \parallel$	[100]	[110]	[111]	[311]
amplitude				
a_t (LDA)	28.10	21.83	25.24	27.18
a_t (LDA*SDF)	20.86	18.60	19.25	20.77
a_e (Experiment)	17.83 ± 0.06	17.51 ± 0.06	15.79 ± 0.10	17.50 ± 0.06
FWHM [a.u.]				
f_t (LDA)	0.106	0.168	0.126	0.121
f_t (LDA*SDF)	0.135	0.188	0.164	0.153
f_e (Experiment)	0.154 ± 0.005	0.179 ± 0.005	0.189 ± 0.007	0.172 ± 0.005
Δ [a.u.]				
Exp. - LDA	0.112 ± 0.042	0.062 ± 0.039	0.141 ± 0.029	0.122 ± 0.022
Exp. - LDA*SDF	0.074 ± 0.058	-0.057 ± 0.063	0.094 ± 0.030	0.079 ± 0.028
Δ_{SDF} [a.u.]				
LDA*SDF - LDA	0.084	0.084	0.105	0.094

Table 3.2: Amplitude and FWHM of the second derivatives at the Fermi momentum of experiment, LDA and LDA convoluted with the spectral density function of the excited particle (SDF). Δ gives the additional Gaussian convolution needed to obtain in the theory the same broadening as in the experiment and Δ_{SDF} represents the Gaussian convolution assigned to the convolution with the spectral density function. The presented values are determined for $f_a = 0.12$ a.u. extra convolution.

The agreement between theory and experiment concerning the width and the amplitude of the second derivatives at the Fermi momentum is highly improved, if the convolution with the spectral density function of the final state is considered. Thus, the main part of the observed smearing at the Fermi momentum of the experimentally determined valence Compton profiles beyond the experimental momentum space resolution is attributed to the finite lifetime of the final state due to the imaginary part of the self-energy. This causes an intrinsic resolution limit for Compton scattering experiments at low incident energies and momentum transfers. In the present experiment the intrinsic momentum space resolution limit is 0.06 a.u., the width of the spectral density function of the excited particle for an incident energy around 9 keV and a momentum transfer of 5 a.u.

Nevertheless, even after convolution of the LDA valence Compton profiles with the spectral density function of the excited particle a discrepancy between experiment and theory remains. The second derivatives of the experimentally obtained Compton profiles are still broader than those of the theoretical ones, which confirms the well-known discrepancy between LDA or QMC calculations and experiment in the case of lithium. This discrepancy is often attributed to the inadequate treatment of electron-electron correlation effects in the Compton scattering process and forced a lot of discussion on the value of the renormalization constant z_F . To examine the high resolution Compton profiles on this basis, the reciprocal form factor $B(\vec{R})$ will be considered.

3.5 Reciprocal form factor

The valence Compton profiles are obtained by subtracting the asymmetrical core Compton profile and the multiple scattering contribution after the energy dependent corrections were performed. Then the reciprocal form factor $B(r)$ of the valence Compton profiles for $\vec{q}||[100], [110], [111]$, and $[311]$ is calculated at the corresponding lattice translation vectors \vec{R} . The uncertainties in extracting the valence Compton profile caused by the subtraction of the core and the multiple scattering contribution have no significant influence on the values of the reciprocal form factor for $r > 5$ a.u. since these contributions vary slowly as a function of p_z . In contrast, the valence Compton profile is localized in momentum space having a delocalized $B(r)$ function. For $r = |\vec{R}|$ the reciprocal form factor yields information about the occupation function $n(\vec{k})$ according to Eq. (1.52) and thus information, how electron-electron correlation affects the valence Compton profile. Fig. 3.17 shows the $B(\vec{R})$ values calculated from the experimental valence Compton profiles compared to the LDA theory, Lam-Platzman corrected, with and without convolution with the spectral density function of the excited particle.

The theoretical valence Compton profiles are convoluted with the momentum space resolution function and the experimental error of $B(\vec{R})$ is calculated according to the approximate equation $\sigma_{B(\vec{R})} = \frac{B_{\text{tot}}(0)}{\sqrt{N_{\text{tot}}}}$ [Pattison and Schneider 1978] to 0.0011 a.u. Here $B_{\text{tot}}(0)$ denotes the value of the reciprocal form factor of the total Compton profile at $|\vec{R}| = 0$ and N_{tot} is the total number of counts measured in the p_z regime, in which $B(\vec{R})$ is determined.

The theoretical values of $B(\vec{R})$ lie closer to the experimental ones, if the convolution with the spectral density function of the excited particle is applied to the LDA calculation. However, a strong discrepancy between experiment and theory remains, confirming the conclusions made at the end of section 3.4. As follows, the discrepancy obtained in the present experiment is confronted with the discrepancy between LDA and experimental results found in former valence Compton profile measurements of lithium [Schülke et al. 1996, Sternemann et al. 2000 (b)]. Tab. 3.3 represents the experimentally found values of $B(\vec{R})$ calculated for the smallest five lattice translation vectors \vec{R} utilizing the corresponding directional valence Compton profile. These values are compared to the results obtained from valence Compton profiles measured at 30 keV [Sternemann et al. 2000 (b)] for $\vec{q}||[110]$ with a momentum space resolution of $\Delta p_z = 0.10$ a.u. and at 31 keV [Schülke et al. 1996] for $\vec{q}||[100], [110], [111]$ and $[311]$ with $\Delta p_z = 0.17$ a.u.⁴ The

⁴In the paper of Schülke et al. [Schülke et al. 1996] the momentum space resolution is determined to be $\Delta p_z = 0.14$ a.u. This estimate neglects the distribution of effective scattering angles on the momentum space resolution as discussed in section 3.1.2. If this distribution is considered a momentum space resolution of $\Delta p_z = 0.17$ a.u. is obtained.

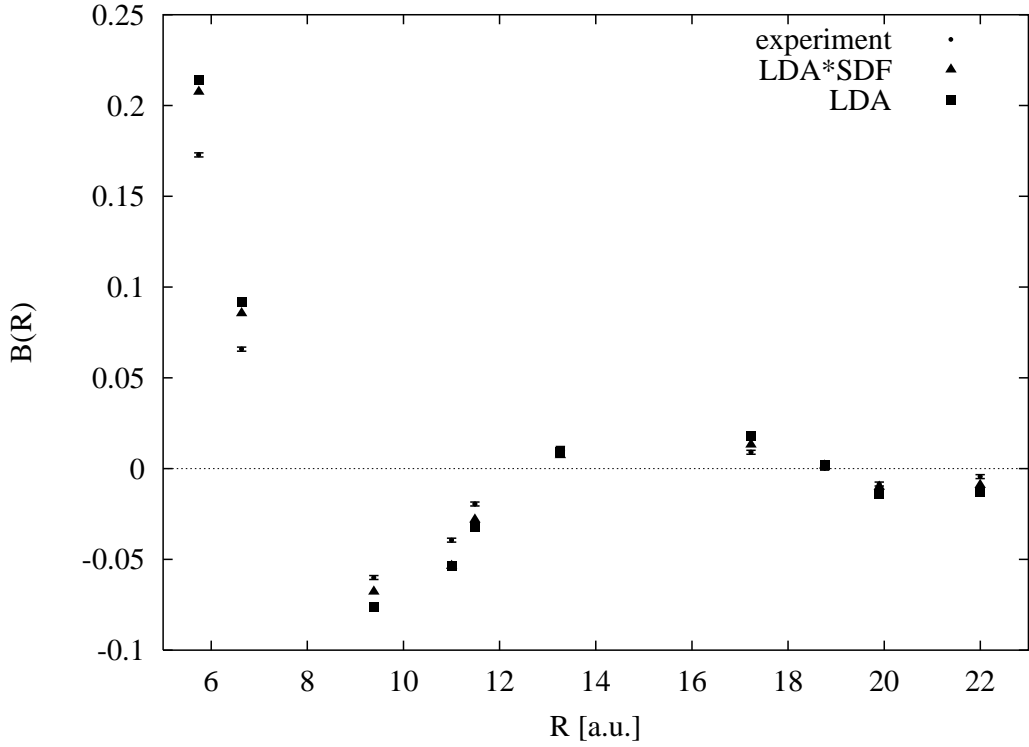


Figure 3.17: Values of the reciprocal form factor $B(\vec{R})$ calculated at the lattice translation vectors \vec{R} for $\vec{q} \parallel [100]$, $[110]$, $[111]$ and $[311]$. The experimental results (dots) are compared to LDA theory (squares) and LDA theory convoluted with the spectral density function of the excited particle (triangles).

values of $B(\vec{R})$ obtained from the experimental valence Compton profiles $B(\vec{R})_{\text{exp}}$ are confronted with the results of the LDA valence Compton profile computations (Lam-Platzman corrected) $B(\vec{R})_{\text{theory}}$, which are convoluted with the momentum space resolution function of the corresponding experiment. The convolution with the spectral density function effects only the measurement at 9 keV significantly since the FWHM of the final state spectral density function at incident energies around 30 keV and 31 keV is in the order of 0.009 a.u. on a p_z scale and thus negligible with respect to the experimental momentum space resolutions of 0.10 a.u and 0.17 a.u., respectively.

It has to be stressed that in the present study the discrepancy between LDA theory and the experimental valence Compton profiles, $\Delta_B = B_{\text{exp}} - B_{\text{theory}}$, is found to be roughly of the same order as obtained from measurements performed at larger incident energies having different momentum space resolutions. This means, that even though the broadening of the Compton profile is mainly attributed to the influence of the spectral density function of the excited particle, the final

$ \vec{R} $ [a.u.]	$ \vec{q} $	Δp_z [a.u.]	$B(\vec{R})_{\text{theory}}$	$B(\vec{R})_{\text{exp}}$	$ \Delta_B $
5.743	[111]	0.17	0.196	0.159	0.037
		0.02	0.208	0.173	0.035
6.633	[100]	0.17	0.082	0.060	0.022
		0.02	0.086	0.066	0.020
9.384	[110]	0.17	-0.061	-0.043	0.018
		0.10	-0.071	-0.051	0.020
		0.02	-0.068	-0.060	0.008
11.000	[311]	0.17	-0.045	-0.026	0.019
		0.02	-0.054	-0.039	0.015
11.486	[111]	0.17	-0.023	-0.016	0.007
		0.02	-0.028	-0.020	0.008

Table 3.3: Values of the reciprocal form factor $B(\vec{R})$ obtained from Compton profile measurements at different incident energies having different momentum space resolutions.

state interaction cannot account for the widely discussed discrepancy between LDA theory and experiment. Since the reciprocal form factor calculated at lattice translation vectors is directly related to the occupation function as emphasized in section 1.4, the observed discrepancy may be due to the inadequate treatment of electron-electron correlation within the Lam-Platzman correction.

3.6 Summary

The high resolution measurements of directional Compton profiles of lithium for $\vec{q} \parallel [100], [110], [111]$ and $[311]$ have shown that the sharp features at the Fermi momentum predicted by LDA theory, which should be resolved with the highly improved experimental momentum space resolution of $\Delta p_z = 0.022$ a.u., are still smeared out. The main part of this additional broadening can be attributed to the convolution of the valence Compton profile with the particle spectral density function, so that the broadening can be considered as a direct evidence of the interaction of the excited particle with the rest of the many-particle system. Thereby, an intrinsic resolution limit due to the final state interaction is given, when Compton profile measurements at low incident energies are performed. The contribution of the particle spectral density function to the momentum space resolution of Compton profile measurements at incident energies of 30 keV and 60 keV is estimated to be 0.009 a.u. and 0.002 a.u. FWHM, respectively. This emphasizes, that the improvement of the momentum space resolution beyond 0.05 a.u. in high resolution Compton scattering experiments requires incident photon energies larger than at least 30 keV. At these energies the influence of the spectral density function of the excited particle becomes more and more negligible. Recent Compton profile measurements of beryllium have shown a similar broadening of the Compton profiles beyond experimental resolution at an incident energy around 10 keV [Huotari et al. 2000] which may also be attributed to final state interactions. On the basis of the reciprocal form factor it is shown that the convolution of the lithium valence Compton profile with the particle spectral density function cannot account for the well-known discrepancy between LDA theory and experiment as found in Compton profile measurements performed at higher incident energies. Furthermore, the valence Compton profile exhibits an asymmetry, which agrees in sign, shape and amplitude with the predictions of the first order vertex correction to the fully self-energy corrected proper polarization function. The magnitude of the second order type vertex correction is presented, slightly improving the agreement between experiment and theory. Thus, this asymmetry is a direct indication of the particle-hole interaction in the course of the Compton scattering process and gives an evidence for the overcompensation of the self-energy by the vertex correction. In interpreting the measured valence Compton profiles it is necessary to go beyond the impulse approximation in the sense that final state interactions have to be considered within a many-particle calculation. This means, that the requirements of the impulse approximation are not fulfilled within the considered regime of energy and momentum transfer. The reliability of the presented experimental results is strongly confirmed since a second experiment performed by Hämäläinen et al. under similar experimental conditions at the beamline X21 of NSLS (National Synchrotron Light Source) yields the same conclusions [Sternemann et al. 2000].

Chapter 4

Temperature effects in Compton scattering from lithium

Recent high resolution Compton scattering studies on lithium [Sakurai et al. 1995, Schülke et al. 1996, Sternemann et al. 2000] and lithium-magnesium alloys [Stutz et al. 1999] have shown significant discrepancies between the experimentally observed valence Compton profiles and Korringa-Kohn-Rostoker LDA computations, in which the electron-electron correlation is generally included via the Lam-Platzman correction [Lam and Platzman 1974]. The calculated valence Compton profiles are above the experimental ones around $p_z = 0$ a.u. and below at $p_z \approx p_F$ as shown in Fig 4.1. The valence Compton profile anisotropies are overestimated by theory and the Fermi breaks are predicted to be much sharper in theory than in the experimental findings.

This discrepancy incited a lot of theoretical work, especially the value of the renormalization constant z_F for lithium was widely discussed, since it is a direct measure for the effect of electron-electron correlation on the electron momentum density describing the stepsize of the occupation function $n(\vec{k})$ at the Fermi momentum. An experimental work of Schülke et al. [Schülke et al. 1996] suggests z_F to be 0.1. This anomalous small value is in strong contradiction to jellium calculation results, where $z_F = 0.7$ was obtained [Takada and Yasuhara 1991]. A first principle calculation of the spectral density function utilizing the *GW* approximation by Kubo [Kubo 1997] shows much better agreement with the experimental valence Compton profiles than LDA theory, yielding $z_F \approx 0.25$ averaged over the three principal crystallographic symmetry directions. However, Schülke emphasized that Kubo's calculations exhibit an unphysical behaviour of the imaginary part of the self-energy at the Fermi level and obtained $z_F = 0.75$ using a similar computation [Schülke 1999]. Roughly the same result, namely $z_F = 0.72$, was found by Eguiluz et al. [Eguiluz et al. 2000]. A Bayesian analysis of the renormalization constant utilizing the high resolution Compton data of Sakurai [Sakurai et al. 1995] and Schülke [Schülke et al. 1996] yields $z_F \approx 0.5$ [Dobrzyński 2000].

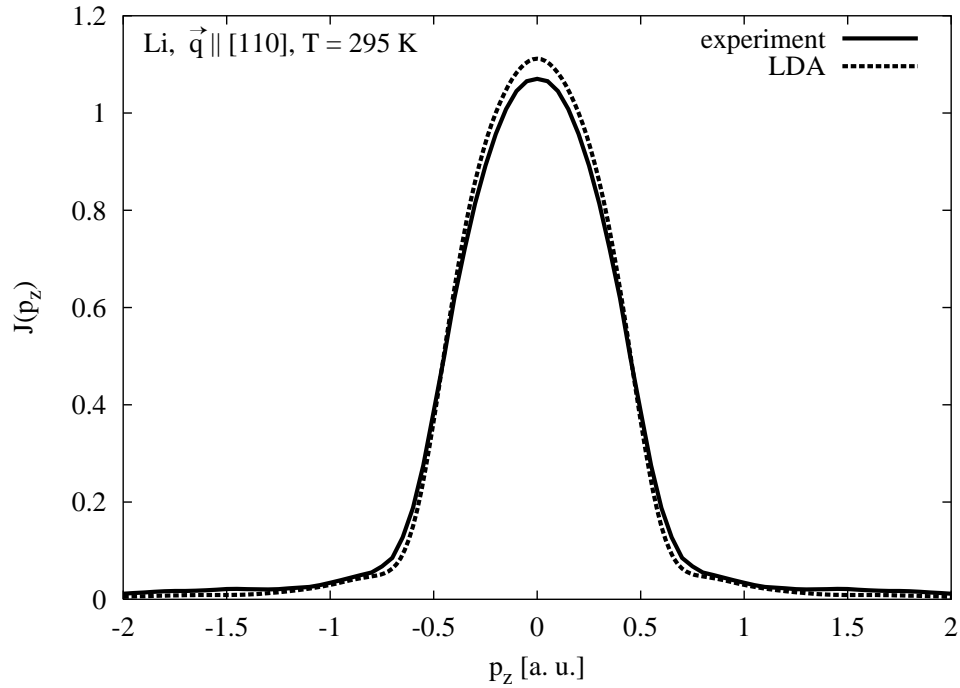


Figure 4.1: Lithium valence Compton profile measured for $\vec{q} \parallel [110]$ [Schülke et al. 1996] compared to the result of a Lam-Platzman corrected LDA calculation of Bansil and Kaprzyk [Sakurai et al. 1995] which is convoluted with the experimental momentum space resolution of $\Delta p_z = 0.17$ a.u.

Recent QMC calculations have shown that their correlation correction is in agreement with the Lam-Platzman correction used within LDA computations and overcomes only 30% of the discussed discrepancy [Filippi and Ceperley 1999], whereas a full-potential LAPW (Linearized Augmented Plane Wave) calculation by Baruah et al. [Baruah et al. 1999] exhibits a somewhat better agreement to the experimental valence Compton profiles and its first derivatives. However, the Compton profile anisotropies are still far from the experimental ones, which is traced back having neglected the anisotropic part of the electron-electron correlations within the Lam-Platzman scheme. Barbiellini [Barbiellini 2000] has criticized all these calculations [Sakurai et al. 1995, Schülke 1999, Eguiluz et al. 2000, Filippi and Ceperley 1999, Baruah et al. 1999] which utilize many-body wave functions within the free fermion nodal structure (FNS) and stated, that schemes like the antisymmetrized geminal product (AGP) going beyond the FNS could account for important correlation effects in the lithium valence Compton profiles. The deviation from the impulse approximation in terms of final state effects was discussed to be negligible at least for incident photon energies higher than 30 keV and thus cannot be the reason for the observed discrepancy [Sternemann et al. 2000].

A different approach to explain this discrepancy was tried by Dugdale and Jarlborg [Dugdale and Jarlborg 1998]. They simulated thermal disorder by introducing a static disorder within a supercell calculation utilizing a self-consistent LMTO (Linear Muffin-Tin Orbital) scheme in the case of lithium and sodium. They found an increasing broadening of the Compton profile in momentum space with increasing temperature resulting in a better agreement between theory and experiment. The calculated total Compton profiles are presented in Fig. 4.2. This approach seems to be reasonable since LDA, QMC, LAPW and *GW* calculations usually neglect the effect of temperature on the electron momentum density and their result has to be verified by an appropriate experiment.

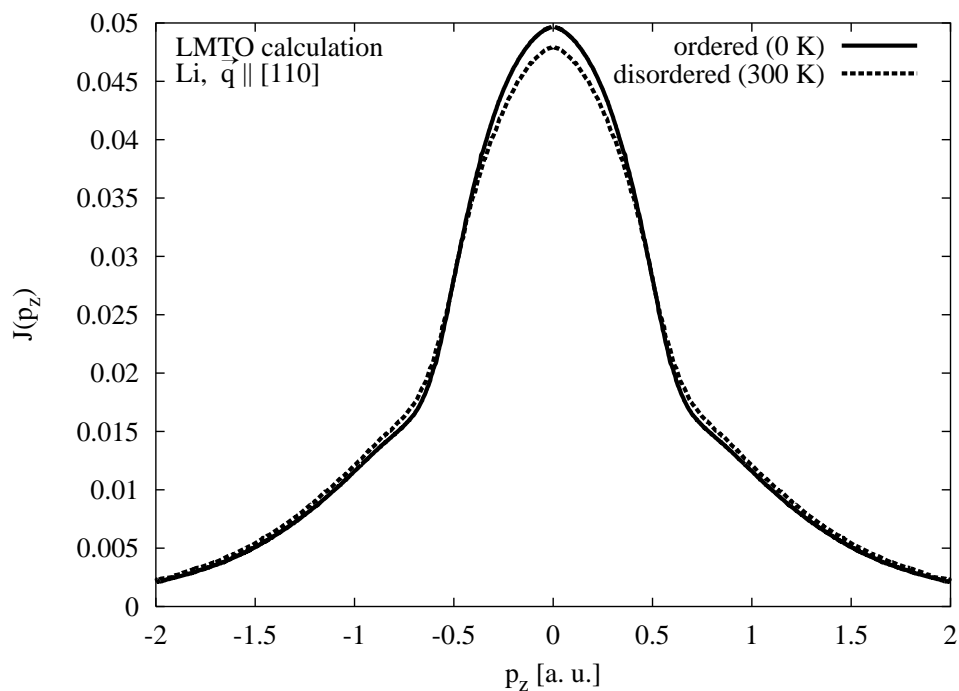


Figure 4.2: Temperature dependence of the total Compton profile of lithium for $\vec{q} \parallel [110]$ calculated utilizing a LMTO supercell approach [Dugdale and Jarlborg 1998] (Fig. 1(a) of their paper).

Such an experiment along with its interpretation is the topic this chapter. The experimental setup to measure the temperature effect on the lithium Compton profile is described. Then the valence Compton profile temperature differences are presented and compared to results obtained from temperature dependent jellium calculations and computations using a temperature dependent local pseudopotential.

4.1 Experiment

The experiment was performed at the Compton scattering beamline ID15B of ESRF (European Synchrotron Radiation Facility). After presentation of the experimental setup the data treatment is discussed and the temperature differences of the lithium valence Compton profiles are compared with the temperature effect predicted by the thermal disorder model of Dugdale and Jarlborg [Dugdale and Jarlborg 1998].

4.1.1 Experimental setup

The experimental setup of the scanning-type x-ray spectrometer of ID15B is illustrated in Fig. 4.3. The incident beam supplied by an asymmetrical multipole permanent-magnet wiggler was focussed on the lithium sample utilizing a Si(111) bent-crystal monochromator. The incident energy was 29.24 keV and the scattering angle was 173° . The scattered photons were analyzed in Rowland geometry utilizing a Si(400) bent analyzer crystal and were detected by a large-diameter NaI scintillation counter. A detailed description of the experimental setup is given elsewhere [Suortti et al. 1999]. The spectrometer was calibrated using the Sn K_{α_1} and K_{α_2} fluorescence lines having fluorescence energies of $E_{K_{\alpha_1}} = 25.271$ keV and $E_{K_{\alpha_2}} = 25.044$ keV.

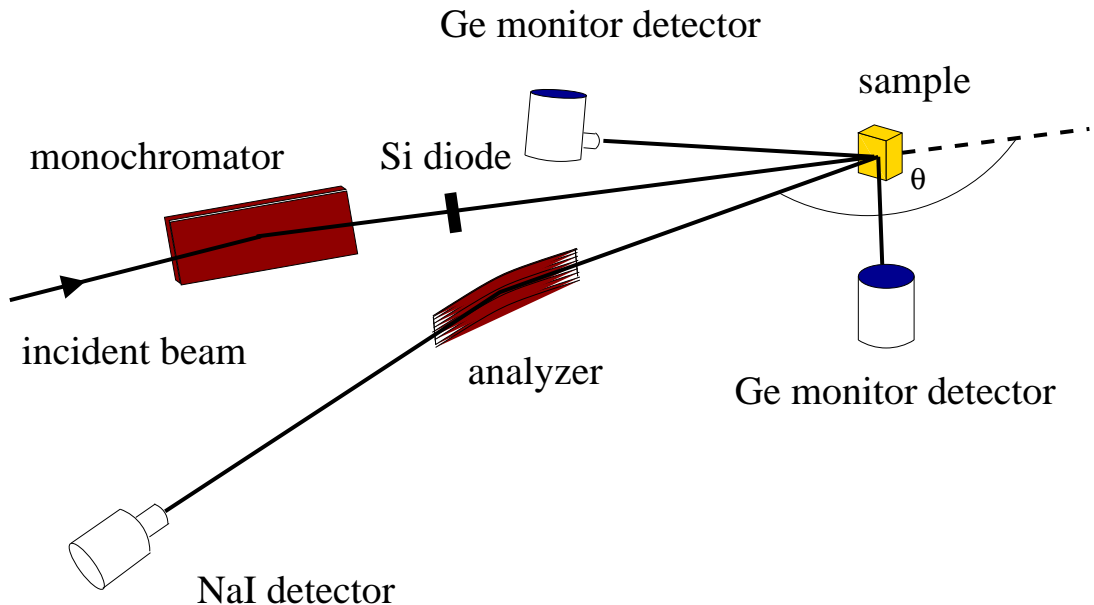


Figure 4.3: Experimental setup of the scanning-type x-ray spectrometer at the Compton scattering beamline ID15B of ESRF.

The lithium single crystal, a cuboid of 7 mm sidelength and 9 mm height, was mounted into a vacuum chamber which was evacuated to 10^{-5} mbar to avoid oxidation. The sample was etched as described in section 3.1.1 and retained the metallic shine until the end of the measurements, so that a contamination of the surface by oxidation can be excluded. Since the experimental momentum space resolution Δp_z depends strongly on the sample thickness, the effective scattering volume seen by the analyzer was restricted using a wolframcarbide rod, which was placed in the scattered beam obtaining an appropriate momentum space resolution (see Fig. 4.4). The Ge monitor detector was placed directly above the scattered beam to detect the scattering from the same effective sample volume as the analyzer does. Thus, the monitor signal was independent of beam position movements on the sample. A closed cycle cryostat was utilized with a temperature controller to stabilize the sample temperatures of 95 K and 295 K with an accuracy of ± 5 K. Lithium Compton profiles were measured for $\vec{q} \parallel [110]$ at 295 K, 95 K and again 295 K to validate the reversibility of the temperature effect. The total number of counts in the maximum of the Compton profile in the second measurement at room temperature was only about 1.3×10^5 in contrast to 2.8×10^5 obtained for the other profiles due to the lack of beamtime. The low temperature measurement was taken above 75 K, where the martensitic phase transition of lithium occurs [Smith 1987]. For each temperature several single spectra were measured, summed up and normalized to the signal of the Ge monitor detector.

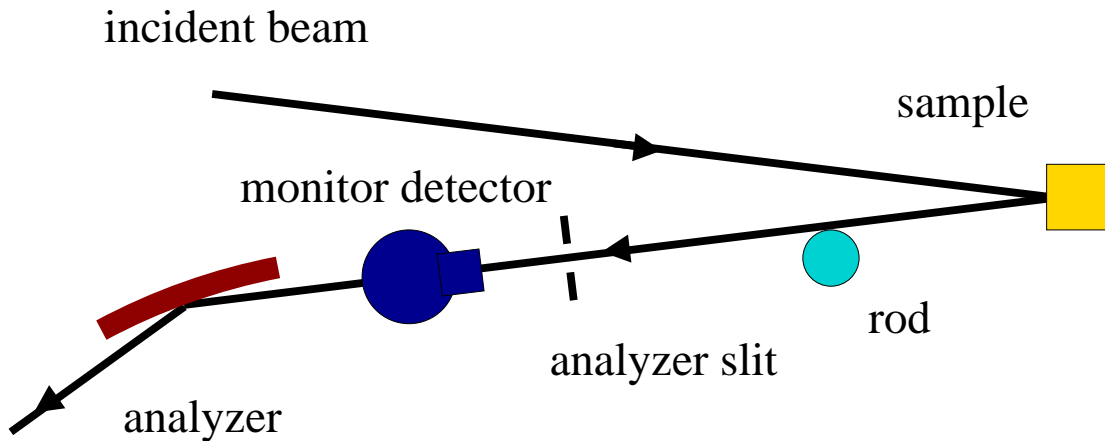


Figure 4.4: Reduction of the effective scattering volume utilizing a wolframcarbide rod. The monitor detector is placed directly above the scattered beam.

4.1.2 Data evaluation

The experimental Compton profiles are evaluated considering all energy dependent corrections $S(\omega_2)$, namely the vertical acceptance of the spectrometer, reflectivity of the analyzer crystal, absorption of the sample, air absorption, scale and relativistic correction and, at last, the subtraction of the multiple scattering contribution $M_S(p_z(\omega_2))$. The background B is assumed to be constant. In the case of the Compton spectrometer of ID15B the measured normalized intensity $I(\omega_2)$ is given by

$$I(\omega_2) = B + CS(\omega_2) (J(p_z(\omega_2)) + M_S(p_z(\omega_2))) . \quad (4.1)$$

C contains all factors which are not energy dependent. The deadtime correction of the detector signal is negligible due to the small counting rates.

Energy dependent corrections

The vertical acceptance of the spectrometer is limited either by the vertical opening of the analyzer slit ($h_S = 35$ mm), the height of the analyzer crystal itself ($h_A = 61$ mm) or the vertical opening of the detector ($h_D = 70$ mm), depending on the values of the distances between sample and analyzer p and analyzer and detector q . The distance between sample and analyzer slit ($d = 1083$ mm) is constant, whereas p and q are functions of the Bragg angle θ_B . Then the vertical acceptance is given by

$$S_{\text{ac}}(\omega_2) = \left(\text{Min} \left\{ \frac{h_S}{d}; \frac{h_A}{p(\theta_B)}; \frac{h_D}{p(\theta_B) + q(\theta_B)} \right\} \right) . \quad (4.2)$$

The reflectivity of the analyzer crystal $S_{\text{ref}}(\omega_2)$ is computed on the basis of the dynamical theory of diffraction utilizing the program REFLECT available at ID15B taking into account the polarization of the scattered photons [Erola et al. 1990].

The sample absorption $S_{\text{abs}}^{\text{sample}}(\omega_2)$ is accounted for according to Eq. (3.8) and the air absorption $S_{\text{abs}}^{\text{air}}(\omega_2)$ is expressed as

$$S_{\text{abs}}^{\text{air}}(\omega_2) = e^{-\mu_{\text{air}}(\omega_2)(p(\theta_B)+q(\theta_B))} . \quad (4.3)$$

The scanning spectrometer measures the intensity of the scattered photons as a function of the Bragg angle and not as function of energy. Thus, a scale correction has to be performed via

$$\frac{d^2\sigma}{d\Omega d\omega_2} = \frac{d^2\sigma}{d\Omega d\theta_B} \frac{d\theta_B}{d\omega_2}, \quad (4.4)$$

which yields

$$S_{\text{scale}}(\omega_2) = \frac{d\omega_2}{d\theta_B} = \frac{\omega_2}{\tan\theta_B}. \quad (4.5)$$

Since the incident photons were linear polarized with respect to the scattering plane the relativistic correction $S_{\text{rel}}(\omega_2)$ is performed using Eq. (3.9). Then the total energy dependent correction factor can be expressed by

$$S(\omega_2) = S_{\text{ac}}(\omega_2) S_{\text{ref}}(\omega_2) S_{\text{abs}}^{\text{sample}}(\omega_2) S_{\text{abs}}^{\text{air}}(\omega_2) S_{\text{scale}}(\omega_2) S_{\text{rel}}(\omega_2). \quad (4.6)$$

After performing the energy dependent corrections the energy scale is transformed to the momentum scale. The correction factors are shown in Fig. 4.5.

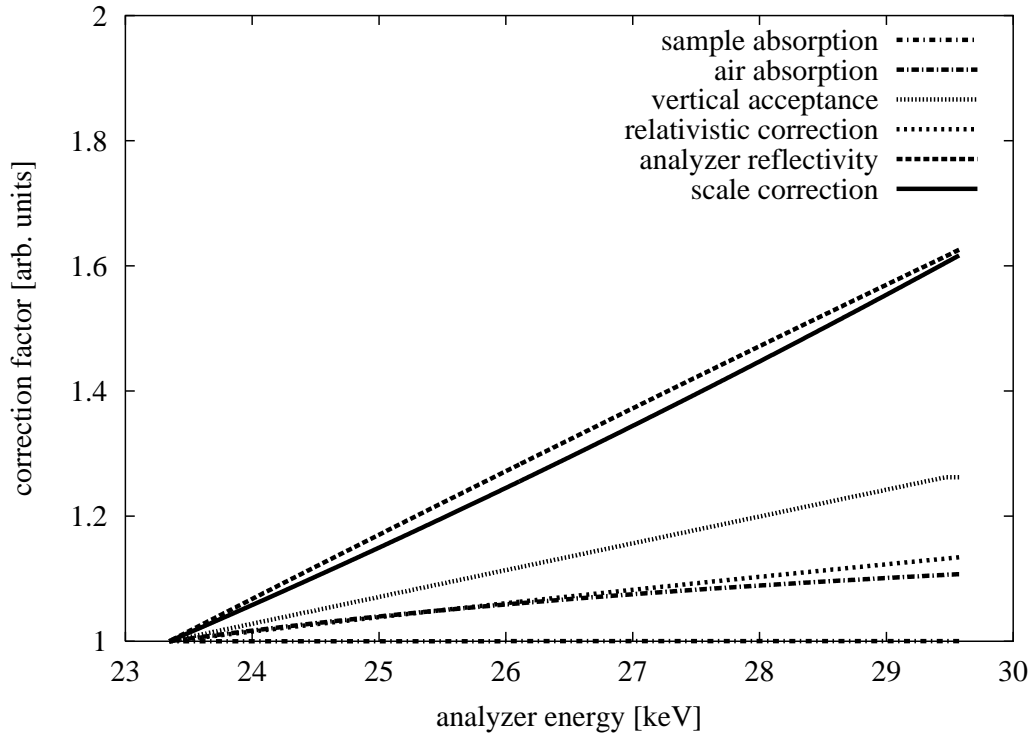


Figure 4.5: Energy dependent correction factors for the experimental lithium spectra measured with the scanning-type x-ray spectrometer of ID15B. The first value of each correction factor is normalized to one which allows for a comparison of the different corrections.

Multiple scattering, core Compton profile and normalization

The multiple scattering contribution is modeled using the Monte Carlo simulation described in section 3.1.2 and the result is shown in Fig. 4.6 together with the calculated core electron Compton profile utilizing the first correction to the non-relativistic Compton scattering cross section [Holm and Ribberfors 1989].

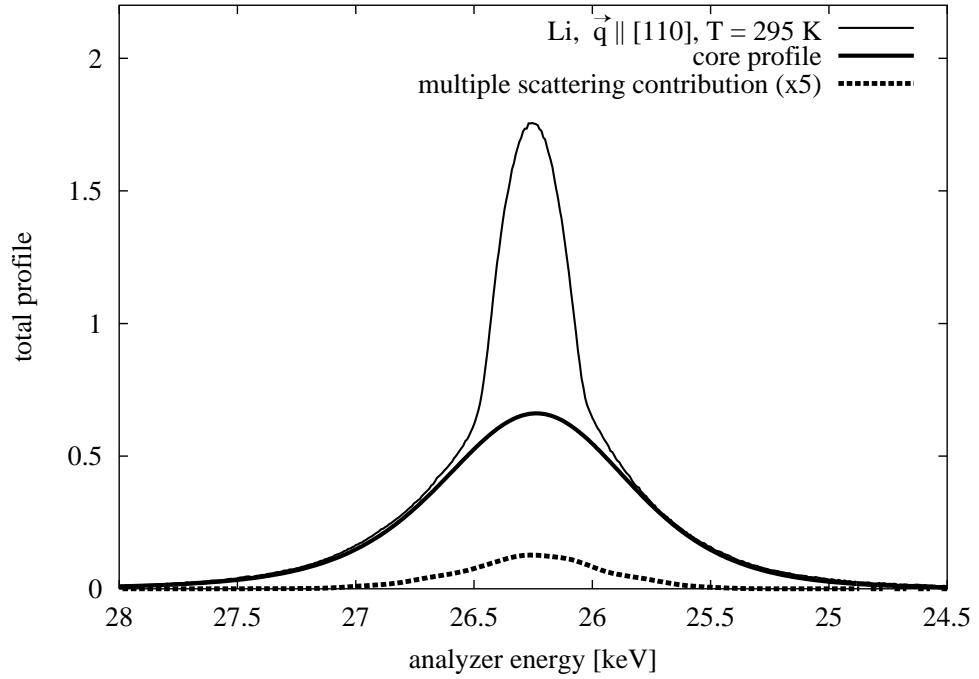


Figure 4.6: Total profile after energy dependent corrections for $\vec{q} \parallel [110]$ at 295 K plotted with the calculated core electron Compton profile and the multiple scattering contribution, which is enhanced by a factor of 5.

The calculation of the multiple scattering contribution remains somehow ambiguous corresponding to the complicated scattering geometry by using the wolframcarbide rod. However, the sample geometry is identical for all measurements so that the multiple scattering contribution cancels out if Compton profile differences are considered. Utilizing the normalization condition (Eq. (1.31)), the Compton profiles are obtained on absolute scale and the constant C is given by

$$C = \frac{\int_{-p_v}^{p_v} dp_z \frac{I(\omega_2) - B}{S(\omega_2)}}{\left(N_{\text{val}} + \int_{-p_v}^{p_v} dp_z (J_{\text{core}}(p_z(\omega_2)) + M_s(p_z(\omega_2))) \right)}. \quad (4.7)$$

N_{val} denotes the number of valence electrons and $-p_v$ to p_v determines the momentum range where the valence electrons contribute to the Compton profile.

momentum space resolution

The momentum space resolution is given by

$$\Delta p_z = \sqrt{\left(\frac{\partial p_z}{\partial \theta}\right)^2 \Delta \theta^2 + \left(\frac{\partial p_z}{\partial \omega_2}\right)^2 \Delta \omega^2}. \quad (4.8)$$

with a negligible uncertainty of the scattering angle of $\Delta \theta = 0.21^\circ$ and an energy width of the quasi-elastic line of $\Delta \omega_0 = 51$ eV. The energy dependence of the resolution function of the spectrometer is estimated to be $\Delta \omega \approx \left(\frac{\omega_2}{\omega_1}\right)^3 \Delta \omega_0$ with $\omega_1 = 29.24$ keV [Suortti et al. 1986]. Fig. 4.7 shows the total momentum space resolution Δp_z as a function of p_z . In the regime of the valence Compton profile the momentum space resolution is assumed to have a constant value of 0.1 a.u. This defines the width of the Gaussian used to simulate the influence of the experimental resolution within the calculations.

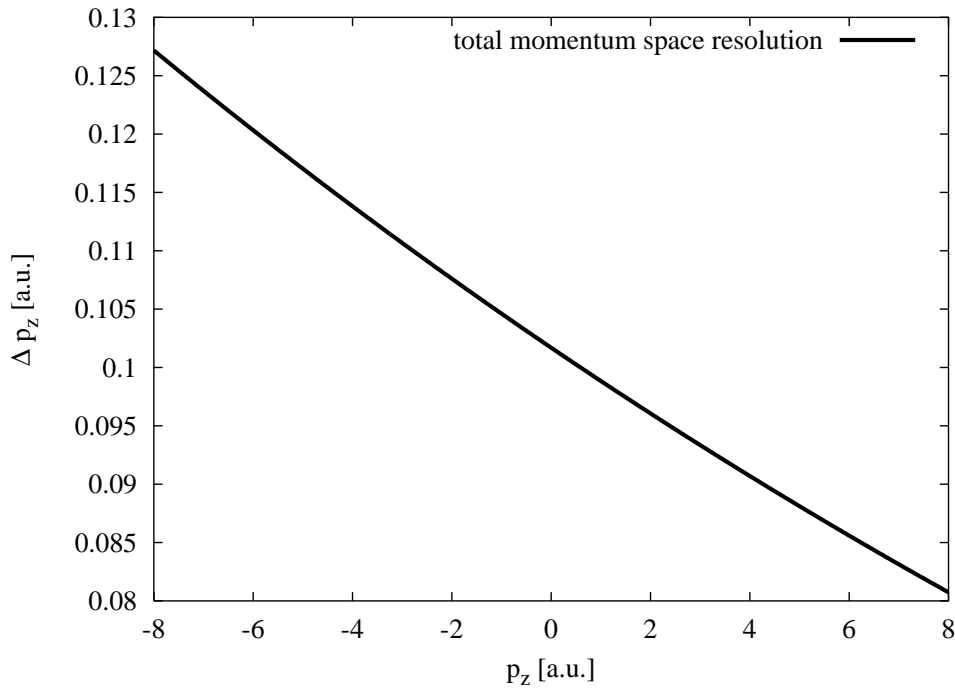


Figure 4.7: Total momentum space resolution of the Compton profile measurements at ID15B as a function of p_z .

4.2 Experimental results

The experimentally observed total Compton profiles of lithium are in agreement with the symmetrized lithium Compton profile for $\vec{q} \parallel [110]$ obtained from the measurements performed with the Compton spectrometer at the beamline W2 of HASYLAB [Schülke et al. 1996]. Fig. 4.8 shows the result of this experiment compared with the first measurement at $T = 295$ K, which is additionally convoluted with a Gaussian of 0.137 a.u. FWHM to simulate the momentum space resolution $\Delta p_z = 0.17$ a.u. of the HASYLAB measurement.

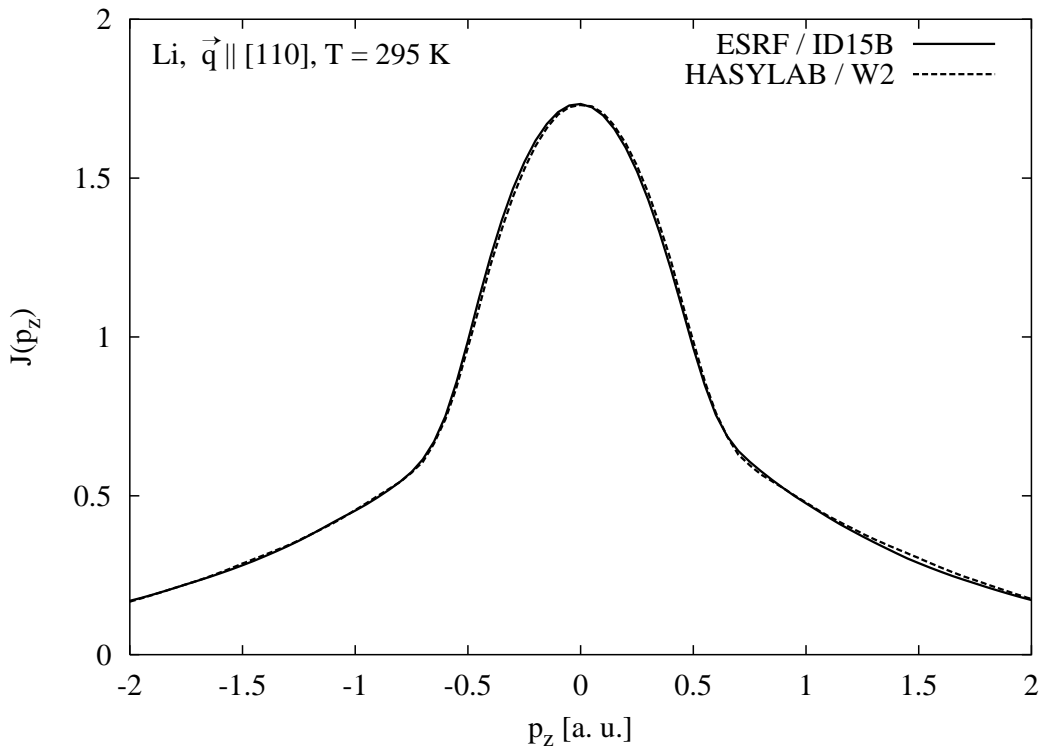


Figure 4.8: Lithium Compton profile measured at ID15B / ESRF (solid line) compared with the W2 / HASYLAB result (dashed line) [Schülke et al. 1996].

In Fig. 4.9 the total Compton profiles at $T = 295$ K and $T = 95$ K are presented. The upper panel shows the result measured at room temperature before the sample was cooled down to 95 K (first measurement), whereas the lower panel shows the Compton profile at room temperature taken after the measurement at 95 K (second measurement). The Compton profiles obtained at room temperature (solid line) lie above the Compton profile measured at 95 K (dashed line) around $p_z = 0$ a.u. and below at $p_z \approx p_F = 0.589$ a.u., the jellium Fermi momentum.

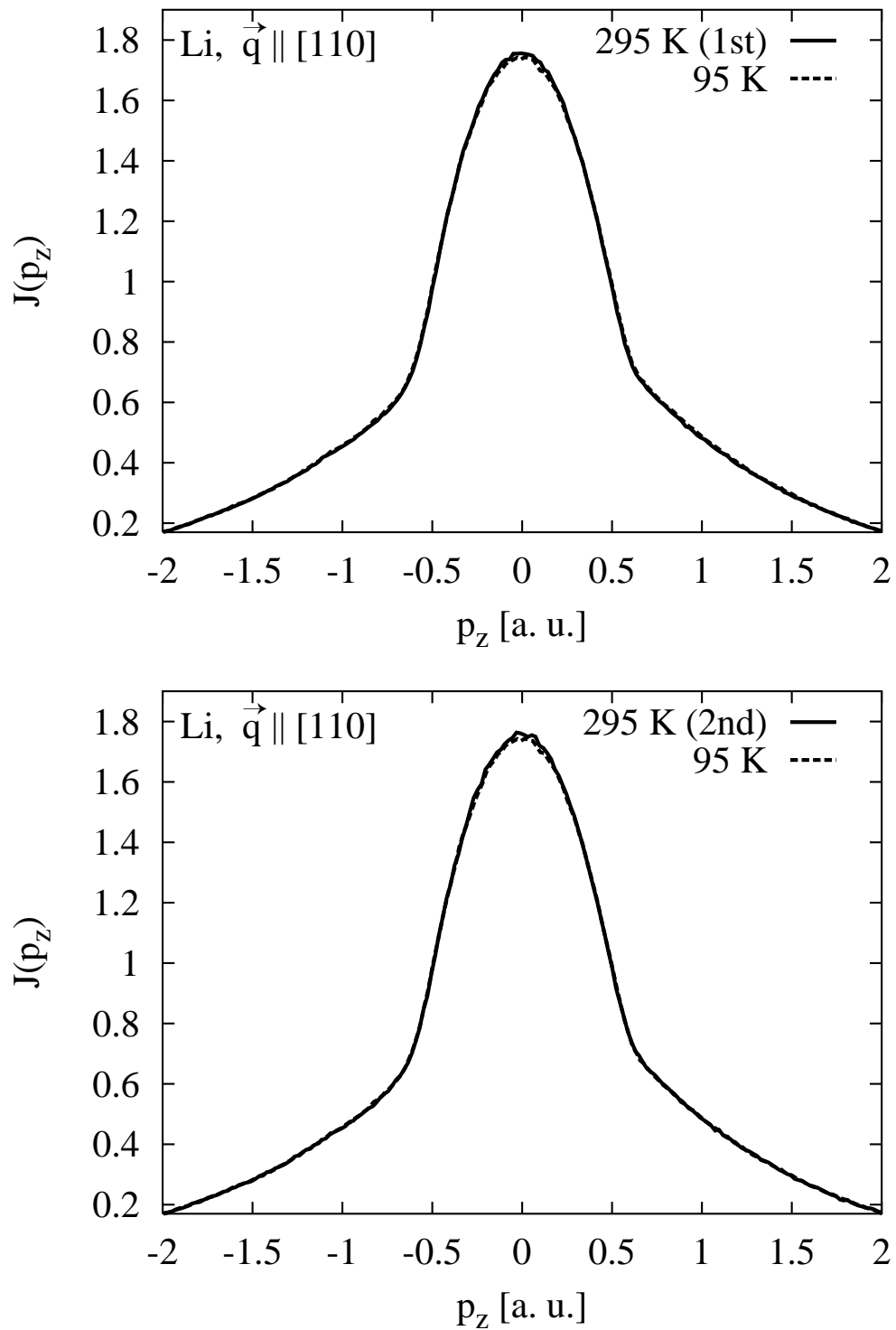


Figure 4.9: Total Compton profiles measured at $T = 295$ K (solid line) and $T = 95$ K (dashed line).

To extract the small temperature effect, the Compton profile differences $J(p_z, T = 95\text{K}) - J(p_z, T = 295\text{K})$ are calculated. The obtained differences are expressed in percent of the maximum value of the valence Compton profile measured at 95 K. By calculating the Compton profile differences all systematic errors cancel out provided the Compton profile asymmetries $J_{\text{asym}} = J(p_z) - J(-p_z)$ of the profiles utilized to calculate the difference are identical. The differences of the Compton profile asymmetries $J_{\text{asym}}(T = 95\text{K}) - J_{\text{asym}}(T = 295\text{K})$ are shown in Fig 4.10 together with its smoothed curve plotted as a solid line. The asymmetries of the Compton profiles measured at room temperature and at 95 K are almost identical if the first measurement at room temperature is considered, whereas the difference of the asymmetry of the second measurement at room temperature and the asymmetry of the Compton profile observed at 95 K exhibits a significant discrepancy around $p_z \approx 0.75$ a.u. marked by the arrow. This indicates that possibly a systematic error occurred in the measurement of the second room temperature Compton profile, so that the difference calculated utilizing the second measurement will exhibit some structure due to this artefact. The systematic error may be due to normalization problems since the normalized counts $N_{\text{tot}} = N_{\text{detector}}/N_{\text{monitor}}$ of the total profile are identical for the first measurement at 295 K and the 95 K measurement but differ significantly from the second measurement at 295 K of about 9%. Thus, the second difference has to be considered with care in the p_z regime between 0.5 a.u. and 0.9 a.u.

The Compton profile differences are presented in Fig. 4.11 compared to the temperature effect calculated by Dugdale and Jarlborg taken from Fig. 1(a) of their paper [Dugdale and Jarlborg 1998]. Within this calculation a momentum space resolution of $\Delta p_z = 0.12$ a.u. was assumed. The theoretical temperature difference is rescaled to the value of the valence Compton profile at $p_z = 0$ a.u. to enable the comparability with the experimentally obtained differences. The difference including the second measurement at room temperature is close to the difference utilizing the first measurement within experimental error as long as the p_z regime is considered, where no systematic error occurred. However, both spectra differ significantly between 0.6 a.u. and 0.8 a.u. due to the fact that the Compton profile asymmetries are not identical (see the arrow in Fig. 4.11). Nevertheless, the main features of the experimental temperature effect are found in both differences. The valence Compton profiles measured at room temperature lie above the valence Compton profile measured at 95 K around $p_z = 0$ a.u. and below at $|p_z| \geq p_F$ which means that the valence Compton profile is narrowed with increasing temperature. For $|p_z| \geq 1.8$ a.u. the experimental differences vanish within experimental errors indicating that no temperature effect with respect to the core electron contribution could be detected.

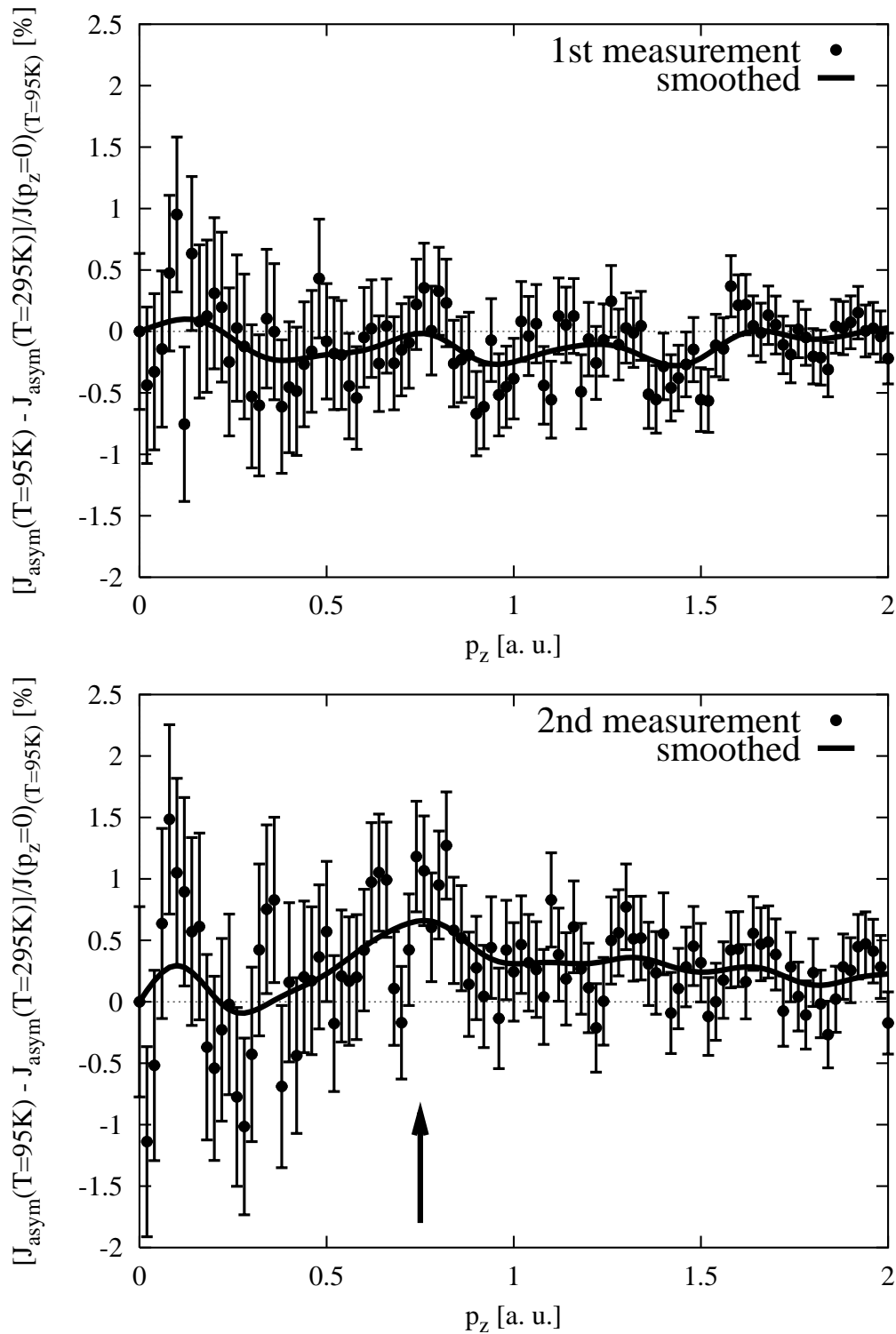


Figure 4.10: Differences of the Compton profile asymmetries $J_{\text{asym}}(T = 95\text{K}) - J_{\text{asym}}(T = 295\text{K})$. The solid line denotes the smoothed differences and the arrow marks the significant deviation of the asymmetries occurring if the second measurement at room temperature is used.

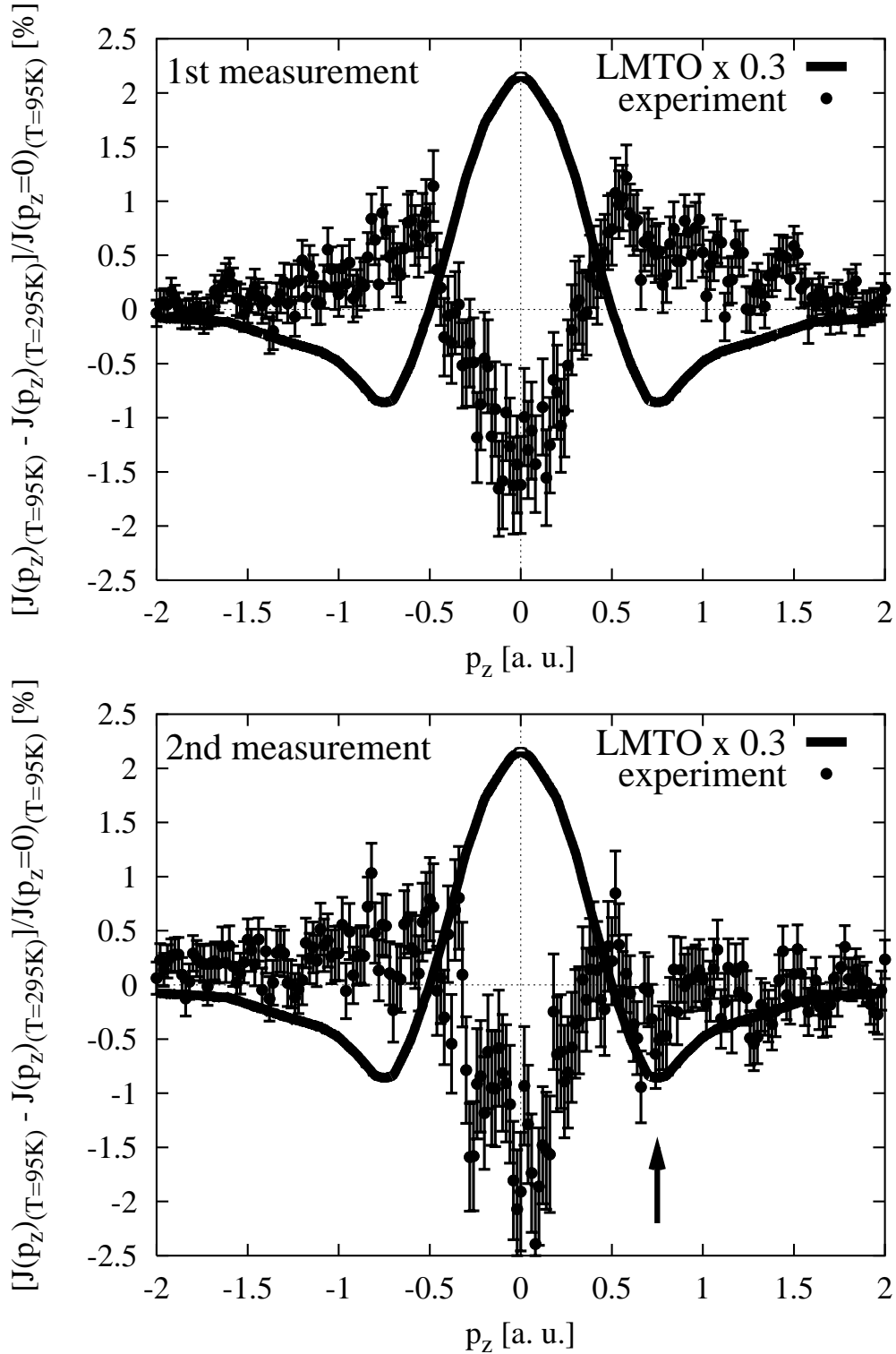


Figure 4.11: Compton profile differences $J(p_z, T = 95\text{K}) - J(p_z, T = 295\text{K})$ compared with the temperature difference extracted from the thermal disorder model of Dugdale and Jarlborg [Dugdale and Jarlborg 1998]. The calculation is scaled by a factor of 0.3 and plotted as a solid line. The arrow marks the position of the feature due to the deviation of the Compton profile asymmetries (see text).

The experimentally observed temperature effect is in contrast to the predictions of the thermal disorder model since the result of the calculation deviates in sign and also in amplitude from the measured one. Thus it can be excluded that the discussed discrepancy between usual band calculation theory and experiment can be attributed to thermal disorder. Furthermore, the experimental result suggests that the agreement between experiment and theory should get worse, when temperature effects are included within a bandstructure calculation.

In the following sections the experimental findings will be discussed in terms of the temperature effect on the lattice constant and on the crystal potential, respectively. Temperature dependent jellium calculations and computations using a temperature dependent empirical local pseudopotential scheme are performed to find a suitable model for the theoretical description of the temperature effect obtained by the experiment.

4.3 The homogeneous interacting electron gas

The homogeneous jellium is described by a system of N electrons embedded into a uniform positive charge background. This simple system is fully determined by the free electron gas parameter r_s , which is the radius of the sphere occupied by one electron in units of the Bohr radius (0.529 Å). The free electron gas parameter can be written as

$$r_s = \left(\frac{3}{4\pi} \frac{V_e}{N_e} \right)^{\frac{1}{3}} = \left(\frac{9\pi}{4} \right)^{\frac{1}{3}} \frac{1}{p_F} \quad (4.9)$$

with the volume of the unit cell V_e and the number of atoms in the unit cell N_e . Via V_e the electron gas parameter r_s is directly related to the lattice constant l . Since no lattice effects are considered the valence Compton profile is obtained from Eq. (1.27) to

$$J(p_z) = \int \int dp_x dp_y n(p) \quad (4.10)$$

utilizing a radial symmetric occupation function $n(k)$ in Eq. (1.42). Schülke et al. [Schülke et al. 1996] proposed a model for the correlated occupation function which contains the renormalization constant z_F as single free parameter. This model found successful application in the interpretation of lithium and aluminium valence Compton profiles [Schülke et al. 1996, Suortti et al. 2000] and is given by

$$\begin{aligned} n(k) &= (1-a) - \frac{1}{2}(1-a-z_F) \left(\frac{k}{p_F} \right)^8 & k < p_F \\ &= \frac{1}{2}(1-a-z_F) \left(\frac{p_F}{k} \right)^8 & k > p_F. \end{aligned} \quad (4.11)$$

The constant a equals to $\frac{9}{64}(1-z_F)$ as calculated by using the normalization condition

$$4\pi \int_0^{\infty} n(k) k^2 dk = \frac{4\pi}{3} p_F^3. \quad (4.12)$$

Within the simple $n(k)$ model presented in Eq. (4.11) the temperature influence on the valence Compton profile has to be accounted for utilizing a temperature dependent lattice constant l [Eisenmann and Schäfer 1986]. This affects the renormalization constant z_F and the Fermi momentum p_F via r_s . Takada and Yasuhara

[Takada and Yasuhara 1991] calculated the correlated occupation function $n(k/p_F)$ for $r_s = 1, 3, 5$. By interpolating the occupation functions for a given r_s the renormalization constant z_F is estimated. Tab. 4.1 shows the temperature dependence of the model parameters l, r_s, z_F , and p_F used within the jellium calculations.

T [K]	l [Å]	r_s [a.u.]	z_F	p_F [a.u.]
295 K	3.5104	3.2662	0.6994	0.5876
95 K	3.4848	3.2424	0.7011	0.5919

Table 4.1: Temperature dependence of the model parameters used within the jellium calculation.

The renormalization constant z_F varies by about 0.24% which causes a negligible influence on the valence Compton profile differences, so that the main temperature effect is due to the variation of the Fermi momentum with temperature (0.73%). The temperature difference obtained from the jellium computations is presented in Fig. 4.12 as a thick solid line in comparison to the experimental results.

The jellium calculation shows a qualitative agreement with the experiment. The theoretical difference is negative around $p_z = 0$ a.u. and positive at $p_z \approx p_F$. However, there exist discrepancies. The experimentally found temperature difference exhibits contributions for $p_z > p_F$ and shows a larger negative amplitude around $p_z = 0$ a.u. A chi-square test was performed utilizing the definition

$$\chi^2 = 1/N \sum_{k=1}^N \frac{(\Delta J_k^{\text{exp}} - \Delta J_k^{\text{calc}})^2}{\sigma_k^2}, \quad (4.13)$$

N being the number of datapoints, $\Delta J_k^{\text{exp}}, \Delta J_k^{\text{calc}}$ the experimentally determined and the calculated values of the valence Compton profile temperature differences, respectively, and σ_k the statistical error of the experimental differences.

The chi-square test yields $\chi^2 = 2.1$ (first measurement) and $\chi^2 = 1.8$ (second measurement) which is far from $\chi^2 = 1$. If $\chi^2 > 1$, there exists significant deviations between the theoretical and the experimental findings, whereas $\chi^2 < 1$ indicates an overestimation of the experimental error. In calculating χ^2 for the second measurement only the part of the valence Compton profile is considered which corresponds to negative p_z to exclude the artefact marked by the arrow in Fig. 4.12.

In contrast experimental results obtained in temperature dependent valence Compton profile measurements of aluminium [Sternemann et al. 2000 (c)] show a good overall agreement ($\chi^2 = 0.97$) between the experiment and a jellium calculation as presented in Fig. 4.13.

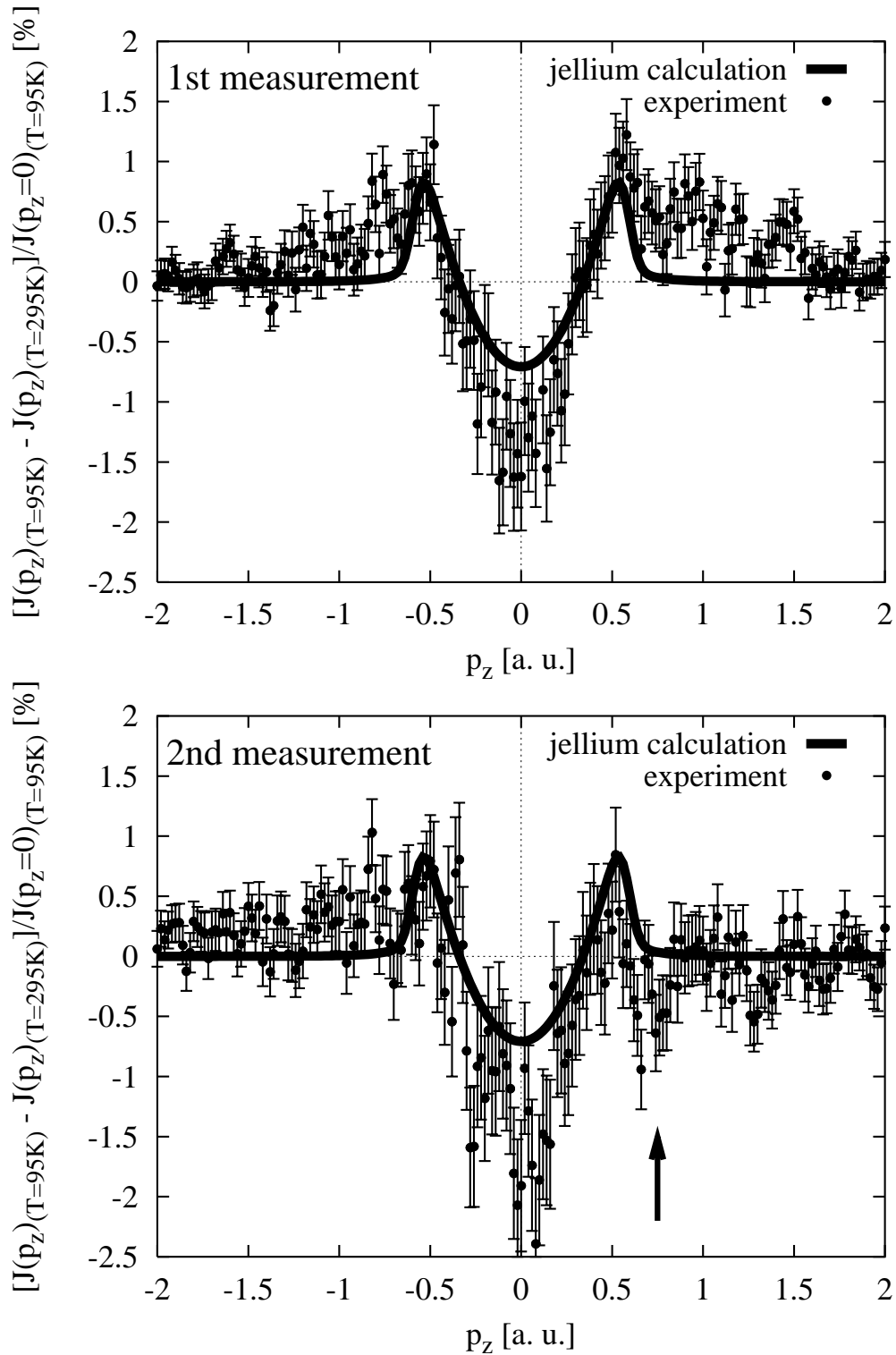


Figure 4.12: Compton profile differences $J(p_z, T = 95\text{K}) - J(p_z, T = 295\text{K})$ compared to the result of the temperature dependent jellium calculation. The arrow indicates the artefact (see text).

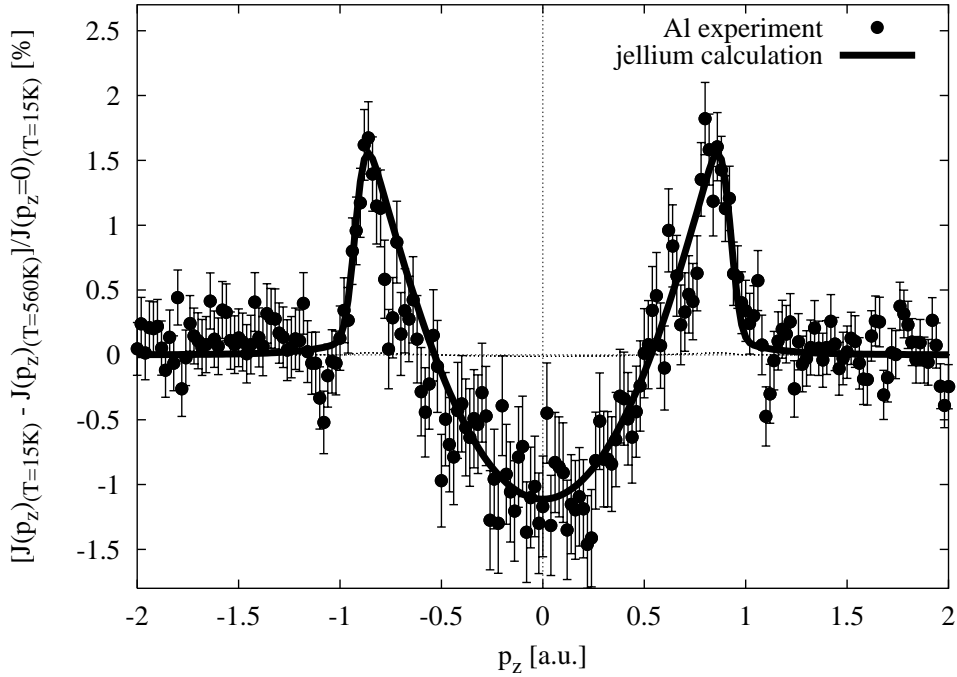


Figure 4.13: Temperature effect on the valence Compton profile of aluminium $J(p_z, T = 15\text{K}) - J(p_z, T = 560\text{K})$ compared to a temperature dependent jellium calculation [Sternemann et al. 2000 (c)].

The difference between the lithium and the aluminium results can be understood, when the calculated electron momentum densities [Papanicolaou et al. 1991] are considered. Aluminium seems to be a good example for a nearly free electron system since the electron momentum density including its lattice induced higher momentum components is approximately isotropic and the directional valence Compton profile differences are found to be small compared to lithium [Suortti et al. 2000]. Thus, the main contributions of the Umklapp-processes cannot be attributed to a single directional valence Compton profile so that the variation of the lattice constant dominates the temperature effect measured for aluminium [Sternemann et al. 2000 (c)]. In contrast, the electron momentum density of lithium exhibits a strong lattice induced contribution centered at $\vec{p} = (0.6, 0.6, 0)$ a.u. [Papanicolaou et al. 1991]. Thus, the corresponding valence Compton profile measured for $\vec{q} \parallel [110]$ is strongly affected by the higher momentum contributions compared to the directional valence Compton profiles for $\vec{q} \parallel [100]$ and $[111]$. Due to this fact it is necessary to consider the temperature influence on the crystal potential within a calculation of the lithium valence Compton profiles. The easiest way to include temperature effects into bandstructure calculations is to utilize a temperature dependent local empirical pseudopotential.

4.4 Pseudopotential calculation

Pseudopotential based model calculations were successfully applied in the interpretation of lattice induced fine structures in the dynamic structure factor $S(\vec{q}, \omega)$ of simple metals like lithium, beryllium and aluminium [Schülke et al. 1986, Schülke et al. 1989, Schülke et al. 1993]. The temperature dependence of the crystal potential can be considered within these calculations, if the pseudopotential coefficients are weighted by a Debye-Waller factor. This method is routinely used if temperature effects have to be included in band calculations to determine semiconductor band gaps [Keffer et al. 1968, Zollner et al. 1991]. Furthermore, the temperature dependence of the one-peak one-shoulder structure appearing in the dynamic structure factor of aluminium was properly described by a temperature dependent empirical local pseudopotential [Sternemann et al. 1998]. In what follows, the pseudopotential scheme utilized to describe the temperature influence on the lithium Compton profiles is presented and then the results of the calculations are compared to the experimental findings.

4.4.1 Pseudopotential scheme

The valence Compton profile is directly related to the electron momentum density given in Eq. (1.42). The plane wave expansion coefficients $\alpha_\nu(\vec{k} + \vec{g})$ of Eq. (1.38) can be estimated utilizing Schrödinger's equation

$$\left(-\frac{\hbar^2}{2m} \vec{\nabla}^2 + V_{\text{Pseudo}}(\vec{r}) \right) \Phi_{\nu, \vec{k}}(\vec{r}) = E_{\nu, \vec{k}} \Phi_{\nu, \vec{k}}(\vec{r}) \quad (4.14)$$

which relates the energy eigenvalues $E_{\nu, \vec{k}}$ with bandindex ν to the Fourier components of the crystal potential $V_{\vec{g}}$ by solving the eigenwert problem

$$\left(\frac{1}{2}(\vec{k} + \vec{g})^2 - E(\vec{k}) \right) \alpha_\nu(\vec{k} + \vec{g}) - \sum_{\vec{g}'} V_{\vec{g}-\vec{g}'} \alpha_\nu(\vec{k} + \vec{g}') = 0. \quad (4.15)$$

The Fourier expansion of the pseudopotential $V_{\text{Pseudo}}(\vec{r})$ and the Bloch functions $\Phi_{\nu, \vec{k}}(\vec{r})$ are given by

$$V_{\text{Pseudo}}(\vec{r}) = \sum_{\vec{g}} V_{\vec{g}} e^{i\vec{g}\cdot\vec{r}} \quad (4.16)$$

$$\Phi_{\nu, \vec{k}}(\vec{r}) = \sum_{\vec{g}} \alpha_\nu(\vec{k} + \vec{g}) e^{i(\vec{k} + \vec{g})\cdot\vec{r}}. \quad (4.17)$$

Within this type of calculation the number of reciprocal lattice vectors \vec{g} and potential coefficients $V_{\vec{g}}$ taken into account to solve the eigenwert problem numerically has to be limited. Nevertheless, calculations of the aluminium Fermi energy can be performed using at least fifteen reciprocal lattice vectors with its two corresponding pseudopotential coefficients, namely V_{200} and V_{111} , [Harrison 1960] and even within the two-band model, where only \vec{g} , $-\vec{g}$ and $\vec{0}$ are considered, fine structures in the dynamic structure factor of lithium and beryllium could be assigned to zone-boundary collective states [Schülke et al. 1986, Schülke et al. 1989].

4.4.2 Temperature dependent pseudopotential calculation

The empirical local pseudopotential coefficients $V_{\vec{g}}$ are obtained by fitting the calculated directional Compton profile differences to the experimental directional Compton profile differences taken from the lithium Compton profile measurement performed at room temperature by Schülke [Schülke et al. 1996]. It is sufficient to use only the pseudopotential coefficients of the $\langle 110 \rangle$ and the $\langle 200 \rangle$ type to fit the Compton profile differences properly with $V_{110}(T = 295\text{K}) = 0.1$ a.u. and $V_{200}(T = 295\text{K}) = 0.02$ a.u. The temperature influence on the crystal potential is now accounted for by multiplying the pseudopotential coefficients with the corresponding Debye-Waller factor, making use of

$$V(\vec{g}, T) = V(\vec{g}, T = 0\text{K}) \exp\left(-\frac{B(T)|\vec{g}|^2}{16\pi^2}\right) \quad (4.18)$$

with the Debye parameter $B(T)$ derived from results of recent phonon density of states measurements [Peng et al. 1996]. $B(T)$, including the zero-point energy parameter B_0 and the thermal Debye parameter B_T , is directly related to the mean square of the vibrational atomic displacement $\langle u^2 \rangle$, describing the thermal disorder of the system, via

$$B(T) = B_0 + B_T = \frac{8\pi^2}{3} \langle u^2 \rangle . \quad (4.19)$$

The introduction of the Debye-Waller factor can be considered as taking into account the reduction of the amplitude of the Bloch wave reflected by the corresponding Bragg plane. The pseudopotential coefficients for $T = 95$ K are determined using Eq. (4.18) and are shown within Tab. 4.2 along with the other parameters used in the calculation.

The valence Compton profiles for $\vec{q} \parallel [110]$ obtained from the pseudopotential calculation have to be corrected with respect to electron-electron correlation since directional differences were fitted, in which the isotropic part of the

T [K]	l [Å]	V_{110} [a.u.]	V_{200} [a.u.]	B [Å ²]	p_F [a.u.]
295 K	3.5104	0.100	0.020	4.842	0.5876
95 K	3.4848	0.114	0.026	1.560	0.5919

Table 4.2: Temperature dependence of the model parameters used in the pseudopotential calculation.

electron-electron correlation contribution cancels out. The correlation correction is performed using the $n(k)$ model (see Eq. (4.11)) by calculating the difference of the jellium valence Compton profiles determined for $z_F = 1$ and $z_F(T = 295\text{K}) = 0.699$ ($z_F(T = 95\text{K}) = 0.701$), respectively. The obtained differences are close to the Lam-Platzman correction used within the LDA scheme and are added to the corresponding calculated valence Compton profiles. This isotropic correction is justified since the influence of the lattice on z_F is found to be small [Schülke 1999, Eguluz et al. 2000]. Finally, the profiles are convoluted with a Gaussian of 0.1 a.u. FWHM to simulate the momentum space resolution of the experiment. As for the experimental differences, the theoretically determined differences $J(p_z, T = 95\text{K}) - J(p_z, T = 295\text{K})$ are given in percent of the value of the calculated pseudopotential valence Compton profile for 95 K at $p_z = 0$ a.u. The result of the calculation is plotted as a solid line in Fig. 4.14 compared with the experimental findings.

A good overall agreement is obtained between the experimental findings and the theoretical computations, in which both the variation of the lattice constant and the change of the crystal potential with temperature is considered. Especially the contributions of the temperature effect at $p_z > p_F$ are nicely reproduced. These are attributed to the temperature dependence of the Umklapp-processes. With increasing temperature electron momentum density is transferred back into the primary Fermi sphere of the extended zone scheme which reduces the delocalization of the valence Compton profile in momentum space. The values given by the chi-square test are $\chi^2 = 0.89$ (first measurement) and $\chi^2 = 1.21$ (second measurement).

A second pseudopotential calculation is performed utilizing the room temperature pseudopotential coefficients for both temperatures and varying only the lattice constant. This allows to separate the temperature effect originating from the change of the crystal potential due to thermal disorder from the one attributed to the lattice expansion. The result is shown as a dashed line in Fig. 4.14 and is close to the jellium result presented in section 4.3. The corresponding values of $\chi^2 = 2.2$ (first measurement) and $\chi^2 = 1.87$ (second measurement) are in good agreement with the ones obtained from the jellium computation. The temperature influence due to the change of the crystal potential is determined by calculating the difference be-

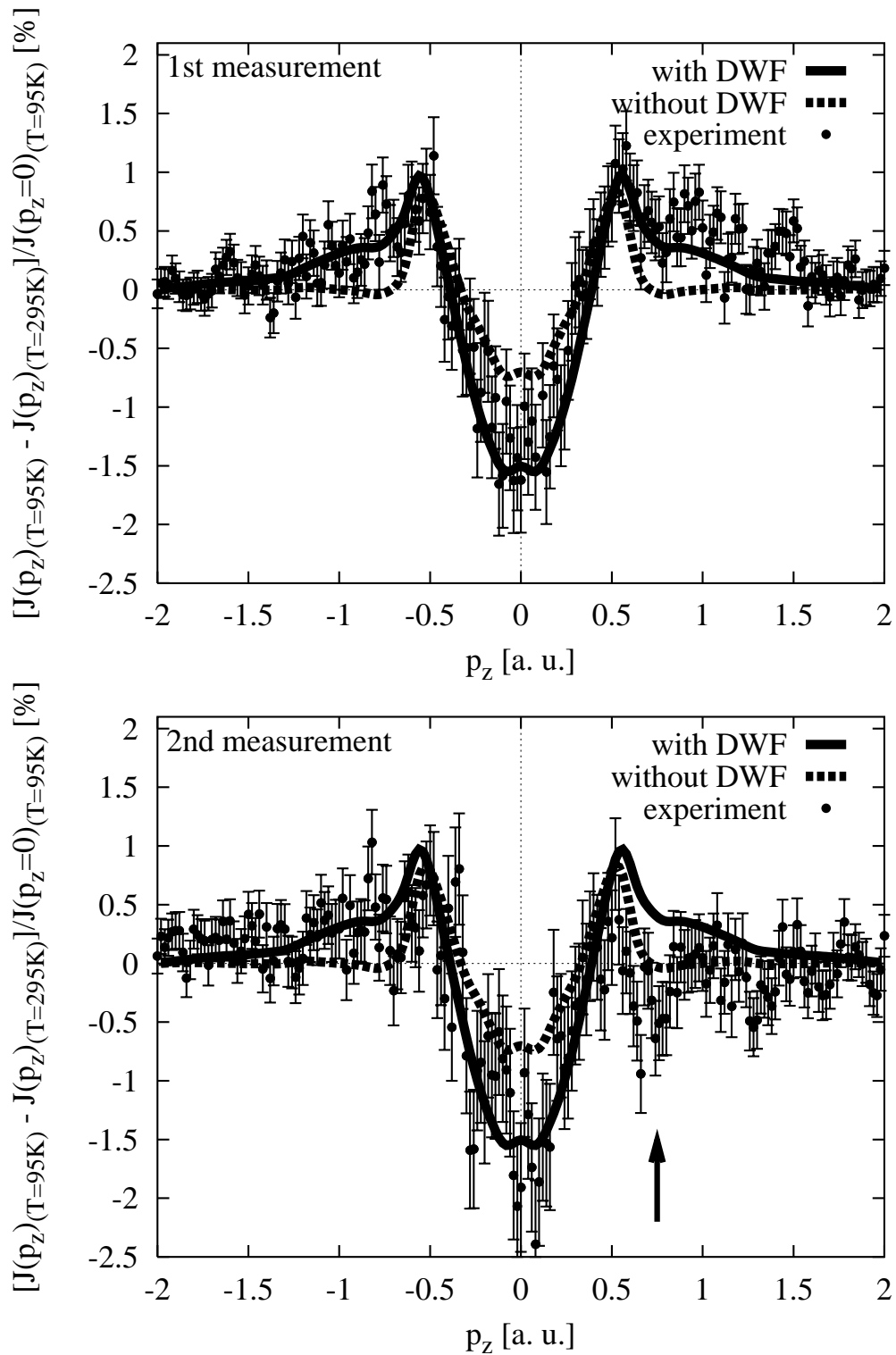


Figure 4.14: Experimentally obtained valence Compton profile differences $J(p_z, T = 95\text{K}) - J(p_z, T = 295\text{K})$ compared to the pseudopotential calculations with (solid line) and without (dashed line) consideration of the temperature effect on the crystal potential via the Debye-Waller factor (DWF).

tween the pseudopotential calculation with temperature dependent Debye-Waller factor (with DWF) and the pseudopotential calculation using a constant Debye-Waller factor (without DWF). This difference is presented in Fig. 4.15 compared to the difference of the symmetrized experimentally observed temperature effect (first measurement) and the jellium calculation.

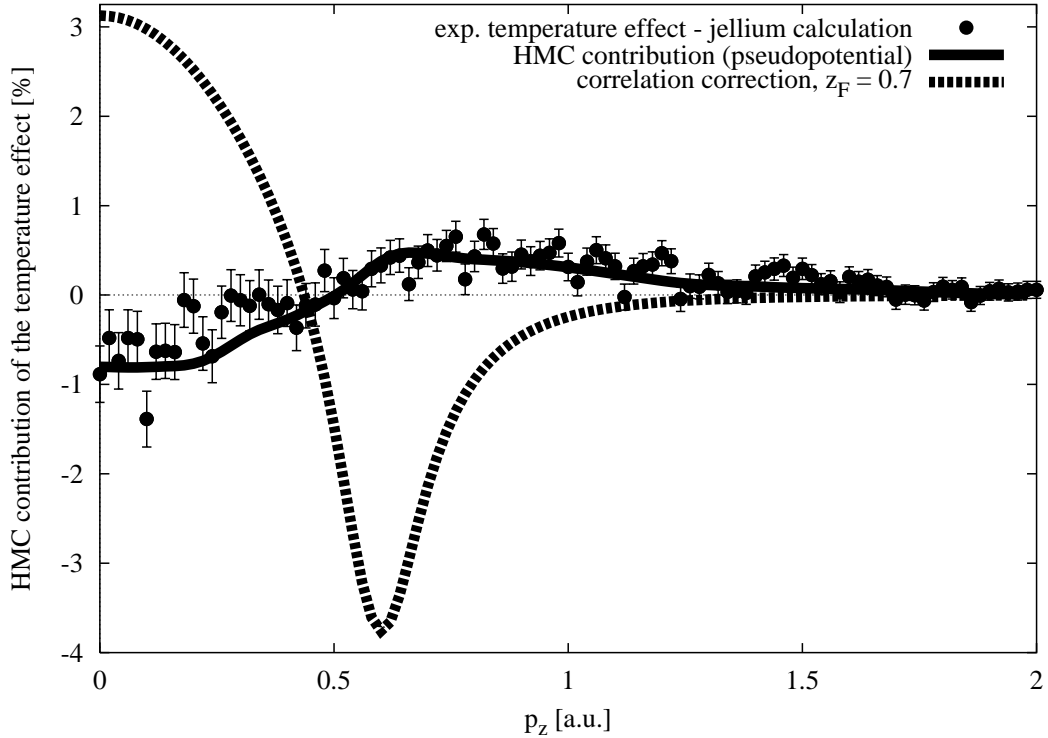


Figure 4.15: Temperature dependence of the contribution of the higher momentum components (HMC's) to the valence Compton profile. The dashed line denotes the correlation correction for $z_F = 0.7$ which is similar to the Lam-Platzman correction and demonstrates the magnitude of the thermal disorder effect.

Thus a significant contribution to the total temperature effect could be assigned to the decrease of the higher momentum component contribution to the valence Compton profile with increasing temperature. The order of magnitude of the temperature effect related to thermal disorder is illustrated in Fig. 4.15 by comparing the contribution due to Umklapp-processes with the correlation correction of the valence Compton profile for $z_F = 0.7$, which is close to the corresponding Lam-Platzman correction. The influence of the zero-point lattice motion on the valence Compton profile is not accessible within the limits of the present experiment. Nevertheless, it should also reduce the contribution of the higher momentum components to the valence Compton profile and is usually neglected in standard

Compton profile calculations. Since thermal disorder causes a narrowing of the valence Compton profile, the experimental findings suggest, that the consideration of thermal disorder within bandstructure calculations of the valence Compton profiles would enlarge the discrepancy between experiment and theory.

4.5 Summary

Measurements of temperature dependent Compton profiles of lithium for $\vec{q}||[110]$ have shown a principal temperature effect which is caused by the variation of the lattice constant. The valence Compton profile becomes narrower with increasing temperature. This temperature effect is in agreement with the results found for aluminium valence Compton profiles [Sternemann et al. 2000 (c)]. In Compton profile measurements on metallic sodium as a function of pressure a similar effect was found and interpreted in terms of the jellium model, where the main pressure effect is also attributed to the variation of the Fermi momentum with changing lattice constant [Hämäläinen et al. 2000]. Beyond this, a significant contribution of the temperature influence on the crystal potential due to thermal disorder is found and well described utilizing an empirical pseudopotential scheme, where the temperature influence is simulated by the use of Debye-Waller factors on the pseudopotential coefficients. With increasing temperature electron momentum density is transferred back to the primary Fermi sphere of the extended zone scheme and the valence Compton profile becomes more and more free electron like. This interpretation is in agreement with the experimental results of positron annihilation measurements on potassium showing that the contributions of higher momentum components decrease with increasing temperature [Manuel et al. 1993]. Finally, the measured temperature effect differs in sign and amplitude from the results of the thermal disorder model presented by Dugdale and Jarlborg [Dugdale and Jarlborg 1998]. Thus it can be ruled out that the discrepancy between experiment and commonly used band structure calculations in the case of lithium Compton profiles is due to thermal disorder. The comparison of the experimental results with the computations shows that the disagreement will be enlarged, if thermal disorder is considered within the computations, which is most important, since the effect of the zero-point lattice motion is not negligible for light elements like lithium, $B_0 = 0.96 \text{ \AA}^2$ [International Tables for X-ray Crystallography 1968], and usually is not considered in any bandstructure calculation.

Conclusion

The decisive argument to study the Compton profile of lithium with very high resolution at low incident energies and as a function of temperature at high incident energies was to clarify some aspects of the widely discussed discrepancy between experiment and theory and thus to bring some light into the unsatisfactory situation with the valence Compton profile of lithium.

Measurements of the lithium Compton profiles have been performed with an incident energy around 9 keV and a momentum space resolution of $\Delta p_z = 0.022$ a.u. to investigate the effect of final state interaction and thus to test the validity of the impulse approximation in interpreting the valence Compton profile. Furthermore, the temperature dependence of the Compton profile of lithium has been studied at 30 keV with $\Delta p_z = 0.10$ a.u. momentum space resolution. Both experiments were discussed with respect to the above mentioned discrepancy.

It was shown that the predicted sharp features at the Fermi momentum, which should be resolved with the highly improved momentum space resolution obtained for the low energy experiment, are still smeared out and that the valence Compton profile exhibits a clear asymmetry. This experimentally found asymmetry agrees well with the predictions of the first and the second order vertex correction to the fully self-energy corrected proper polarization function which is a direct evidence of the particle-hole interaction. The main part of the additional smearing of the Compton profile beyond experimental resolution was attributed to the convolution of the Compton profile with the spectral density function of the excited particle. This final state effect causes an intrinsic resolution limit for Compton measurements performed at low incident energies. It is emphasized that the smearing of the valence Compton profile due to the spectral density function becomes more and more negligible with increasing incident energy so that the highly demanded improvement of the momentum space resolution beyond 0.05 a.u. requires incident photon energies larger than 30 keV. The application of the impulse approximation is definitely not justified for this high resolution experiment performed at low incident energies in the sense that it is necessary to consider final state effects in interpreting the experimental results. Furthermore, the discussion of the experimental results utilizing the reciprocal form factor has shown that the discrepancy between experiment and theory still remains. Due to this fact the discrepancy may be attributed to the inadequate treatment of electron-electron correlation effects,

since the reciprocal form factor determined at lattice translation vectors is hardly influenced by lattice effects. It can be ruled out that the discrepancy can be explained by the final state interaction, since the influence of the spectral density function of the excited particle on the Compton profile vanishes with increasing incident energy.

Furthermore, the lithium Compton profile has been measured as a function of temperature at 30 keV incident energy, where the impulse approximation can be applied to valence electrons. The valence Compton profile gets narrower with increasing temperature and the difference of the valence Compton profiles measured at 95 K and 295 K exhibits significant contributions for momenta larger than the Fermi momentum. No temperature dependence of the core Compton profile could be detected within the limits of the experiment. This temperature effect was confronted with a temperature dependent jellium calculation and computations using an empirical local pseudopotential, where the influence of thermal disorder is considered via the Debye-Waller factor. By comparing the calculations with the experiment the temperature effect is attributed to the expansion of the lattice constant and to the diminishing of the higher momentum component contribution to the Compton profile with increasing temperature. The measured temperature effect is opposite in sign and different in amplitude compared to the predictions of the LMTO calculations [Dugdale and Jarlborg 1998] so that it can be ruled out that the discrepancy between experiment and theory is due to thermal disorder. The experimental results suggest that the discrepancy will be enlarged if thermal disorder is included into the bandstructure calculations of the lithium valence Compton profile.

The presented results don't solve the lithium puzzle but give some important indications which way to go to explain the discrepancy between experiment and theory. The effect of temperature and of the final state interaction cannot account for it and the high resolution measurement suggests that the treatment of electron-electron correlation in the calculation schemes has to be reconsidered. New theoretical approaches may be promising [Baruah et al. 1999, Barbiellini 2000]. Furthermore, a study of the predicted sharp features appearing at the Fermi break would be useful, when measured with a momentum resolution around 0.03 a.u. and at high incident energies to exclude the influence of the final state interaction. A study on beryllium exhibits similar conclusions concerning the electron-electron correlation and the influence of the final state interaction [Huotari et al. 2000] and results for sodium are highly requested [Hämäläinen 2000]. In contrast, aluminium valence Compton profiles are in good overall agreement with the present theories [Suortti et al. 2000].

With the use of synchrotron radiation sources Compton scattering became a powerful tool to investigate very small changes of the electron momentum density,

which incited a fruitful interplay between experimentalists and theoreticians. With this progress on the experimental side temperature [Sternemann et al. 2000 (b)] and pressure [Hämäläinen et al. 2000] effects are accessible. Even small signatures of the Fermi surface can be resolved as shown in the case of beryllium [Huotari et al. 2000] and Compton scattering is exposed to be a valuable probe of many-particle calculations if studied under experimental conditions where the impulse approximation is not valid [Sternemann et al. 2000]. However, in spite of this exciting progress in Compton scattering on the experimental and the theoretical side it is still critical from an experimental point of view to correct the data for multiple scattering, to have a reliable monitorization of the incident photon beam, to account for the background and to overcome the problems connected with the detector dead time. In interpreting ground state properties the failure of the impulse approximation and the treatment of electron-electron correlation turn out to be serious problems from a theoretical point of view.

Appendix A

The fully dressed Green's function

Within Appendix A the relation between the free-particle Green's function $G^0(\vec{p}, \epsilon)$ and the fully dressed Green's function $G^{\text{SE}}(\vec{p}, \epsilon)$ which includes the total self-energy contribution to the free-particle polarization function is discussed.

The correction of the free-particle polarization function $\chi_{\text{sc}}^0(\vec{q}, \omega)$ by the self-energy contributions is presented in Fig. A.1, which shows the first terms of the self-energy series expanded in terms of the Coulomb potential screened by the Lindhard dielectric function. The self-energy corrected polarizability is then determined by the calculation of the whole Feynman diagram series. The thin solid lines denote the free-particle Green's functions of the hole and the particle, respectively. The interaction term $I_{\text{sc}}^C(\vec{p}, \epsilon, \vec{p}', \epsilon')$ is plotted as wiggly line and the resulting fully dressed Green's functions are given by the bold lines.

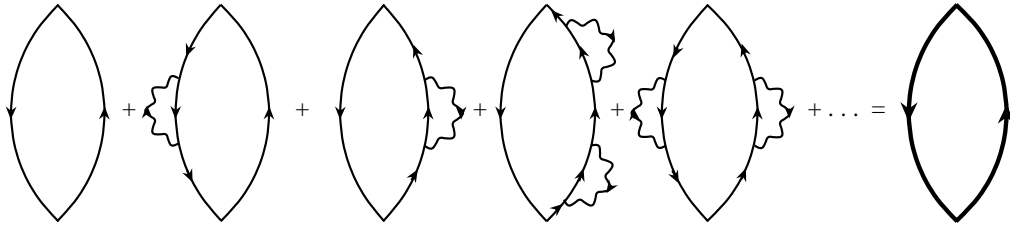


Figure A.1: Self-energy series expanded in terms of the screened Coulomb interaction (wiggly line).

The calculation of the first diagram yields

$$\chi_{\text{sc}}^0(\vec{q}, \omega) = 2 \int \frac{d\epsilon}{(2\pi i)} \int \frac{d\vec{p}}{(2\pi)^3} G^0(\vec{p}, \epsilon) G^0(\vec{p} + \vec{q}, \epsilon + \omega), \quad (\text{A.1})$$

the proper polarization function of a free particle. The first order self-energy correction is performed by calculating the diagrams (2) and (3) of Fig. A.1, which results in

$$\begin{aligned} \chi_{\text{sc}}^{\text{SE}_1}(\vec{q}, \omega) &= 2 \int \frac{d\epsilon}{(2\pi i)} \int \frac{d\vec{p}}{(2\pi)^3} G^0(\vec{p}, \epsilon) G^0(\vec{p} + \vec{q}, \epsilon + \omega) \\ &\times (\Sigma(\vec{p}, \epsilon) G^0(\vec{p}, \epsilon) + \Sigma(\vec{p} + \vec{q}, \epsilon + \omega) G^0(\vec{p} + \vec{q}, \epsilon + \omega)) \end{aligned} \quad (\text{A.2})$$

with the self-energy of the hole $\Sigma(\vec{p}, \epsilon)$ and the particle $\Sigma(\vec{p} + \vec{q}, \epsilon + \omega)$, respectively:

$$\Sigma(\vec{p}, \epsilon) = - \int \frac{d\epsilon'}{(2\pi i)} \int \frac{d\vec{p}'}{(2\pi)^3} \frac{v(\vec{p}' - \vec{p})}{\epsilon^{\text{RPA}}(\vec{p}' - \vec{p}, \epsilon' - \epsilon)} G^0(\vec{p}', \epsilon') \quad (\text{A.3})$$

$$\begin{aligned} \Sigma(\vec{p} + \vec{q}, \epsilon + \omega) &= - \int \frac{d\epsilon'}{(2\pi i)} \int \frac{d\vec{p}'}{(2\pi)^3} \frac{v(\vec{p}' - \vec{p})}{\epsilon^{\text{RPA}}(\vec{p}' - \vec{p}, \epsilon' - \epsilon)} \\ &\times G^0(\vec{p}' + \vec{q}, \epsilon' + \omega). \end{aligned} \quad (\text{A.4})$$

Following Eqs. (A.1) and (A.2) the total self-energy series, $\chi_{\text{sc}}^0 + \chi_{\text{sc}}^{\text{SE}_1} + \text{terms of higher order in the screened Coulomb potential}$, can be expressed utilizing the fully dressed Green's function $G^{\text{SE}}(\vec{p}, \epsilon)$ in Eq. (A.1) instead of $G^0(\vec{p}, \epsilon)$, where $G^{\text{SE}}(\vec{p}, \epsilon)$ is determined by the self-consistent Dyson equation [Holas et al. 1979]

$$G^{\text{SE}}(\vec{p}, \epsilon) = G^0(\vec{p}, \epsilon) + G^0(\vec{p}, \epsilon) \Sigma(\vec{p}, \epsilon) G^{\text{SE}}(\vec{p}, \epsilon). \quad (\text{A.5})$$

The recursive insertion of this expression into Eq. (A.1) describes the series presented in Fig. A.1. The solution of the Dyson equation yields

$$\begin{aligned} G^{\text{SE}}(\vec{p}, \epsilon) &= \frac{G^0(\vec{p}, \epsilon)}{1 - \Sigma(\vec{p}, \epsilon) G^0(\vec{p}, \epsilon)} \\ &= G^0(\vec{p}, \epsilon + \Sigma(\vec{p}, \epsilon)). \end{aligned} \quad (\text{A.6})$$

Thus the self-energy correction can fully be taken into account by Eq. (A.1), if the free-particle Green's function is replaced by the fully dressed Green's function including the self-energy:

$$\begin{aligned} \chi_{\text{sc}}^{\text{SE}}(\vec{q}, \omega) &= 2 \int \frac{d\epsilon}{(2\pi i)} \int \frac{d\vec{p}}{(2\pi)^3} G^0(\vec{p}, \epsilon + \Sigma(\vec{p}, \epsilon)) \\ &\times G^0(\vec{p} + \vec{q}, \epsilon + \omega + \Sigma(\vec{p} + \vec{q}, \epsilon + \omega)) \\ &= 2 \int \frac{d\epsilon}{(2\pi i)} \int \frac{d\vec{p}}{(2\pi)^3} G^{\text{SE}}(\vec{p}, \epsilon) G^{\text{SE}}(\vec{p} + \vec{q}, \epsilon + \omega). \end{aligned} \quad (\text{A.7})$$

The calculation of the self-energy in GW approximation [Hedin 1965] can be extended by the so-called cumulant expansion since therein a diagrammatic expansion in the Green's function and not in the self-energy is performed [Aryasetiawan et al. 1996]. Both the GW calculation and the cumulant expansion can also be performed self-consistently utilizing a variable Green's function [Holm and Aryasetiawan 1997]. Concerning the spectral density function these extended calculation schemes hardly influence the results obtained for the quasi-particle peak compared to a GW computation but give rise to a more realistic description of its satellite structure.

Appendix B

Local field approximation

In the local field approximation the irreducible interaction term is represented by $I(\vec{p}, \epsilon, \vec{p}', \epsilon'; \vec{q}, \omega) = 2I(q, \omega) = -2v(q)g(q, \omega)$, where the bare Coulomb potential is screened by the local field $g(q, \omega)$. Then Eq. (2.12) can be expressed in terms of the free-particle Green's function

$$\begin{aligned}
 \chi_{\text{sc}}^{\text{LF}}(\vec{q}, \omega) &= 2 \int \frac{d\epsilon}{(2\pi i)} \int \frac{d\vec{p}}{(2\pi)^3} G^0(\vec{p}, \epsilon) G^0(\vec{p} + \vec{q}, \epsilon + \omega) \\
 &\times \left[1 + 2 \int \frac{d\epsilon'}{(2\pi i)} \int \frac{d\vec{p}'}{(2\pi)^3} I(q, \omega) G^0(\vec{p}', \epsilon') G^0(\vec{p}' + \vec{q}, \epsilon' + \omega) \right. \\
 &\quad + 2 \int \frac{d\epsilon'}{(2\pi i)} \int \frac{d\vec{p}'}{(2\pi)^3} I(q, \omega) G^0(\vec{p}', \epsilon') G^0(\vec{p}' + \vec{q}, \epsilon' + \omega) \\
 &\quad \times 2 \int \frac{d\epsilon''}{(2\pi i)} \int \frac{d\vec{p}''}{(2\pi)^3} I(q, \omega) G^0(\vec{p}'', \epsilon'') G^0(\vec{p}'' + \vec{q}, \epsilon'' + \omega) \\
 &\quad \left. + \dots \right]. \tag{B.1}
 \end{aligned}$$

With the definition of the free-particle polarization function $\chi_{\text{sc}}^0(\vec{q}, \omega)$ from Eq. (2.23) the proper polarization function yields

$$\chi_{\text{sc}}^{\text{LF}}(\vec{q}, \omega) = \chi_{\text{sc}}^0(\vec{q}, \omega)(1 + I(q, \omega)\chi_{\text{sc}}^0(\vec{q}, \omega) + I(q, \omega)^2\chi_{\text{sc}}^0(\vec{q}, \omega)^2 + \dots), \tag{B.2}$$

which can be identified as a geometric series. The geometric series is summed up to

$$\chi_{\text{sc}}^{\text{LF}}(\vec{q}, \omega) = \frac{\chi_{\text{sc}}^0(\vec{q}, \omega)}{1 + v(q)g(q, \omega)\chi_{\text{sc}}^0(\vec{q}, \omega)}. \tag{B.3}$$

Bibliography

- [Anastassopoulos et al. 1998] D. L. Anastassopoulos, G. D. Priftis, C. Toprakcioglu, and A. A. Vradis, *Phys. Rev. Lett* **81**, 830 (1998).
- [Aryasetiawan et al. 1996] F. Aryasetiawan, L. Hedin, and K. Karlsson, *Phys. Rev. Lett.* **77**, 2268 (1996).
- [Asthalter and Weyrich 1997] T. Asthalter and W. Weyrich, *Ber. Bunsenges. Phys. Chem.* **101**, 11 (1997).
- [Awa et al. 1981] K. Awa, H. Yasuhara, and T. Asahi, *Solid State Commun.* **38**, 1285 (1981).
- [Bansil 1993] A. Bansil, *Z. Naturforschung A* **48**, 165 (1993).
- [Bansil et al. 1998] A. Bansil, S. Kaprzyk, A. Andrejczuk, L. Dobrzyński, J. Kwiatkowska, F. Maniawski, and E. Żukowski, *Phys. Rev. B* **57**, 314 (1998).
- [Barbiellini 2000] B. Barbiellini, *J. Phys. Chem. Solids* **61**, 341 (2000).
- [Baruah et al. 1999] T. Baruah, R. R. Zope, and A. Kshirsagar, *Phys. Rev. B* **60**, 10770 (1999).
- [Bauer and Schneider 1985] G. E. W. Bauer and J. R. Schneider, *Phys. Rev. B* **31**, 681 (1985).
- [Benesch et al. 1971] R. Benesch, S. R. Singh, and V. H. Smith Jr., *Chem. Phys. Lett.* **10**, 151 (1971).
- [Benesch and Smith 1973] R. Benesch and V. H. Smith Jr., *Wave Mechanics - The First Fifty Years*, edited by W. C. Price, S. S. Chissik, and T. Ravensdale, p. 203 (Butterworths, London, 1973).
- [Berggren et al. 1977] K.-F. Berggren, S. Manninen, T. Paakkari, O. Aikala, and K. Mansikka, *Compton Scattering*, edited by B. G. Williams, p. 139 (McGraw-Hill, New York, 1977).
- [Biggs et al. 1975] F. Biggs, L. B. Mendelsohn, J. B. Mann, *At. Data and Nucl. Data Tables* **16**, 201 (1975).

- [Blaas et al. 1995] C. Blaas, J. Redinger, S. Manninen, V. Honkimäki, K. Hämäläinen, and P. Suortti, *Phys. Rev. Lett.* **75**, 1984 (1995).
- [Blume 1985] M. Blume, *J. Appl. Phys.* **57**, 3615 (1985).
- [Borstel 1985] G. Borstel, *Appl. Phys. A* **38**, 193 (1985).
- [Cardona and Ley 1978] M. Cardona and L. Ley, *X-Ray Data Booklet*, edited by D. Vaughan (Lawrence Berkeley Laboratory, University of California, Berkeley, California, 1986).
- [Cardwell and Cooper 1989] D. A. Cardwell and M. J. Cooper, *J. Phys. Condens. Matter* **1**, 9357 (1989).
- [Compton 1923] A. H. Compton, *Phys. Rev.* **21**, 207, 483 (1923).
- [Cooper et al. 1965] M. J. Cooper, J. A. Leake, and R. J. Weiss, *Phil. Mag.* **12**, 797 (1965).
- [Cooper 1985] M. J. Cooper, *Rep. Prog. Phys.* **48**, 415 (1985).
- [Cooper and Duffy 2000] M. J. Cooper and J. A. Duffy, *J. Phys. Chem. Solids* **61**, 345 (2000).
- [Debye 1923] P. Debye, *Phys. Zeit.* **24**, 165 (1923).
- [Dobrzyński 2000] L. Dobrzyński, *J. Phys. Condens. Matter* **12**, 87 (2000).
- [Duffy et al. 2000] J. A. Duffy, S. B. Dugdale, J. E. McCarthy, M. A. Alam, M. J. Cooper, S. B. Palmer, and T. Jarlborg, *Phys. Rev. B* **61**, 14331 (2000).
- [Dugdale and Jarlborg 1998] S. B. Dugdale and T. Jarlborg, *Solid State Commun.* **105**, 283 (1998).
- [Dugdale et al. 2000] S. B. Dugdale, H. M. Fretwell, K. J. Chen, Y. Tanaka, A. Shukla, T. Buslaps, Ch. Bellin, M. A. Alam, A. A. Manuel, P. Suortti, and N. Shiotani, *J. Phys. Chem. Solids* **61**, 361 (2000).
- [DuMond 1929] J. W. M. DuMond, *Phys. Rev.* **33**, 643 (1929).
- [DuMond and Kirkpatrick 1931] J. W. M. DuMond and H. A. Kirkpatrick, *Phys. Rev.* **37**, 136 (1931), *Phys. Rev.* **38**, 1094 (1931).
- [DuMond and Hoyt 1931] J. W. M. DuMond and A. Hoyt, *Phys. Rev.* **37**, 1443 (1931).

- [DuMond et al. 1932] J. W. M. DuMond, H. A. Kirkpatrick, and L. Alden, *Phys. Rev.* **40**, 165 (1932).
- [Eguiluz et al. 2000] A. G. Eguiluz, W. Ku, and J. M. Sullivan, *J. Phys. Chem. Solids* **61**, 383 (2000).
- [Eisenberger and Platzman 1970] P. Eisenberger and P. M. Platzman, *Phys. Rev. A* **2**, 415 (1970).
- [Eisenmann and Schäfer 1986] B. Eisenmann and H. Schäfer, *Landolt Börnstein - Numerical Data and Functional Relationships in Science and Technology*, Vol. 14 a, edited by K.-H. Hellwege and A. M. Hellwege, p. 398 (Springer-Verlag, Berlin, Heidelberg, New York, London, Paris, Tokyo, 1986).
- [Erola et al. 1990] E. Erola, V. Eteläniemi, P. Suortti, P. Pattison, and W. Thomlinson, *J. Appl. Cryst.* **23**, 35 (1990).
- [Felsteiner and Schülke 1997] J. Felsteiner and W. Schülke, *Nucl. Instrum. and Methods B* **132**, 1 (1997).
- [Filippi and Ceperley 1999] C. Filippi and D. M. Ceperley, *Phys. Rev. B* **59**, 7907 (1999) and references therein.
- [Green et al. 1985] F. Green, D. Neilson, and J. Szymański, *Phys. Rev. B* **31**, 2779, 2796 (1985).
- [Green et al. 1987] F. Green, D. Neilson, and J. Szymański, *Phys. Rev. B* **35**, 124 (1987).
- [Hämäläinen et al. 1996] K. Hämäläinen, S. Manninen, C.-C. Kao, W. A. Caliebe, J. B. Hastings, A. Bansil, S. Kaprzyk, and P. M. Platzman, *Phys. Rev. B* **54**, 5453 (1996).
- [Hämäläinen et al. 2000] K. Hämäläinen, S. Huotari, J. Laukkanen, A. Soininen, S. Manninen, C.-C. Kao, T. Buslaps, and M. Mezouar, *Phys. Rev. B* **62**, 735 (2000).
- [Hämäläinen 2000] K. Hämäläinen, private communication.
- [Hansen 1980] N. K. Hansen, *Reconstruction of the electron momentum distribution from a set of directional Compton profiles*, Report HMI B 342 (Hahn-Meitner Institut, Berlin, 1980).
- [Harrison 1960] W. A. Harrison, *Phys. Rev.* **118**, 1182 (1960).
- [Hedin 1965] L. Hedin, *Phys. Rev.* **139**, A 796 (1965).

- [Holas et al. 1979] A. Holas, P. K. Aravind, and K. S. Singwi, Phys. Rev. B **20**, 4912 (1979).
- [Holm and Ribberfors 1989] P. Holm and R. Ribberfors, Phys. Rev. A **40**, 6251 (1989) and references therein.
- [Holm and Aryasetiawan 1997] B. Holm and F. Aryasetiawan, Phys. Rev. B **56**, 12825 (1997).
- [Holt et al. 1978] R. S. Holt, M. J. Cooper, and K. R. Lea, J. Phys. E **11**, 68 (1978)
- [Holt et al. 1979] R. S. Holt, J. L. Dubard, M. J. Cooper, T. Paakkari, and S. Manninen, Philos. Mag. B **39**, 541 (1979)
- [Huotari et al. 2000] S. Huotari, K. Hämäläinen, S. Manninen, S. Kaprzyk, A. Bansil, W. A. Caliebe, T. Buslaps, V. Honkimäki, and P. Suortti, Phys. Rev. B **62**, 7956 (2000).
- [International Tables for X-ray Crystallography 1968] *International Tables for X-ray Crystallography*, Vol. 3, 234 (Kynoch Press, Birmingham, 1968).
- [Isaacs et al. 1999] E. D. Isaacs, A. Shukla, P. M. Platzman, D. R. Hamann, B. Barbiellini, and C. A. Tulk, Phys. Rev. Lett. **82**, 600 (1999).
- [Issolah et al. 1988] A. Issolah, B. Levy, A. Beswick, and G. Loupiau, Phys. Rev. A **38**, 4509 (1988).
- [Keffer et al. 1968] C. Keffer, T. M. Hayes, and A. Bienenstock, Phys. Rev. Lett. **21**, 1676 (1968).
- [Kappeler 1936] H. Kappeler, Ann. der Physik **27**, 129 (1936).
- [Králik et al. 1998] B. Králik, P. Delaney, and S. G. Louie, Phys. Rev. Lett. **80**, 4253 (1998).
- [Kubo 1997] Y. Kubo, J. Phys. Soc. Jpn. **66**, 2236 (1997).
- [Lam and Platzman 1974] L. Lam and P. M. Platzman, Phys. Rev. B **9**, 5122, 5128 (1974).
- [Lindhard 1954] K. Dan. Vidensk. Selsk. Mat.-Fys. Medd. **28**, 8 (1954).
- [Löwdin 1955] P.-O. Löwdin, Phys. Rev. **97**, 1474 (1955).
- [Loupiau et al. 1980] G. Loupiau, J. Petiau, A. Issolah, and M. Schneider, Phys. Stat. Sol. B **102**, 79 (1980).

- [Loupias et al. 1984] G. Loupias, J. Chomilier, and D. Guérard, *J. Phys. Lett.* **45**, L301 (1984).
- [Lundqvist 1967] B. I. Lundqvist, *Phys. kondens. Materie* **6**, 193, 206 (1967).
- [Lundqvist and Lydén 1971] B. I. Lundqvist and C. Lydén, *Phys. Rev. B* **4**, 3360 (1971).
- [Mahan 1981] G. D. Mahan, *Many Particle Physics*, (Plenum Press, New York, 1981).
- [Manninen et al. 1996] S. Manninen, V. Honkimäki, K. Hämäläinen, J. Laukkanen, C. Blaas, J. Redinger, J. E. McCarthy, and P. Suortti, *Phys. Rev. B* **53**, 7714 (1996).
- [Manuel et al. 1993] A. A. Manuel, L. Oberli, A. K. Singh, T. Jarlborg, M. Peter, P. E. Mijnaerends, L. P. L. M. Rabou, T. Hyodo, and A. T. Stewart, *J. Phys. Condens. Matter* **5**, 8703 (1993).
- [Marangolo et al. 1999] M. Marangolo, Ch. Bellin, G. Loupias, S. Rabii, S. C. Erwin, and T. Buslaps, *Phys. Rev. B* **60**, 17084 (1999).
- [McMaster et al. 1970] W. H. McMaster, N. Kerr Del Grande, J. H. Mallet, and J. H. Hubbel, *Compilation of X-ray Cross Sections*, (Lawrence Radiation Laboratory, University of California, Livermore, California, 1970).
- [Ng and Dabrowski 1986] Tai Kai Ng and B. Dabrowski, *Phys. Rev. B* **33**, 5358 (1986).
- [Papanicolaou et al. 1991] N. I. Papanicolaou, N. C. Bacalis, and D. A. Papaconstantopoulos *Handbook of Calculated Electron Momentum Distributions, Compton Profiles, and X-ray Form Factors of Elemental Solids* (CRC Press, Boca Raton Ann Arbor Boston London, 1991)
- [Pattison et al. 1977] P. Pattison, W. Weyrich, and B. Williams, *Solid State Commun.* **21**, 967 (1977).
- [Pattison and Schneider 1978] P. Pattison and J. R. Schneider, *Solid State Commun.* **28**, 581 (1978).
- [Pattison et al. 1981] P. Pattison, N. K. Hansen and J. R. Schneider, *Chem. Phys.* **59**, 231 (1981).
- [Peng et al. 1996] L.-M. Peng, G. Ren, S. L. Dudarev, and M. J. Whelan, *Acta. Cryst. A* **52**, 456 (1996).

- [Pines and Nozières 1966] D. Pines and P. Nozières, *The Theory of Quantum Liquids* (Benjamin, New York, Amsterdam, 1966).
- [Platzman and Tzoar 1965] P. M. Platzman and N. Tzoar, Phys. Rev. **139**, A 410 (1965).
- [Ribberfors 1975] R. Ribberfors, Phys. Rev. B **12**, 2067, 3136 (1975).
- [Sakai 1996] N. Sakai, J. Appl. Cryst. **29**, 81 (1996).
- [Sakurai et al. 1995] Y. Sakurai, Y. Tanaka, A. Bansil, S. Kaprzyk, A. T. Stewart, Y. Nagashima, T. Hyodo, S. Nanao, H. Kawata, and N. Shiotani, Phys. Rev. Lett. **74**, 2252 (1995).
- [Schülke 1977] W. Schülke, Phys. Stat. Sol. **82**, 229 (1977).
- [Schülke and Nagasawa 1984] W. Schülke and H. Nagasawa, Nucl. Instrum. and Methods **222**, 203 (1984).
- [Schülke et al. 1986] W. Schülke, H. Nagasawa, S. Mourikis, and P. Lanzki, Phys. Rev. B **33**, 6744 (1986).
- [Schülke 1986] W. Schülke, Nucl. Instrum. and Methods A **246**, 491 (1986).
- [Schülke et al. 1989] W. Schülke, H. Nagasawa, S. Mourikis, and A. Kaprolat, Phys. Rev. B **40**, 12215 (1989).
- [Schülke et al. 1993] W. Schülke, H. Schulte-Schrepping, and J. R. Schmitz, Phys. Rev. B **47**, 12426 (1993).
- [Schülke et al. 1996] W. Schülke, G. Stutz, F. Wohlert, and A. Kaprolat, Phys. Rev. B **54**, 14381 (1996).
- [Schülke 1999] W. Schülke, J. Phys. Soc. Jpn. **68**, 2470 (1999).
- [Shukla et al. 1999] A. Shukla, B. Barbiellini, A. Erb, A. Manuel, T. Buslaps, V. Honkimäki, and P. Suortti, Phys. Rev. B **59**, 12127 (1999).
- [Singwi and Tosi 1981] K. S. Singwi and M. P. Tosi, *Solid State Physics*, edited by H. Ehrenreich, F. M. Seitz, and D. Turnbull **36**, p. 177 (Academic, New York, 1981).
- [Smith 1987] H. G. Smith, Phys. Rev. Lett. **58**, 1228 (1987).
- [Sternemann et al. 1998] C. Sternemann, A. Kaprolat, and W. Schülke, Phys. Rev. B **57**, 622 (1998).

- [Sternemann et al. 2000] C. Sternemann, K. Hämäläinen, A. Kaprolat, A. Soininen, G. Döring, C.-C. Kao, S. Manninen, and W. Schülke, Phys. Rev. B **62**, 7687 (2000).
- [Sternemann et al. 2000 (b)] C. Sternemann, G. Döring, C. Wittkop, W. Schülke, A. Shukla, T. Buslaps, and P. Suortti, J. Phys. Chem. Solids **61**, 379 (2000).
- [Sternemann et al. 2000 (c)] C. Sternemann, T. Buslaps, A. Shukla, P. Suortti, G. Döring, and W. Schülke, Phys. Rev. B **63**, 094301 (2001).
- [Stutz et al. 1999] G. Stutz, F. Wohlert, A. Kaprolat, W. Schülke, Y. Sakurai, Y. Tanaka, M. Ito, H. Kawata, N. Shiotani, S. Kaprzyk, and A. Bansil, Phys. Rev. B **60**, 7099 (1999).
- [Suortti et al. 1986] P. Suortti, P. Pattison, W. Weyrich, J. Appl. Cryst. **19**, 343 (1986).
- [Suortti et al. 1999] P. Suortti, T. Buslaps, P. Fajardo, V. Honkimäki, M. Kretschmer, U. Lienert, J. E. McCarthy, M. Renier, A. Shukla, Th. Tschentscher, and T. Meinander, J. of Synchrotron Rad. **6**, 69 (1999).
- [Suortti et al. 2000] P. Suortti, T. Buslaps, V. Honkimäki, C. Metz, A. Shukla, Th. Tschentscher, J. Kwiatkowska, F. Maniawski, A. Bansil, S. Kaprzyk, A. S. Kheifets, D. R. Lun, T. Sattler, J. R. Schneider and F. Bell, J. Phys. Chem. Solids **61**, 397 (2000).
- [Suortti et al. 2000] P. Suortti, T. Buslaps, V. Honkimäki, A. Shukla, J. Kwiatkowska, F. Maniawski, S. Kaprzyk and A. Bansil, J. Phys. Chem. Solids, to be published
- [Takada and Yasuhara 1991] Y. Takada and H. Yasuhara, Phys. Rev. B **44**, 7879 (1991).
- [Van Hove 1954] L. Van Hove, Phys. Rev. **95**, 249 (1954).
- [Weyrich 1978] W. Weyrich, *Einige Beiträge zur Compton-Spektroskopie*, Habilitationsschrift (Technische Hochschule Darmstadt, Darmstadt, 1978).
- [Weyrich et al. 1979] W. Weyrich, P. Pattison, and B. Williams, Chem. Phys. **41**, 271 (1979).
- [Weyrich 1996] W. Weyrich, *Quantum-Mechanical Ab-initio Calculation of the Properties of Crystalline Materials*, edited by C. Pisani, 245 (Springer-Verlag, Berlin-Heidelberg, 1996).

-
- [Wang et al. 1993] J. H. Wang, R. P. Sagar, H. Schmider, and V. H. Smith, *At. and Nucl. Data Tables* **53**, 233 (1993).
- [Wong et al. 1982] T. C. Wong, L. B. Mendelson, H. Grossman, and H. F. Wellenstein, *Phys. Rev. A* **26**, 181 (1982).
- [Zollner et al. 1991] S. Zollner, M. Garriga, J. Humlicek, S. Gopalan, and M. Cardona, *Phys. Rev. B* **43**, 4349 (1991).

List of Figures

1.1	The inelastic scattering process.	6
1.2	Electron momentum densities of the homogeneous interacting and the non-interacting electron gas and the corresponding Compton profiles.	17
2.1	Feynman diagrams for the calculation of the proper polarization function.	25
2.2	Real part and the absolute value of the imaginary part of the self-energy $\Sigma(\vec{p}, E)$ for different momenta \vec{p} and the corresponding spectral density function.	27
2.3	Feynman diagrams of the first and the second order vertex correction to the fully self-energy corrected proper polarization function. . . .	33
3.1	Experimental setup of the inelastic x-ray scattering beamline G3 of HASYLAB/DESY.	37
3.2	Crystallographic orientation of the lithium single crystal.	38
3.3	Raw spectrum of lithium for $\vec{q} \parallel [100]$	39
3.4	Energy dependent correction factors (G3 spectrometer).	43
3.5	Total lithium profile after energy dependent corrections for $\vec{q} \parallel [100]$	44
3.6	Momentum space resolution (G3 spectrometer).	46
3.7	Experimental lithium Compton profile for $\vec{q} \parallel [100]$ and $[110]$ compared to LDA theory.	48
3.8	Experimental lithium Compton profile for $\vec{q} \parallel [111]$ and $[311]$ compared to LDA theory.	49
3.9	Second derivatives of the experimentally observed lithium Compton profile for $\vec{q} \parallel [111], [110], [111]$ and $[311]$ compared to LDA theory.	51
3.10	Total Compton profile asymmetry of lithium for $\vec{q} \parallel [100], [110], [111]$ and $[311]$ and the directional average of the asymmetry.	53
3.11	Valence Compton profile asymmetry of lithium.	54

3.12	Lithium valence Compton profile asymmetry obtained from the experiment compared to the calculated asymmetry taking into account the full self-energy correction.	55
3.13	Lithium valence Compton profile asymmetry obtained from the experiment compared to the calculated asymmetry taking into account the full self-energy correction and in addition the first order and the first together with the second order vertex correction.	56
3.14	Spectral density function of the excited particle for different $ \vec{q} $. . .	59
3.15	Experimental Compton profiles compared to the LDA calculations with and without convolution with the spectral density function of the excited particle.	61
3.16	Symmetrized second derivatives of the experimentally obtained valence Compton profiles compared to LDA results with and without convolution with the spectral density function of the excited particle.	62
3.17	Values of the reciprocal form factor $B(\vec{R})$ calculated at the lattice translation vectors \vec{R} for $\vec{q} $ [100], [110], [111] and [311] compared to LDA theory with and without convolution with the spectral density function of the excited particle.	66
4.1	Lithium valence Compton profile measured for $\vec{q} $ [110] compared to the result of the LDA calculation.	70
4.2	Temperature dependence of the total Compton profile of lithium for $\vec{q} $ [110] calculated utilizing a LMTO supercell approach.	71
4.3	Experimental setup of the scanning-type x-ray spectrometer at the Compton scattering beamline ID15B of ESRF.	72
4.4	Reduction of the effective scattering volume utilizing a wolframcarbide rod.	73
4.5	Energy dependent correction factors (ID15B scannig-type x-ray spectrometer).	75
4.6	Total lithium profile after energy dependent corrections for $\vec{q} $ [110] measured at 295 K.	76
4.7	Momentum space resolution (ID15B scannig-type x-ray spectrometer).	77
4.8	Lithium Compton profile measured at ID15B / ESRF compared with the W2 / HASYLAB result.	78
4.9	Total Compton profiles measured at $T = 295$ K and $T = 95$ K.	79
4.10	Differences of the Compton profile asymmetries $J_{\text{asym}}(T = 95\text{K}) - J_{\text{asym}}(T = 295\text{K})$	81

4.11	Compton profile differences $J(p_z, T = 95\text{K}) - J(p_z, T = 295\text{K})$ compared to the temperature difference obtained from the thermal disorder model of Dugdale and Jarlborg.	82
4.12	Compton profile differences $J(p_z, T = 95\text{K}) - J(p_z, T = 295\text{K})$ compared to the result of the temperature dependent jellium calculation.	86
4.13	Temperature effect on the valence Compton profile of aluminium $J(p_z, T = 15\text{K}) - J(p_z, T = 560\text{K})$ compared to a temperature dependent jellium calculation.	87
4.14	Experimentally obtained valence Compton profile differences $J(p_z, T = 95\text{K}) - J(p_z, T = 295\text{K})$ compared to the pseudopotential calculations.	91
4.15	Temperature dependence of the contribution of the higher momentum components (HMC's) to the valence Compton profile.	92
A.1	Feynman diagrams of the self-energy series expanded in terms of the screened Coulomb interaction.	99

List of Tables

3.1	Position of the valence Compton profile maximum $p_z^{\text{CP}_{\text{max}}}$ and the difference of the Fermi break positions $p_F^+ + p_F^-$ determined from the experiment.	50
3.2	Amplitude and FWHM of the second derivatives at the Fermi momentum.	63
3.3	Values of the reciprocal form factor $B(\vec{R})$ obtained from Compton profile measurements at different incident energies having different momentum space resolutions.	67
4.1	Temperature dependence of the model parameters used within the jellium calculation.	85
4.2	Temperature dependence of the model parameters used in the pseudopotential calculation.	90

Publications

Papers

C. Sternemann, T. Buslaps, A. Shukla, P. Suortti, G. Döring, and W. Schülke, *Temperature influence on the valence Compton profiles of aluminium and lithium*, Phys. Rev. B **63**, 094301 (2001).

C. Sternemann, K. Hämäläinen, A. Kaprolat, A. Soininen, G. Döring, C.-C. Kao, S. Manninen, and W. Schülke, *Final state interaction in Compton scattering from electron liquids*, Phys. Rev. B **62**, 7686 (2000) (Rapid Communication).

C. Sternemann, G. Döring, C. Wittkop, W. Schülke, A. Shukla, T. Buslaps, and P. Suortti, *Influence of lattice dynamics on electron momentum density of lithium*, J. Phys. Chem. Solids **61**, 37 (2000).

C. Sternemann, A. Kaprolat, M. H. Krisch, and W. Schülke, *Evolution of the germanium $K \beta'''$ x-ray satellites from threshold to saturation*, Phys. Rev. A **61**, 020501 (2000) (Rapid Communication).

A. Kaprolat, K. Höppner, C. Sternemann, and W. Schülke, *New lights on electron correlation in simple metals: Inelastic x-ray scattering results vs. current theoretical treatment* in *Understanding chemical reactivity, Vol. 21: Electron, Spin and Momentum Densities and Chemical Reactivity*, edited by P. G. Mezey et al. (Kluwer Academic Publishers, Dordrecht, 2000).

C. Sternemann, A. Kaprolat, and W. Schülke, *Effect of thermal vibration and the solid-liquid phase transition on electron dynamics: An inelastic x-ray scattering study on Al*, Phys. Rev. B **57**, 622 (1998).

Conference contributions

C. Sternemann, K. Hämäläinen, A. Kaprolat, A. Soininen, G. Döring, C.-C. Kao, S. Manninen, and W. Schülke, *Final state interaction in Compton scattering from electron liquids*, Sagamore XIII: Conference on Charge, Spin and Momentum Densities, Stare Jablonki, Poland (2000) (oral representation).

G. Döring, H. Enkisch, C. Sternemann, and W. Schülke, *Resonant Raman scattering from CuO*, Sagamore XIII: Conference on Charge, Spin and Momentum Densities, Stare Jablonki, Poland (2000).

C. Sternemann, G. Döring, C. Wittkop, W. Schülke, A. Shukla, T. Buslaps, and P. Suortti, *Influence of lattice dynamics on electron momentum density of lithium*, International Workshop on Inelastic X-ray Scattering, Montauk, NY, USA (1998).

C. Sternemann, A. Kaprolat, G. Döring, and W. Schülke, *Self-energy effects in non resonant inelastic scattering from simple metals*, 17th General Conference of the Condensed Matter Division of the European Physical Society, Abstracts, 299, Grenoble, France (1998).

G. Döring, K. Höppner, C. Sternemann, A. Kaprolat, and W. Schülke, *Compton profile measurements on disordered Cu-Al alloys*, 17th General Conference of the Condensed Matter Division of the European Physical Society, Abstracts, 299, Grenoble, France (1998).

C. Sternemann, A. Kaprolat, and W. Schülke, *Effect of thermal vibration and the solid-liquid phase transition on electron dynamics: An IXSS-study on Al metal*, Sagamore XII, Waskiesu, Saskatchewan, Canada (1997).

A. Kaprolat, K. Höppner, C. Sternemann, and W. Schülke, *New lights on electron correlation in simple metals: Inelastic x-ray scattering results vs. current theoretical treatment*, Sagamore XII, Abstracts, 32, Waskiesu, Saskatchewan, Canada (1997).

C. Sternemann, R. Heise, K. Höppner, K.-J. Gabriel, A. Spiertz, A. Kaprolat, and W. Schülke, *The dynamic structure factor of liquid aluminium*, 17th International Conference on X-ray and Inner-shell Processes, Abstracts, 335, Hamburg, Germany (1996).

K. Höppner, W. Schülke, A. Kaprolat, C. Sternemann, S. Kaprzyk, F. Maniawski, and J. Kwiatkowska, *Measurements of the momentum space densities of $Cu_{1-x}Al_x$ by means of high resolution Compton scattering*, 17th International Conference on X-ray and Inner-shell Processes, Abstracts, 343, Hamburg, Germany (1996).

C. Sternemann, *The dynamic structure factor of aluminium*, International School on Condensed Matter Physics, Bialowieża, Poland (1996) (oral representation).

HASYLAB annual reports

G. Döring, H. Enkisch, C. Sternemann, and W. Schülke, *Resonant x-ray Raman scattering from CuO* (2000).

U. Magdars, H. Enkisch, G. Döring, C. Sternemann, and W. Schülke, *Measurement of the $Eu-L_{\beta_{2,15}}$ -fluorescence in EuO with RIXS* (2000).

C. Sternemann, R. Heise, G. Döring, H. Enkisch, A. Kaprolat, C. Wittkop, and W. Schülke, *Ultra high resolution Compton profile measurement of the valence profile asymmetry of lithium* (1998).

C. Wittkop, G. Döring, H. Enkisch, C. Sternemann, and W. Schülke, *Spin selective measurement of the unoccupied 5d DOS of EuO via resonant inelastic x-ray scattering (RIXS)* (1998).

C. Sternemann, G. Döring, R. Heise, A. Kaprolat, and W. Schülke, *Ultra high resolution Compton profile measurements of lithium single crystal* (1997).

C. Wittkop, F. Wohlert, R. Heise, C. Sternemann, H. Enkisch, and W. Schülke, *Resonant inelastic x-ray scattering (RIXS) on Eu_2O_3* (1997).

C. Sternemann, R. Heise, K. Höppner, K.-J. Gabriel, C. Wittkop, A. Kaprolat, and W. Schülke, *Effect of reduced long-range order on Al metal* (1996).

C. Wittkop, F. Wohlert, R. Heise, C. Sternemann, and W. Schülke, *Circular dichroism of the $\text{Eu-L}_{\beta_{2,15}}$ emission from ferromagnetic EuO investigated by resonant IXSS* (1996).

C. Sternemann, R. Heise, K. Höppner, K.-J. Gabriel, A. Spiertz, A. Kaprolat, and W. Schülke, *The dynamic structure factor of liquid aluminium* (1996).

Danksagung

Ich bedanke mich bei Herrn Prof. Dr. *Winfried Schülke* für die Vergabe des Themas, sein stets förderndes Interesse an dieser Arbeit und die Bereitschaft zu zahlreichen Diskussionen während meiner gesamten Promotionszeit, die mir einen tieferen Einblick in die Welt der Quasiteilchen gegeben haben.

Allen MitarbeiterInnen der Arbeitsgruppe E Ib am Lehrstuhl für experimentelle Physik I der Universität Dortmund möchte ich für ihre ständige Hilfs- und Diskussionsbereitschaft danken. Besonderen Dank schulde ich *Gordon Döring*, *Hartmut Enkisch*, Dr. *Rainer Heise*, Dr. *Axel Kaprolat* und Dr. *Christof Wittkop* für ihre Unterstützung bei den vielen Messschichten am HASYLAB und an der ESRF. Ohne ihre Hilfe wäre die Durchführung der zahlreichen Experimente nicht möglich gewesen. Weiterhin danke ich *Cord Wöhning* und *Joachim Schulz* für ihre Mitarbeit während meiner Aufenthalte am HASYLAB.

Gordon Döring und Dr. *Axel Kaprolat* haben ihre Zeit geopfert, um diese Arbeit zu lesen und ausführlich mit mir zu diskutieren.

Allen MitarbeiterInnen der Dortmunder Elektronen Testspeicherringanlage (DELTA), der mechanischen Werkstatt und des Konstruktionsbüros des Instituts für Physik der Universität Dortmund danke ich für ihre Unterstützung während meiner Arbeit an der SAW 2 Strahllinie. Weiterhin bedanke ich mich bei Herrn *Friedrich Ströwer* und Frau *Gisela Pike* für die gute Zusammenarbeit. Dr. *Klaus-Jürgen Gabriel* und *Rainer Wollmann* standen mir stets beratend zur Seite.

Für willkommene Abwechslung während der HASYLAB Messzeiten haben *Christian*, *Uli*, *Radu*, *Martin* und *Rainer* gesorgt. Ich erinnere mich gerne an die gemütlichen Grillabende vor der HARWI Halle, das Sonnenbaden an der Strandperle und die nächtlichen Exkursionen mit *Achim*, *Cord*, *Rainer*, *Klaus*, *Uta* und *Christof*.

Ohne die liebevolle Unterstützung und Geduld meiner Frau *Gabi* wäre die Durchführung dieser Arbeit nicht möglich gewesen. Meinen Eltern und Schwiegereltern danke ich für ihre ständige Hilfsbereitschaft insbesondere seit der Geburt unseres Sohnes *Lasse*.

Acknowledgment

I want to thank *Keijo Hämäläinen* for the fruitful cooperation concerning the high resolution Compton profile measurements of lithium performed at the HASYLAB and the NSLS and the valuable discussions of the data treatment. It was a long way until we were convinced that the asymmetry and the smearing of the lithium valence Compton profile was real. However, it was a good experience to work hard for a few days in Helsinki with having a lot of fun and a lot of satisfying results. I would like to thank all the people which were an integral part of the lithium high resolution project, namely *Winfried Schülke*, *Alexi Soininen*, *Axel Kaprolat*, *Chi-Chang Kao*, *Gordon Döring*, *Seppo Manninen* and *Keijo Hämäläinen*. Especially, the discussions of the many-particle calculations with *Winfried Schülke* and *Axel Kaprolat* have been essential. I had, and will have, a lot of interesting discussions related to the temperature effects on Compton scattering with *Simo Huotari*, who also gave me a nice introduction into the matlab codes.

At the ESRF it was a great pleasure to work at the beamline ID15. *Thomas Buslaps* and *Abhay Shukla* aligned the Compton scattering experiments well and gave an excellent support combined with many helpful discussions. *Veijo Honkimäki* was permanently disposed to answer my questions and *Pekka Suortti* gave a lot of important suggestions to improve my work.

I have to thank *Arun Bansil* and *Stanislaw Kaprzyk* for providing their LDA calculations of the lithium Compton profiles in numerical form.

Michael Krisch and *Axel Kaprolat* enabled my measurements of the germanium x-ray satellites during the commissioning of ID28 at the ESRF. At this time I learned how to work efficiently with having much fun. I had the pleasure to spend a few nice evenings with *family Krisch* and *Axel*.

There was more than science in Grenoble, Helsinki and elsewhere. I enjoyed the social life in Grenoble with *Christian*, *Cécile*, *Veijo* (How is skiing?), *Mauriz*, *Bettina* and *Thomas*. The canoe trip in Canada with *Joanne*, *Abhay*, *Thomas*, *Pekka*, *Gordon*, *Axel*, and *Veijo* is unforgotten and *Simo* showed me, that there exists a really good punk rock reggae band in Helsinki. It was a pleasant surprise that a part of the Compton community likes to play soccer, volleyball and pool.

This work was supported by the German Ministry of Education and Research under contract no. 05 ST 8 HRA.